SANDIA REPORT

SAND2004-5211
Unlimited Release
Printed January 2005

Geomechanics of Penetration: Experimental and Computational Approaches: Final Report for LDRD Project 38718

David J. Holcomb, Arlo F. Fossum, Glen L. Gettemy, Robert D. Hardy,
Dave R. Bronowski,
Geomechanics Raul R. Rivas, and Dale S. Preece

Prepared by Sandia National Laboratories
Albuquerque, New Mexico 87185 and Livermore, California 94550

Sandia is a multiprogram laboratory operated by Sandia Corporation,
a Lockheed Martin Company, for the United States Department of Energy's
National Nuclear Security Administration under Contract DE-AC04-94AL85000.

Sandia National Laboratories

Issued by Sandia National Laboratories, operated for the United States Department of Energy by Sandia Corporation.

Available to DOE and DOE contractors from
U.S. Department of Energy
Office of Scientific and Technical Information
P.O. Box 62
Oak Ridge, TN 37831

Telephone: (865)576-8401
Facsimile: (865)576-5728
E-Mail: reports@adonis.osti.gov
Online ordering: http://www.osti.gov/bridge

Available to the public from
U.S. Department of Commerce
National Technical Information Service
5285 Port Royal Rd
Springfield, VA 22161

Telephone: (800)553-6847
Facsimile: (703)605-6900
E-Mail: orders@ntis.fedworld.gov
Online order: http://www.ntis.gov/help/ordermethods.asp?loc=7-4-0#online

SAND2004-5211
Unlimited Release
Printed October 2004

Geomechanics of Penetration: Experimental and Computational Approaches: *Final Report for LDRD Project 38718*

David J. Holcomb, Arlo F. Fossum, Glen L. Gettemy, Robert D. Hardy, Dave R. Bronowski
Geomechanics
Raul R. Rivas, Dale S. Preece
Explosives Applicatons
Sandia National Laboratories
PO Box 5800
Albuquerque, NM 87185-0751

Abstract

The purpose of the present work is to increase our understanding of which properties of geomaterials most influence the penetration process with a goal of improving our predictive ability. Two primary approaches were followed: development of a realistic, constitutive model for geomaterials and designing an experimental approach to study penetration from the target's point of view. A realistic constitutive model, with parameters based on measurable properties, can be used for sensitivity analysis to determine the properties that are most important in influencing the penetration process.

An immense literature exists that is devoted to the problem of predicting penetration into geomaterials or similar man-made materials such as concrete. Various formulations have been developed that use an analytic or more commonly, numerical, solution for the spherical or cylindrical cavity expansion as a sort of Green's function to establish the forces acting on a penetrator. This approach has had considerable success in modeling the behavior of penetrators, both as to path and depth of penetration. However the approach is not well adapted to the problem of understanding what is happening to the material being penetrated. Without a picture of the stress and strain state imposed on the highly deformed target material, it is not easy to determine what properties of the target are important in influencing the penetration process.

We developed an experimental arrangement that allows greater control of the deformation than is possible in actual penetrator tests, yet approximates the deformation processes imposed by a penetrator. Using explosive line charges placed in a central borehole, we loaded cylindrical specimens in a manner equivalent to an increment of penetration, allowing the measurement of the associated strains and accelerations and the retrieval of specimens from the more-or-less intact cylinder.

Results show clearly that the deformation zone is highly concentrated near the borehole, with almost no damage occurring beyond ½ a borehole diameter. This implies penetration is not strongly influenced by anything but the material within a diameter or so of the penetration. For penetrator tests, target size should not matter strongly once target diameters exceed some small multiple of the penetrator diameter. Penetration into jointed rock should not be much affected unless a discontinuity is within a similar range.

Accelerations measured at several points along a radius from the borehole are consistent with highly-concentrated damage and energy absorption; At the borehole wall, accelerations were an order of magnitude higher than at ½ a diameter, but at the outer surface, 8 diameters away, accelerations were as expected for propagation through an elastic medium. Accelerations measured at the outer surface of the cylinders increased significantly with cure time for the concrete. As strength increased, less damage was observed near the explosively-driven borehole wall consistent with the lower energy absorption expected and observed for stronger concrete. As it is the energy absorbing properties of a target that ultimately stop a penetrator, we believe this may point the way to a more readily determined equivalent of the S number.

Contents

Tables and Figures

This page intentionally left blank

Historical Approach to modeling penetration

An immense literature exists, devoted to the problem of predicting penetration into geomaterials or similar man-made materials such as concrete. Virtually all of this work can be related to early work by Hill (1948) who analyzed the problem of an expanding spherical void as a means of understanding the effect of bombs on structures partially or wholly buried in the earth. From this early work, various formulations have been developed that use an analytic or more commonly, numerical, solution for the spherical or cylindrical cavity expansion as a sort of Green's function to establish the forces acting on a penetrator. Work by Forrestal and Tzou (1997) is a good example of this approach, which has had considerable success in modeling the behavior of penetrators, both as to path and depth of penetration. However the approach is not easily adapted to the problem of understanding what is happening to the material being penetrated. Without a picture of the stress and strain state imposed on the highly deformed target material, it is not easy to determine what properties of the target are important in influencing the penetration process.

Compared to the body of literature discussing the penetrator and the forces on it, derived from some variant of cavity expansion, there is a paucity of work aimed at understanding the target and its response to the penetration process. The experiments required are difficult and not well defined. Two recent examples are the work by Gran and Frew (1997) and Kerr et al. (1998). Gran and Frew embedded stress gages in concrete cylinders as they were being cast. A penetrator was then fired into the concrete target and the resultant stresses measured. In experiments similar to the work reported here, Kerr et al. embedded a network of stress gages and accelerometers in concrete surrounding a spherical explosive charge. Commonly in this situation, a computational approach is used to give guidance and build intuition about the problem. However, the current state of computation does not allow us to realistically model the penetration problem in geomaterials. One source of difficulty is the singularity along the line of penetration where the material must accommodate very large strains in order to open the cavity. Another area of difficulty is the constitutive models for geomaterials. In general, the constitutive behavior of geomaterials is anisotropic, non-linear, pressure-sensitive, hysteretic, damaging and rate-sensitive. Geomaterials can compact or dilate, often doing both for some portion of a given load path. There are few, if any, constitutive models that can replicate this range of behavior and that, in addition, use parameters which can be derived from doable experiments.

The purpose of the present work is to increase our understanding of which properties of geomaterials most influence the penetration process with a goal of improving our predictive ability. Two primary approaches were followed: development of a realistic, constitutive model for geomaterials and designing an experimental approach to study penetration from the target's point of view. A realistic constitutive model, with parameters based on measurable properties, can be used for sensitivity analysis to determine the properties that are most important in influencing the penetration process. Of course such a model will be valuable in its own right for the better representation of the response of geomaterials.

Rock Penetration: Finite Element Sensitivity and Probabilistic Modeling Analyses

A. F. Fossum, Geomechanics

This work is the subject of a report of the same title (Fossum, 2004) and makes use of the constitutive model developed by Fossum and Brannon (2004). What follows is a summary of the report.

Executive Summary

The relative importance is determined of rock model parameters representing the presence of microscale flaws such as porosity and networks of microcracks and rock mass structural features on depth of penetration calculations for a weapon projectile. After the determination of key parameters, which represent the dominant deformation mechanisms controlling penetration resistance, a probabilistic analysis is undertaken with an advanced reliability method that incorporates the deterministic tools developed in this project to quantify the uncertainty of the predicted penetration depth response caused by the uncertainty in the input material parameters representing the controlling mechanisms. The key parameters containing uncertainty are then ranked according to their probabilistic importance factors. Thus, if it were desired to decrease the uncertainty in the predicted penetration response the analyst has the option of attempting to reduce the uncertainty of the most important parameters, perhaps by additional testing.

The constitutive model used in the analyses for rock behavior during penetration is developed to take into account the principal deformation mechanisms controlling penetration as well as up-scaling of these processes to account for rock-mass and structural features that could influence a penetration event. For computational tractability, and to allow relatively straightforward model parameterization using standard laboratory tests, the constitutive model is constructed to strike a balance between first-principals micro-mechanics and phenomenological modeling strategies. The over-arching goal of the constitutive modeling effort is to provide a unified general-purpose constitutive model that can be used for any geological or rock-like material and one that is predictive over a wide range of porosities and strain rates.

The following conclusions are drawn from more than 30 penetration finite element analyses:

1) The most important physics features represented in the rock model from the standpoint of predicting penetration in order of importance are *a*) pressure sensitivity of yield, *b*) the coefficient of friction between the penetrator and the rock, *c*) ubiquitous rock jointing, *d*) strain-rate sensitivity, and *e*) pore collapse. Playing lesser roles are tensile cracking, kinematic hardening, Lode angle dependence of yield, and nonlinear elasticity.
2) When the important physics features are included in the model, the material parameters representing the physics that are most important *deterministically* in order of importance are *a*) strain-rate sensitivity, *b*) ubiquitous rock jointing, *c*) the coefficient of friction between the penetrator and the rock, *d*) porosity, and *e*) pressure sensitivity of yield.

From a *probabilistic* standpoint the order of importance changes because of the degree of uncertainty associated with the parameters. The key probabilistic importance factors in order of importance are *a*) ubiquitous rock jointing, *b*) strain-rate sensitivity, *c*) the coefficient of friction between the penetrator and the rock, *d*) pressure sensitivity of yield, and *e*) pore collapse. Because all rocks have inherent uncertainty it is the probabilistic importance factors, which combine deterministic sensitivities with uncertainty, that are perhaps the most important from a practical standpoint.

4) Penetration depth increases with increasing striking velocity. If the striking velocity is too low, the penetrator will ricochet off the target.

5) The influence of pore collapse on penetration increases slightly with increasing striking velocity because of the difference in the load path followed with increasing striking velocity.

Scientific Impact

The scientific impact of the findings of this research effort on penetration prediction is that it is more important to include the major physics phenomena governing penetration in a rock model used to model penetration than it is to evaluate a full physics model that characterizes the complete stress-strain curves obtained in laboratory testing. Also, the uncertainties in the parameters associated with the main physics for Salem Limestone, which is a rock with relatively low uncertainty compared with many sedimentary rocks, translate to 27 % uncertainty in penetration depth predictions with 98% confidence. If a target rock can be identified through telemetry and/or other means it may be possible to use this information to identify a rock classification from which a known rock characterization for an analog rock can be used to make penetration depth predictions as a function of striking velocity with relatively high confidence from only a minimal amount of laboratory testing.

Recommendations

It is recommended that a suite of candidate target rock types be characterized with the minimum amount of testing to evaluate the key parameters representing the important physics governing penetration resistance for general categories of rock types likely to be identified through direct as well as indirect means.

Experiments

Experimental Approach

Our goal was an experimental system that allowed more control of the processes that occur during penetration into rock-like materials than is possible in an actual penetrator experiment. By simplifying the process it was believed that a deeper understanding of the effects of penetration on rock-like materials could be gained. The price paid for this reductionist approach is concern over the relevance of our experiments to increasing our understanding of the actual penetration process. Answering the question of relevance will require a step beyond the present work; the same techniques for characterizing the damaging effects observed in the present experiments will need be applied to the target materials damaged by penetrators. Field observations and calculations do provide some guidance in designing an appropriate system.

Anecdotal evidence from various sources indicates that the material displaced by the penetrator is highly deformed in a relatively thin zone, beyond which little damage is obvious. Tensile cracks along the radii from the axis of penetration are commonly observed. Computational results, to be discussed later, also indicate that the deformation of the target required to accommodate the volume of the penetrator occurs in a thin zone. Finally, the deceleration curves for penetration into concrete, obtained by Forrestal et al. (2003), show a nearly constant deceleration, with the exception of a small kinetic energy term at shallow penetrations and the obvious effect of the cratering at the free surface where the penetrator enters.

This is a very informative result. If the deceleration were constant it would indicate that the processes responsible for stopping the penetrator are independent of velocity. It is of course possible that compensating changes in rate dependence could cancel, resulting in an apparent rate independence. However it is much simpler to assume that the data are telling us that the penetration process is rate independent in the usual range of velocities which extends up to a few hundred meters per second. Assuming that the process is indeed rate-independent (or nearly so) leads to the conclusion that the penetration process should look the same along the penetrator's path as the penetrator is slowed to a stop. Similarity along a path implies that the effects should have a cylindrical geometry.

From these various lines of thought, we chose an experimental system consisting of concrete cylinders with a line charge of explosives along the axis of a hole cast on the cylinder's central axis. Concrete is convenient for a number of reasons: inter-specimen reproducibility, ease of emplacing gages, adjustable physical properties, and comparability with previous work, particularly that of Forrestal et al. (2003) and Warren et al. (2004). Details of the experiments will be discussed later. Overall, our goal was to simulate various stages of the penetration process by varying the velocity boundary conditions imposed on the concrete by using different amounts of explosive. Taking advantage of concrete's increasing strength with time, we were able to test cylinders that were the same in terms of composition and porosity but had a range of strengths. It is usually impossible to change just one parameter in a natural target material. As a result, distinguishing the effects of strength, material composition, porosity, pressure dependence, etc. is difficult.

Sample Design

Figure 1 is a diagram of the specimen geometry and the initial layout of the accelerometers. Sample dimensions were governed by several factors: similarity to targets used by Forrestal et al. (2003), a need to obtain a cylindrically symmetric stress state at mid-height of the sample and finally, the need to transport the cylinders after casting. A diameter of 900 mm (36 inches) is similar to that used by Forrestal et al. (2003) in penetration experiments on a similar, weak concrete. Specimen length was chosen to be 1200 mm (48 inches) to ensure that end effects would not be communicated to the gage locations during the initial pass of the stress wave. A longer cylinder might have been better, but the logistics of moving the specimens quickly becomes prohibitive.

A weak concrete mix, without aggregate, was chosen to replicate as closely as possible the concrete used by Forrestal et al. (2003) and Warren et al. (2004). Table 1 lists the materials used per cubic yard of concrete. A local batch plant was contracted to provide the mix. Because strain gages were to be applied to the exterior surface, an unusually smooth surface was desired. To achieve the desired finish, the specimens were cast in architectural-grade Sonotube forms which had a special, seamless, glassy interior finish. Overall, the surface finish was good, but entrained air bubbles formed cavities which had to be filled with a plaster compound before applying the exterior strain gages.

The concrete cylinders were cast on a ½” thick, 8 ft. x 8 ft. steel platform to allow the cylinders to be transported via forklift, both before and after testing. A 102-mm (4-inch) -diameter borehole was cast concentric with the cylinder’s axis to allow placement of the explosive charge and provide an air buffer for smoothing of the explosive pulse. Two radial holes were also cast in place to allow the placement of internal accelerometers at the wall of the borehole, 50 mm (2 inches) from the explosive charge. A mold, setup and ready for filling, is shown in Figure 2a. A Sonotube form was supported by a casting jig to ensure that the form stayed centered on the 4-inch-diameter pipe used to form the axial hole. The interior of the form is seen in Figure 2b showing the removeable pipe (black tube) that formed the axial, 102 mm (4-inch) -diameter borehole and the four fixtures that formed the mounting holes for the accelerometers at mid-height in the cylinder. During pouring, the form was half filled in one pour, before pausing to insert the strain gages. The pour was manually rodded to remove air bubbles, but mechanical vibration was not used for fear the very liquid concrete mix would lift the form, ruining the pour. Specifications were checked against the as-delivered mix and, in case of doubt, a very informal slump test was done. The liquidity of the mix was such that it would spread almost flat. One load was rejected on the basis of too much water and, as will be discussed later, moisture content was a continuing source of problems.

Strain gages

Strains and accelerations were measured at several distances from the central borehole using both embedded gages and surface mounted gages. Strain gages used were Micromeasurements 1 and 2 inch gages suitable for small strains. One of our major concerns was achieving good coupling between the rather smooth surfaces of the strain gage backing material and the concrete that the gages were cast into. At the expected high strain rates it was easy to imagine that the gage backing would simply slip instead of straining the gage grid. In addition there was the problem of holding the flimsy strain gages in the correct orientation, without bending, and at the desired positions as nearly 1700 kg of concrete was poured into the form.

The solution to the coupling problem was to change the smooth gage surface to a very rough surface by gluing sand to the gages. Figure 3a shows the results which were not pretty, but proved very effective. In addition to providing good coupling, the glued-on sand stiffened the gages sufficiently so that bending was not a problem as long as they were handled gently.

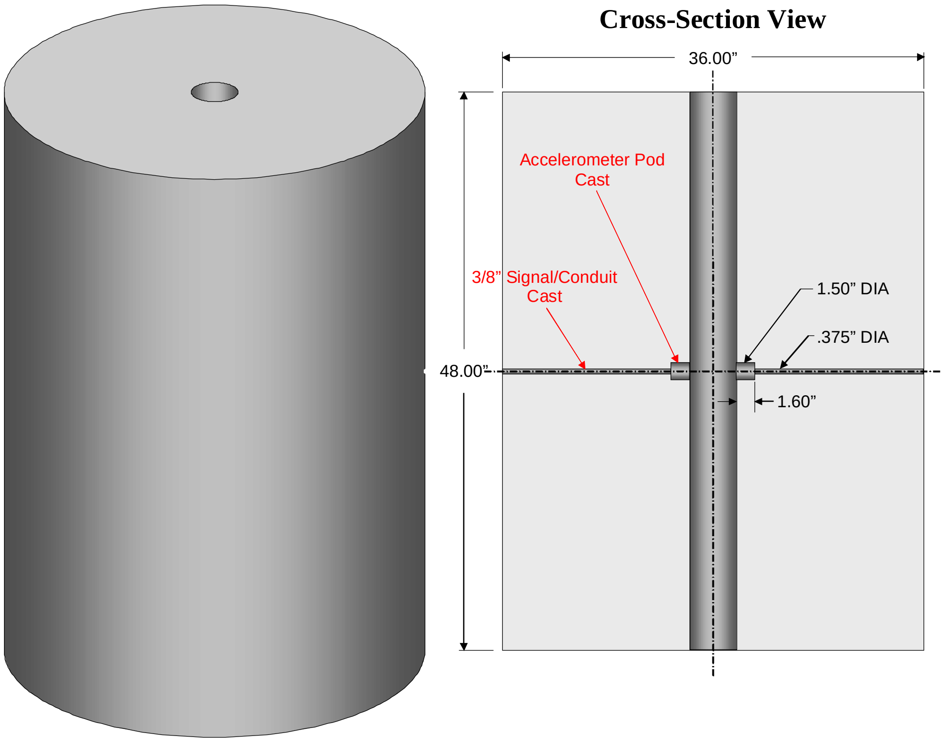

Figure 1. Diagram of the initial concrete cylinder design showing the cast-in hole for explosives (left) and a cross-section indicating the position of the accelerometers. Strain gages (not shown) were cast in at the same level as the accelerometers.

We wished to measure the three strain components in the radial, circumferential and vertical directions, at two distances from the cylinder axis. A wire frame was constructed consisting of two right triangles connected at the 45 degree angles by 125-mm (5 inch) wire legs and at the 90 degree angles by a backbone wire. The backbone wire extended 140 mm (5.5 inches) beyond the triangular frames in both directions. A photograph of the frame (Figure 3b) shows the mounted gages which were tacked to the frame with epoxy. This simple jig proved surprisingly easy and robust to use under field conditions. When the concrete pour reached the ½ full level, pouring was halted and the jig with mounted gages was worked into the concrete. By placing the end of the 140 mm wire against the pipe used to form the axial hole, it was possible to place the gages within a few mm of the desired positions and at the desired orientation. Embedding the jig was made much easier if the concrete was agitated with a probe (a 2x6 worked well) in the vicinity of the jig. The agitation causes the viscosity of the concrete to drop sharply and the jig slid in easily. Figure 4 shows the gages being emplaced and illustrates the function of the wires extending on either end of the jig in controlling gage position. Electrical wiring for the gages was run out through the side of the form through a drilled hole. No attempt was made to seal the hole which fit relatively tightly around the wire bundle. Figure 5 is a drawing showing the relative position of the gages in the cylinder. Two strain gages were glued to the exterior surface to measure strains in the vertical and circumferential directions.

An unanticipated difficulty was the coupling of the electromagnetic pulse from the explosion into the Wheatstone bridge circuitry used with the strain gages. Initial results were disappointing; in fact, no data were obtained on strains due to the large induced voltages which swamped the presumed signal. Determining a solution to the problem was difficult since only the actual explosion served to recreate the electrical pulse. Nearby test shots did not reproduce the phenomenon. As a result, testing of several cylinders yielded no strain data. Decoupling the bridges from the electrical system and each other by using a battery power supply for each bridge removed most of the interference from the exterior gages, but not those embedded in the concrete. It was finally realized that the wire mounting jig, in intimate contact with all of the embedded gages, was acting as an antenna to couple electrical energy into the embedded gages. Grounding the jig via its almost-exposed end wire solved the problem. A non-metallic jig would avoid the coupling problem altogether.

Table 1. Materials used for weak concrete, UCS=22 MPa (3400 psi). Quantities are for one cubic yard and weights are in pounds

ASTM Type I/II portland cement	516 lb
Natural, siliceous, concrete sand, SSD condition	2708 lb
Water reducer, high-range, Eucon 37	912 ml or 31 fl oz
Water reducer, normal-range, Eucon WR-9	912 ml or 31 fl oz
Water	438 lb
Aggregate	0

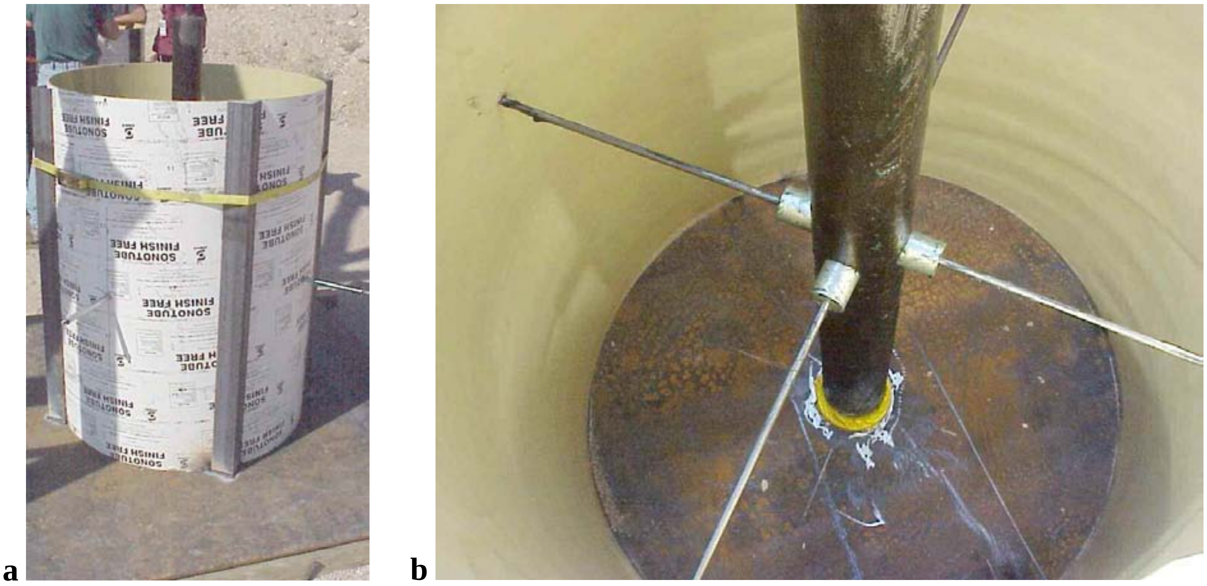

Figure 2. (a) Sonotube form mounted on casting jig (b) Interior of form showing the molds that formed the axial, 4-inch-diameter hole (black tube) and the four fixtures that formed the mounting holes for the accelerometers.

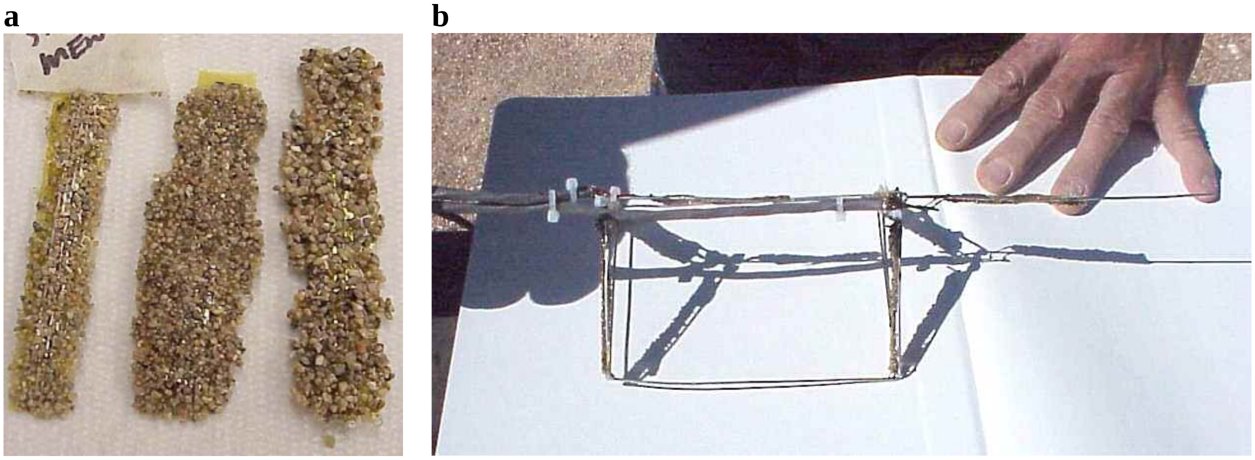

Figure 3. (a) Sand-encapsulated strain gages ready for mounting on the emplacement jig (b) emplacement jig used to hold strain gages at proper radial distances and orientation while pouring the specimen.

a **b**

Figure 4. (a) Emplacing a set of strain gages at the mid-height of the pour (b) Gages in place showing the function of the emplacement jig for holding the correct distances and orientations.

Accelerometers

One of the primary goals was to measure accelerations as a means of determining how the radiated energy varied as a function of distance from the explosive and strength of the concrete. Several arrangements of accelerometers were tested as we encountered and overcame various problems. Normally four piezo-resistive accelerometer transducers were installed on each cylinder, with two embedded and two externally mounted. For the first two tests, a total of 8 accelerometers were employed to increase the likelihood of covering the proper, unknown, acceleration range. A full list of the types and numbers of accelerometers used on each test may be found in Table 2.

Accelerometers were encapsulated in aluminum pods for protection (see Figure 6) and positioned at the midheight of the concrete cylinder. Two accelerometers were placed with faces flush with the wall of the internal 4-inch hole (see Figure 7) and two accelerometers were placed on the external wall of the concrete cylinder as shown in Figure 5 and Figure 8. The external accelerometer pods (Figure 6b) were mounted on the surface of the concrete cylinder using a plaster-like material. To avoid or minimize the effects of the radial hole used to embed the internal accelerometers, mounting positions were displaced 6 inches circumferentially away from the signal access conduit of the internal accelerometers (Figure 5 and Figure 8).

Initially, two accelerometers with a range of 200-kilo-g's (1,960,000 m/s^2) were installed flush with the borehole wall. Based on modeling it appeared that accelerations there should be around 300,000 m/s^2, which is well within the range of accelerations that could be encountered without damage. As will be discussed later, it appears that the actual accelerations were consistent with the modeling, but other effects resulted in damage or destruction of the accelerometers. Exposed to the full force of the explosion with only the grouting material to hold the mounting pod in place, it was perhaps to be expected that the pod would break loose, leading to very high accelerations. In addition, there was concern that fragments from the detonator would strike the face of the mounting pod, again causing high, damaging, apparent accelerations.

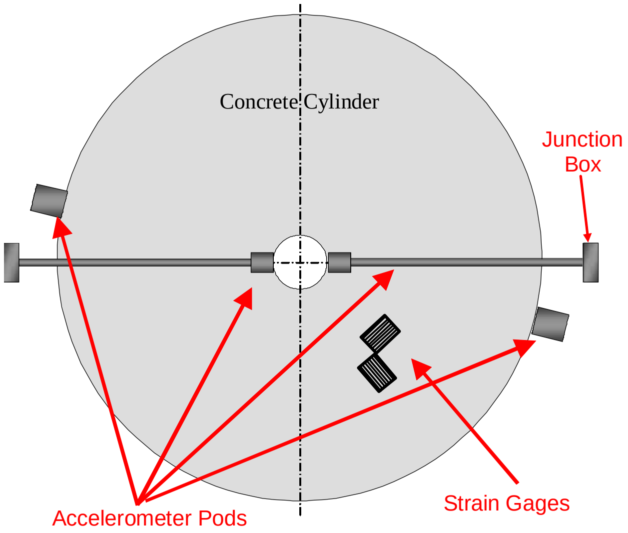

Figure 5. Top-View of instrumentation setup used for initial tests.The embedded accelerometer pods were mounted with faces flush with the wall of the 102 mm (4-inch) borehole using the pre-formed holes and bonded to the concrete using a plaster-like material.

After several attempts ended with destroyed accelerometers, the placement of the inner accelerometers was changed; one 200kg accelerometer was placed 4 inches inside the concrete or 151 mm (6 inches) from the explosive and another was placed 202 mm from the explosive. This arrangement proved satisfactory in terms of recording accelerations in the interior of the specimen but did not capture the accelerations in the near field where most non-linear, energy-absorbing processes were expected to occur. Later discussions will expand on this point.

All data for strain gages and accelerometers were recorded using 4-channel LeCroy WavePro oscilloscopes at 8 bit resolution. The low dynamic range complicated the problem of proper amplification of signals to optimize the limited recording range. Each accelerometer was recorded on two or more channels to allow different amplification and time intervals. Strain gages were only recorded on one channel.

Table 2. Types and range of accelerometers used for each shot.

Test #	**Cylinder #**	Accelerometers	Range (g) (number used)
1	Cylinder 1	Endevco Model 7270A and Model 2262A	200K, 60K, 20K, 6K, 2K, 1K, 100, and 25
2	Cylinder 2	Endevco Model 7270A and Model 2262A	200K, 60K, 20K, 6K, 2K, 1K, 100, and 25
3	Cylinder 7	Endevco Model 7270A	200K (2), 2K (2)
4	Cylinder 8	Endevco Model 7270A	200K (2), 2K (1), 100 (1)
5	Cylinder 9	Endevco Model 7270A	200K (2), 2K (1), 100 (1)
6	Cylinder 10	Endevco Model 7270A	200K (2), 20K (1), 2K (1)
7	Cylinder 6	Endevco Model 7270A	200K (2), 20K (1), 2K (1)
8	Cylinder 5	Endevco Model 7270A	200K (2), 20K (1), 2K (1)
9	Cylinder 3	Endevco Model 7270A	200K (2), 20K (1), 2K (1)
10	Cylinder 4	Endevco Model 7270A	200K (2), 20K (1), 2K (1)

Explosives design

Several design criteria were imposed on the explosive system used to drive the experiments: cylindrical symmetry, particle velocities in the range imposed by penetrators, significant damage, and recoverable target materials. Cylindrical symmetry was achieved by use of a cylinder of explosive centered in the borehole and detonated at the mid-height of the cylinder. This initiated a pressure wave whose wave front was nearly parallel to the borehole wall in the mid-height portion of the cylinder.

Particle velocities imposed by free-fall penetrators are in the range of few hundred m/s, with a geometric factor depending on the shape of the penetrator nose. Near the tip of a rounded nose, velocities are extremely high, while approaching zero for a nose that fairs smoothly into the main, cylindrical body of the penetrator. There is a conflict between achieving realistic particle velocities and leaving the target sufficiently coherent to examine the induced damage. Because the penetrator imposes a displacement boundary condition, the loading is much stiffer, resulting in less overall damage. Once the target material is pushed back out of the way, the stress applied drops rapidly. With the gas-driven pressure boundary condition imposed by explosives, the loading is much more compliant. As a result, pressures sufficient to accelerate the target material to the velocities imposed by penetrators tend to pulverize the target. An idea considered for future work is to combine the explosives with an expandable liner installed against the inner wall of the borehole. This would allow the pressure from the explosively-generated gases to deform the target through expanding the liner, but would then change to a stiff boundary condition, preventing unwanted damage. A liner should also protect the cylinder ends from cratering.

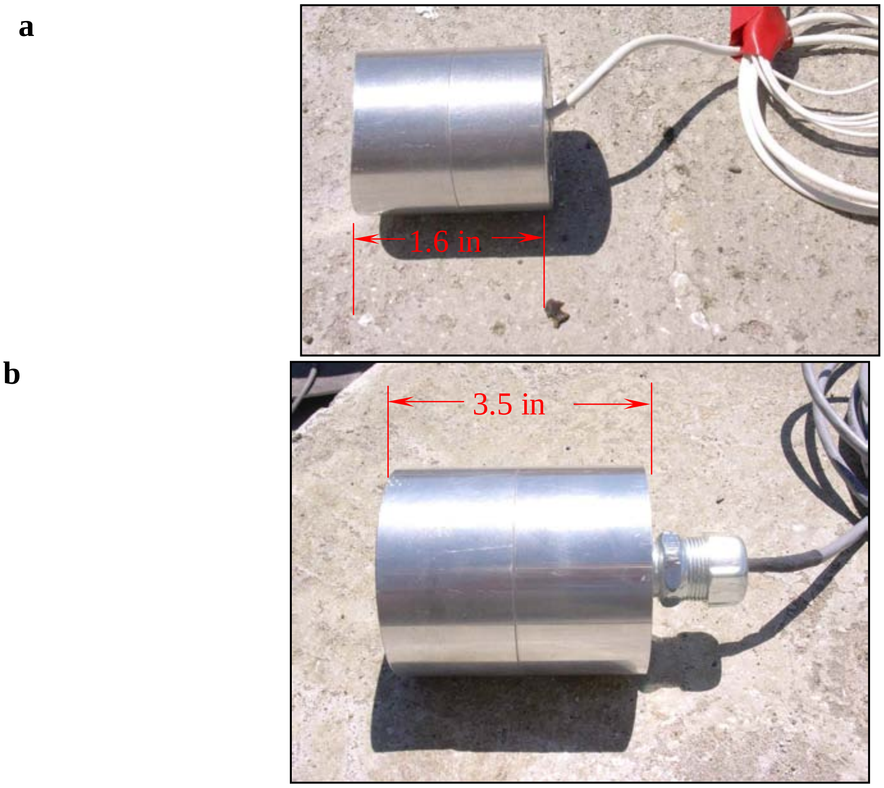

Figure 6. Mounts for accelerometers. (a) used at the borehole wall. Note curved face to match borehole curvature. (b) used on exterior of cylinder.

Figure 7. A view down the borehole in which the protective mounting pod for an embedded accelerometer may be seen at the top, flush with the wall of the borehole.

Figure 8. External accelerometer mounted on specimen to the left of the exit point for one of the embedded accelerometers.

Scoping calculations indicated that to achieve particle velocities near the borehole approaching 100 m/s would require about 800 g of C-4, which is a substantial amount of explosives. The results of the test on Cylinder #1 were spectacular, but not very useful. The target was nearly destroyed, making it difficult to retrieve materials. As later results showed, the destruction was enhanced by the pressure pulse reflecting off the steel plate sealing the lower end of the borehole, implying that it may be feasible to use larger amounts of explosives than were ultimately used in the present work. However for the present work, a substantially smaller amount of PETN was used in all of the non-developmental tests. Table 3 lists all the tests and corresponding explosives load.

Because one of the main points of the work was to be able to recover and characterize target materials post-test, we compromised on the side of target survival, accepting lower imposed velocities. Target disruption was successfully minimized by surrounding the cylinder with 30 cm of wet sand in an annulus between the cylinder and a 1.5 m (5 ft) diameter steel culvert.

Another measure of the comparability between the present work and real penetrator tests is the amount of energy deposited in the target. PETN releases about 5860 J/gm when detonated. Thus the 156 gm charge used in tests 3-9 released about 925,000 J. By comparison, a 1 kg penetrator moving 1 m/s carries ½ J of kinetic energy, which of course increases as the square of the velocity. At 100 m/s, the same penetrator carries 5000 J and at 500 m/s, the kinetic energy is 125,000 J. Thus the explosive deposits energy in the target that is of the same order of magnitude as a 10 kg test penetrator..

Experimental Program

Ten concrete cylinders measuring 900 mm (36 inches) in diameter by 1200 mm (48 inches) in length were constructed using the concrete mix described in Table 1. The program was built around the idea that the influence of strength on penetrability and target behavior could be studied by using the same concrete, but testing at different cure ages to allow the concrete to gain strength. Ideally, if the concrete were the same, then the only variation would be strength. For natural targets, such as rock, it is almost impossible to vary material parameters in any systematic way. Four casting-to-test intervals were planned: 3-day, 7 days, 14 days, and 28 days. Cylinders were formed as described earlier. Casting dates were chosen in accord with the test schedule in Table 3 to achieve efficient use of the test facility, limit testing to one specimen per day and produce two cylinders for each cure stage. The first two cylinders were considered to be developmental, with the last eight designed to meet the test goals. Table 3 tabulates the cylinder designation, explosive quantities, and test dates for the entire test series.

All shots were performed at the “Boom-Box” in Building 9930. When the concrete cylinder was allowed its proper curing time, the steel platform bearing the concrete cylinder was moved to the “boom-box” for instrumentation fitting. Accelerometers were installed and the external strain gages applied. All power and signal wires were routed inside metal-clad water-proof conduits to attenuate signal noise and protect against fragment damage.

To reduce fragmentation of the concrete target, a 5-foot diameter (4-feet high) steel culvert was placed around the concrete cylinder and the annulus was filled with wet sand. The explosive charge was then inserted inside the borehole and held centered in place by three foam rings; the middle ring was at mid-height and the end rings were located 100 mm from the cylinder ends as shown in Figure 11. An RP-83 detonator was used as the initiation device and was placed about 100 mm above center on the axis of symmetry to reduce the chance of detonator fragments striking the accelerometer face.

A materials characterization program was carried out in parallel with the main cylinder tests, with the goal of characterizing the physical properties of the concrete as a function of time and pour number. Using cylindrical samples cast at the same time as the main cylinder, an extensive series of properties was measured, many of them on the same day as the cylinder tests. Unconfined compressive strength, hydrostatic compression, pressure dependence of strength, tensile strength, moisture content and compressional and shear wave speeds were all determined on the same day as the cylinder from the same pour was tested. This was done for each unique pour, as it was anticipated that there would be some variation between pours from different batches. In addition, moisture content and wave speed were determined for samples from the same pour over a 28 day period to determine the temporal variation of these parameters. Microscopic and SEM observations were made on virgin, hydrostatically-loaded, and explosively loaded samples to study the micromechanisms responsible for the irreversible deformation of the concrete. Wave speed measurements were made on the hydrostatically loaded samples post-test to assess the irreversible changes in moduli that occurred under pressures up to 400 MPa. In addition, radial cores were taken from the explosively-loaded cylinders and compressional wave speeds determined as a function of radial position, again with the goal of quantifying the damage caused by the explosive loading.

Table 3. Test Description and Experiment Setup

Test #	Cylinder Designation	Cylinder Description, cure time	Explosive Charge (gr.)	Detonator Type	Test Date
1	Cylinder 1	Developmental, 9 day	837 gm C-4	RP-83	6/24/04
2	Cylinder 2	Developmental, 10 day	262 gm C-4	RP-83	6/25/04
3	Cylinder 7	7 day	78 gm PETN	RP-83	7/7/04
4	Cylinder 8	7 day	156 gm PETN	RP-83	7/8/04
5	Cylinder 9	3 day	156 gm PETN	RP-83	7/9/04
6	Cylinder 10	3 day	156 gm PETN	RP-83	7/12/04
7	Cylinder 6	14 day	156 gm PETN	RP-83	7/13/04
8	Cylinder 5	15 day	156 gm PETN	RP-83	7/14/04
9	Cylinder 3	28 day	156 gm PETN	RP-83	7/15/04
10	Cylinder 4	28 day	156 gm PETN	RP-83	7/15/04

The following series of photos shows the test sequence from prepared concrete cylinder to the end result of detonating 150 g of high explosive. Figure 9 is a photograph of a cylinder with instrumentation complete, positioned in the “boom box”, and ready for placing of the constraining culvert and sand fill. The steel plate used to support the cylinder during pouring and transport can be seen with the numeral “1” painted on. Junction boxes and wiring for the exterior and interior accelerometers are visible at mid-height of the specimen. After the explosives were detonated the specimen was fragmented but not destroyed. A top view (Figure 10a) shows a pattern of radial cracking due to the tensile hoop stresses induced by radial expansion of the cylinder. No circumferential cracking was observed, as might have been expected from the reflected tensile wave from the outer surface. Given the low tensile strength of the concrete, this would seem to indicate that the wet sand was a reasonable impedance match. Note the cratering around the borehole. The picture is suggestively similar to photographs of similar samples after being struck by a penetrator from a Davis gun. From the side, Figure 10b shows that the cylinder was fractured but still coherent. With the added strap stabilizing the fractures the specimen could be transported.

Figure 9. Specimen instrumented and ready for testing.

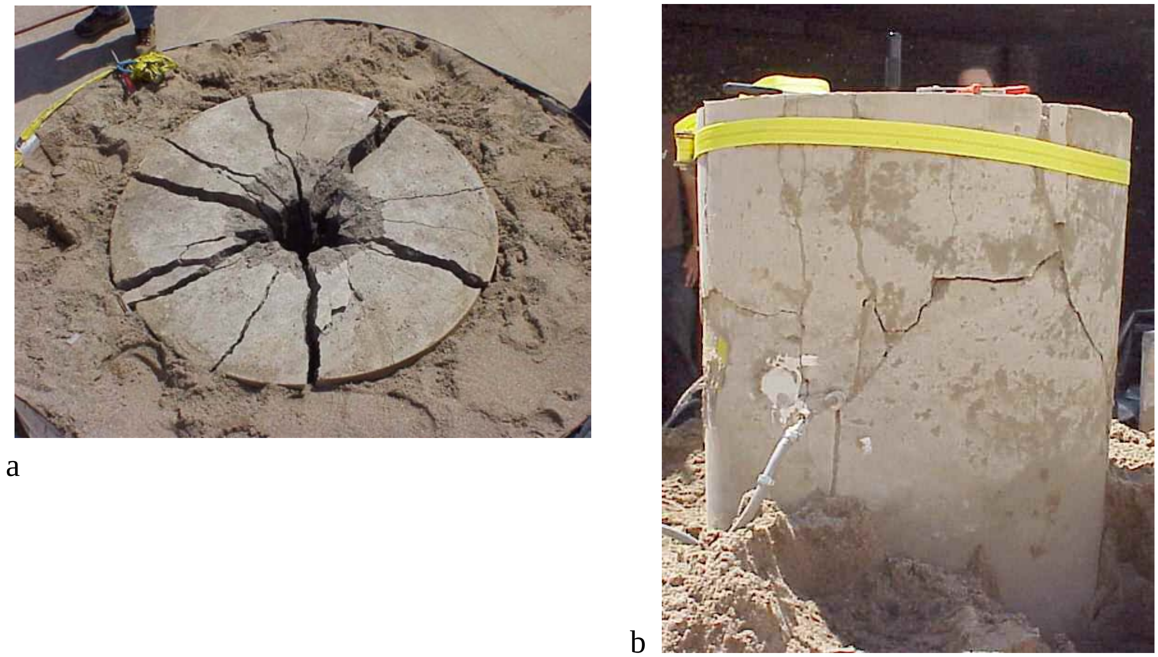

Figure 10. (a) Post-test top view showing radial cracking and near-borehole cratering (b) Post-test side view with specimen stabilized by strap. With radial motion restrained by the sand and culvert, the specimen remained relatively intact.

Acceleration Measurements on Explosively-Loaded Cylinders

Four piezo-resistive accelerometer transducers were employed on most tests (8 accelerometers were employed during Tests 1 and 2). Initially, as shown in Figure 5, two internal accelerometers were located at the inner face of the internal 102-mm (4-inch) diameter borehole, with the inner face of the mounting pod exposed to the explosives placed 51 mm (2 inches) away at the center of the borehole. The two external accelerometers were placed on the external cylinder wall, 457 mm (18 inches) from the center of the charge. Installation was done just prior to testing.

After installation was completed, the culvert and wet sand were put in place as shown in Figure 11, the explosive charge was installed and the firing line connected to the RP-83 pigtail. Standard Arming and Firing Operating Procedures were strictly followed to authorize proper detonation of the explosives charge. Post-test, all signal data were downloaded from the oscilloscopes and electronically archived.

A brief description of each test follows, in the same order as the testing was done. A summary of all results may be found in Table 11. When peak accelerations or velocities are discussed, the value refers to the first peak, as we felt this best represented the material response unaffected by reflected waves. For the early tests, the accelerometers were often driven beyond their range. If the result was not obviously clipped, then the peak value will be reported with the understanding that the accuracy of the measurement is not equal to that of values within the calibrated range. Even when the acceleration could not be determined, it was often possible to determine the arrival time of the wave at each accelerometer which is useful to note as it can be used to calculate a wave velocity for comparison with the values measured in the laboratory. These values may be found in Table 11, along with the calculated apparent wave velocities.

Tests 1 and 2, using Cylinders 1 and 2, were conducted as calibration shots to determine the proper amount of explosives and to determine the proper accelerometer range (see Figure 13 and Figure 14). Very little useful accelerometer data was acquired during these shots.

Test 3, Cylinder 7, was the first test of the planned program and was done 7 days after casting the concrete cylinder. As Figure 15a shows, an accelerometer 51 mm (2 inches) from the charge recorded about 250,000 g’s before clipping. One external accelerometer 457 mm (18 inches away) recorded about 4200 g’s (Figure 15d). The other external accelerometer did not function properly (Figure 15c). Close examination of Figure 15a shows an initial acceleration-deceleration cycle beginning at 56 microseconds, followed by a phase of much higher accelerations. It is tempting to interpret this initial acceleration, which peaked at 35,000 g’s as the “real” acceleration, while the later, much higher, acceleration pulse is an artifact of the extreme environment experienced at the surface of the borehole. Test 4, Cylinder 8, was also tested at 7 days cure age (see Figure 16). Only arrival times could be determined from the accelerometer data.

Test 5, Cylinder 9, (see Figure 17) conducted at 3 days cure age appeared to produce no useful data from the embedded accelerometers, except for arrival times, but one of the external accelerometers recorded 2300 g's (see Figure 17c). As will be discussed in the section Analysis of Experiments, filtering the signal from the 200kg accelerometer embedded at the borehole wall shows an acceleration of about 3400 g's arriving at the correct time.

During the course of the first five shots, we learned that the internal accelerometers were being severely influenced by the shock impulse with extremely high apparent acceleration rates resulting in several transducers being destroyed. In an attempt to protect the accelerometers and acquire data, the two internal accelerometers were moved to positions 151 mm and 203 mm (6 and 8 inches) away from the center of the charge (see Figure 12). This move placed 100 and 150 mm of concrete between the accelerometers and the explosives. Instead of installing the accelerometer pods from the inside-out as was done for the arrangement shown in Figure 5, a 1.5-inch-diameter hole was drilled radially inwards along the mid-height plane to the required depth to allow the accelerometer to be inserted. Plaster compound with impedance matching that of the concrete was then used to backfill the emplacement hole. This arrangement was employed for the remaining of the test series.

The first test completed with the new arrangement was Test 6, Cylinder 10 which was the second cylinder tested at 3 days after pouring. Despite being protected, the poor quality of the signal and low level of acceleration measured by the embedded accelerometer at 152 mm (Figure 18a) indicates the data should be discarded. No signal was received from the accelerometer at 203 mm (Figure 18b) due to a broken wire. One external accelerometer recorded about 3200 g's without clipping. The probable cause of the failure for the embedded accelerometers was difficulty inserting and seating the accelerometers.

The specimen used for Test 7 was Cylinder 6 which had cured 14 days. Figure 19 shows that the accelerometer 151 mm (6 inches) from the explosives recorded about 4200 g's, the accelerometer 203 mm (8 inches) away recorded a much lower 1600 g's (possibly due to improper installation), and the external accelerometers recorded 3000 and 3800 g's. Test 8 used Cylinder 5 which had cured for 15 days. Data for all accelerometers are plotted in Figure 20. The accelerometer positioned 151 mm (6 inches) from the explosives recorded 6200 g's as did the accelerometer at 203 mm (8 inches). Two external accelerometers recorded 4000 and 5000 g's.

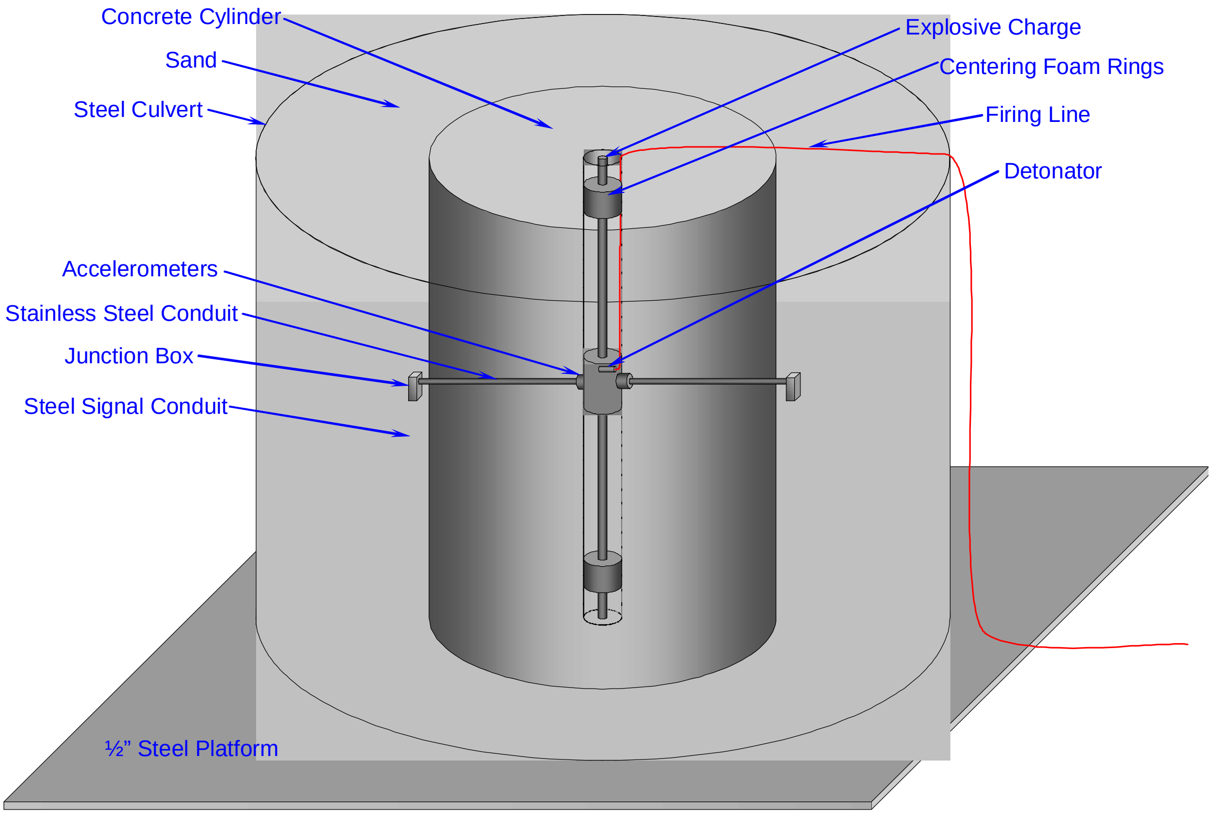

Figure 11. Diagram of complete test assembly. Embedded strain gages are not shown for clarity.

For Test 9, Cylinder 3 was cured 28 days. At 151 mm, the accelerometer experienced approximately 5300 g's, at 203 mm (8 inches) 3300 g's were measured and the external accelerometers recorded 3300 and 4300 g's. Finally, for Test 10, Cylinder 4 (28 days) approximately 5700 g's were measured at 151 mm (6 inches), 8000 g's at 203 mm (8 inches), and one external accelerometer recorded 6000 g's .

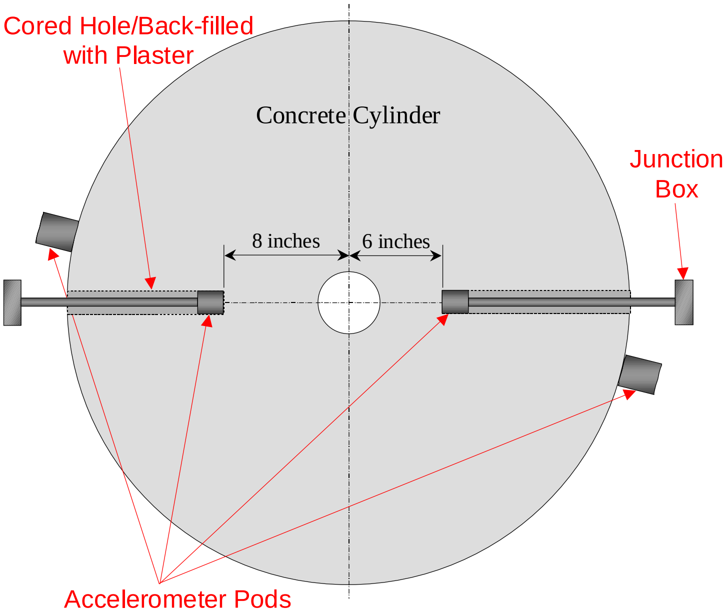

Figure 12. The altered configuration of embedded accelerometers used for Tests 6-10.

Acceleration results

The following set of figures shows all of the useable acceleration data in a consistent format for ease of comparison. Tests are shown in the order conducted, which is not particularly logical since the important variable is cure time, but does allow the stages at which improvements in technique were made to be identified. All accelerations are in g's (1 g= 9.8 m/s^2). Accelerometer ranges are in kilogees, abbreviated kg.

Test 1 – Cylinder 1, 9 day cure time

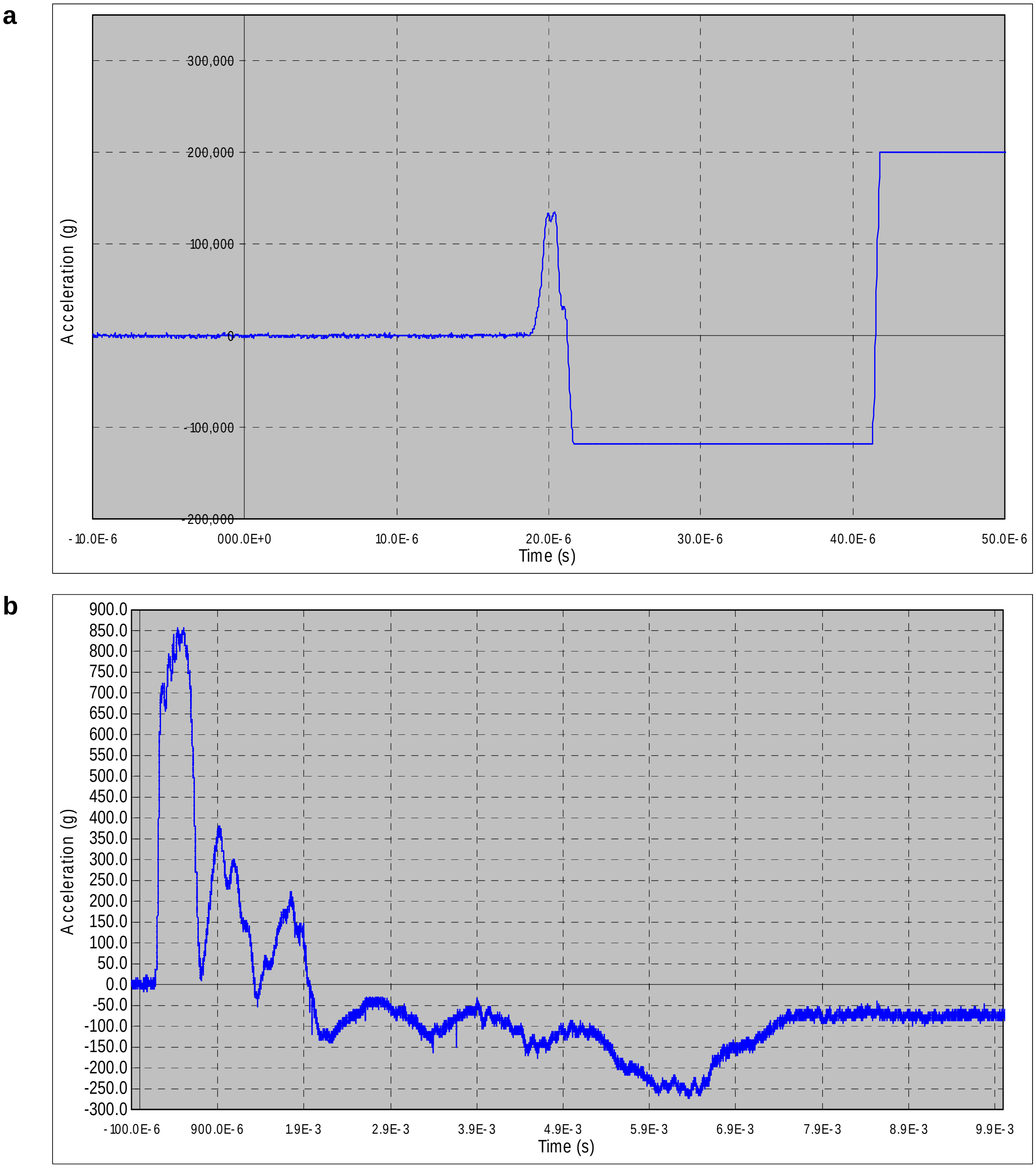

Figure 13. (a) 200kg accelerometer at 51 mm. Only the arrival time is reliable. (b) 2kg exterior accelerometer at 457 mm. All measurements are from center of charge.

Test 2 – Cylinder 2, 10 day cure time

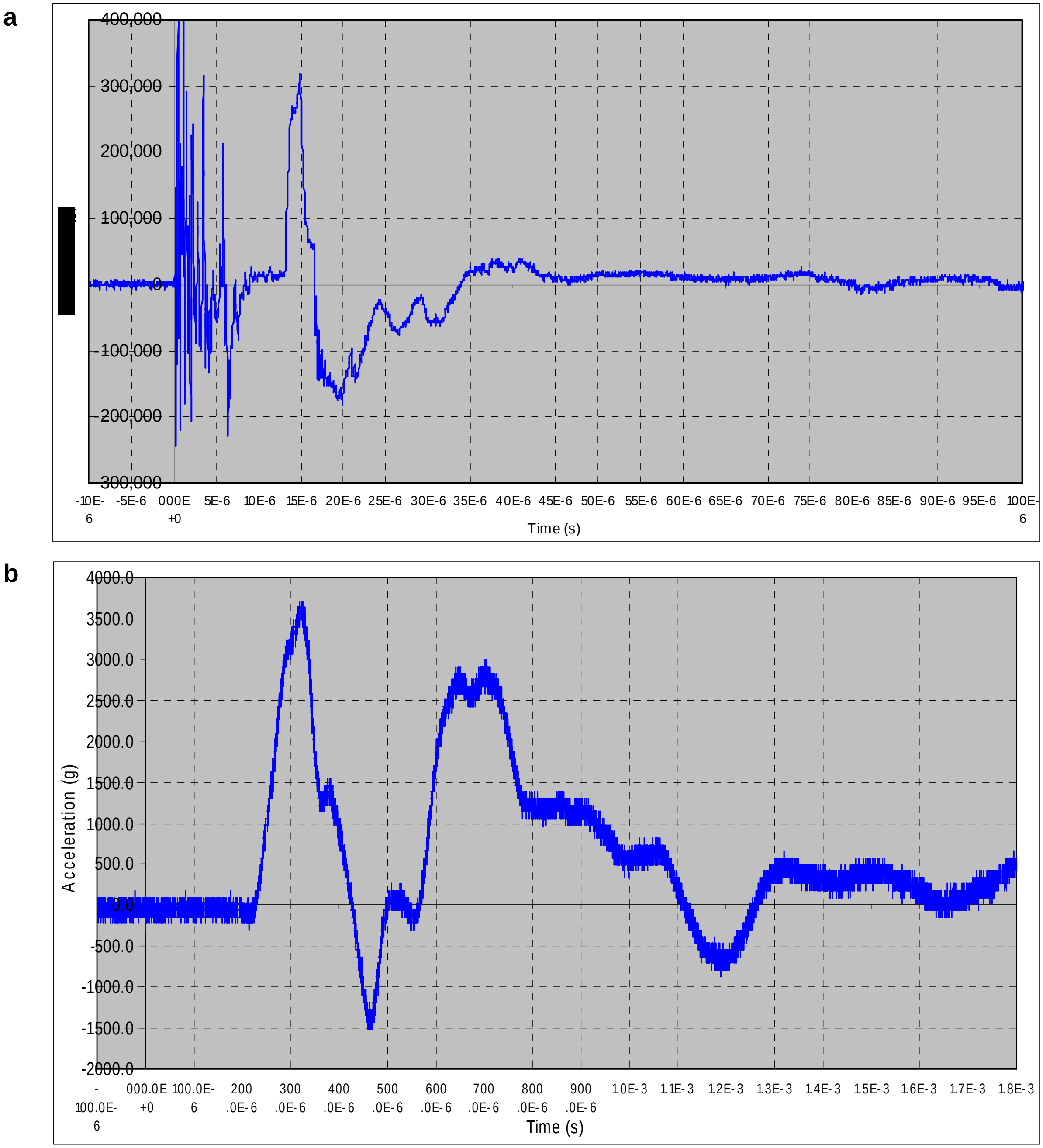

Figure 14. (a) 200kg accelerometer at 51 mm. (b) 2kg exterior accelerometer at 457 mm. All measurements are from center of charge.

Test 3 – Cylinder 7, 7 day cure time

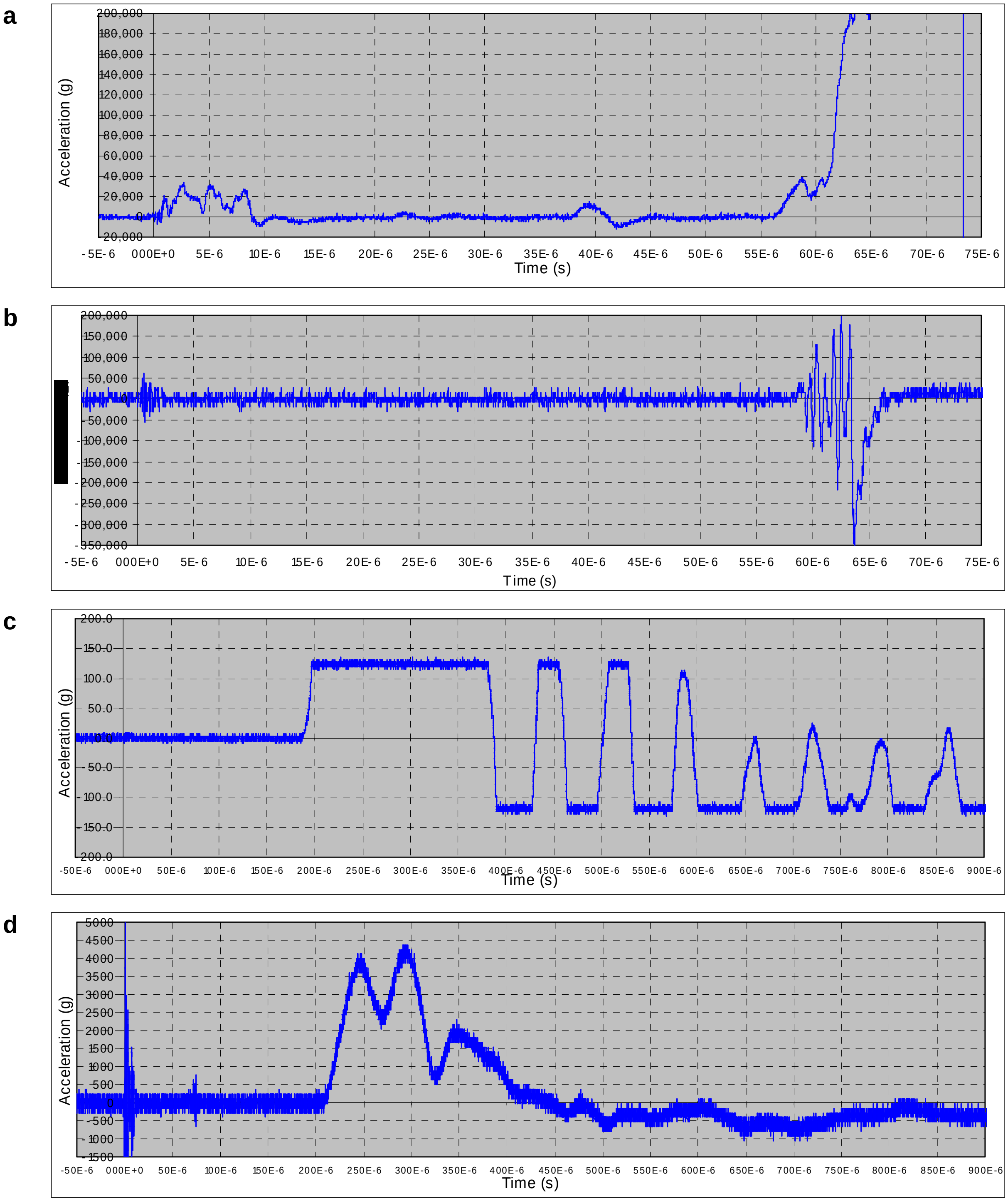

Figure 15. (a) 200kg accelerometer at 51 mm (b) 200kg accelerometer at 51 mm (c) 2kg exterior accelerometer at 457 mm (d) 2kg exterior accelerometer at 457 mm. All distances from center of charge.

Test 4 – Cylinder 8, 7 day cure time

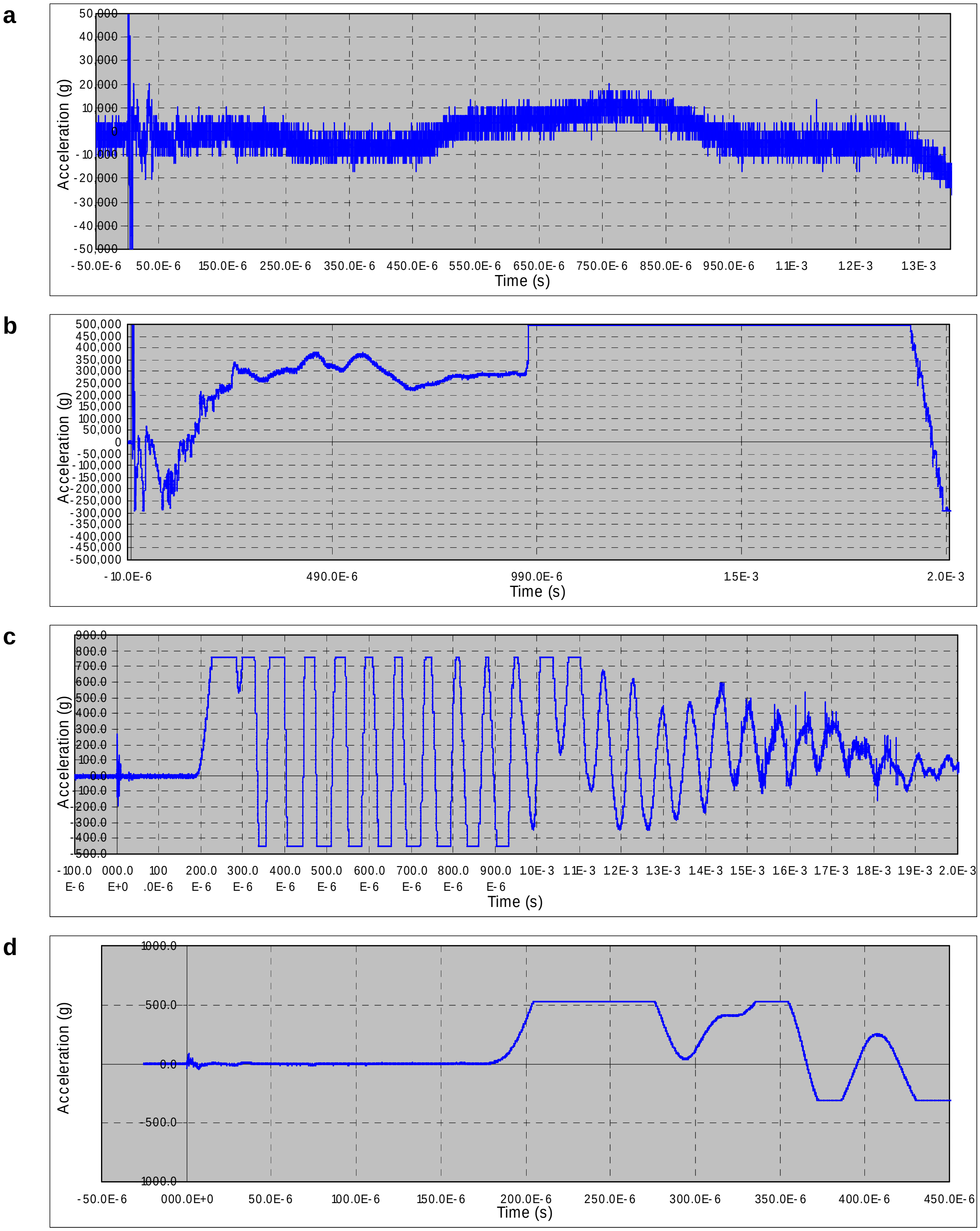

Figure 16. (a) 200kg accelerometer at 51 mm, (b) 200kg accelerometer at 51 mm, (c) 2 kg exterior accelerometer at 457 mm (d) 100g exterior accelerometer at 457 mm. All distances from center of charge.

Test 5 – Cylinder 9, 3 day cure time

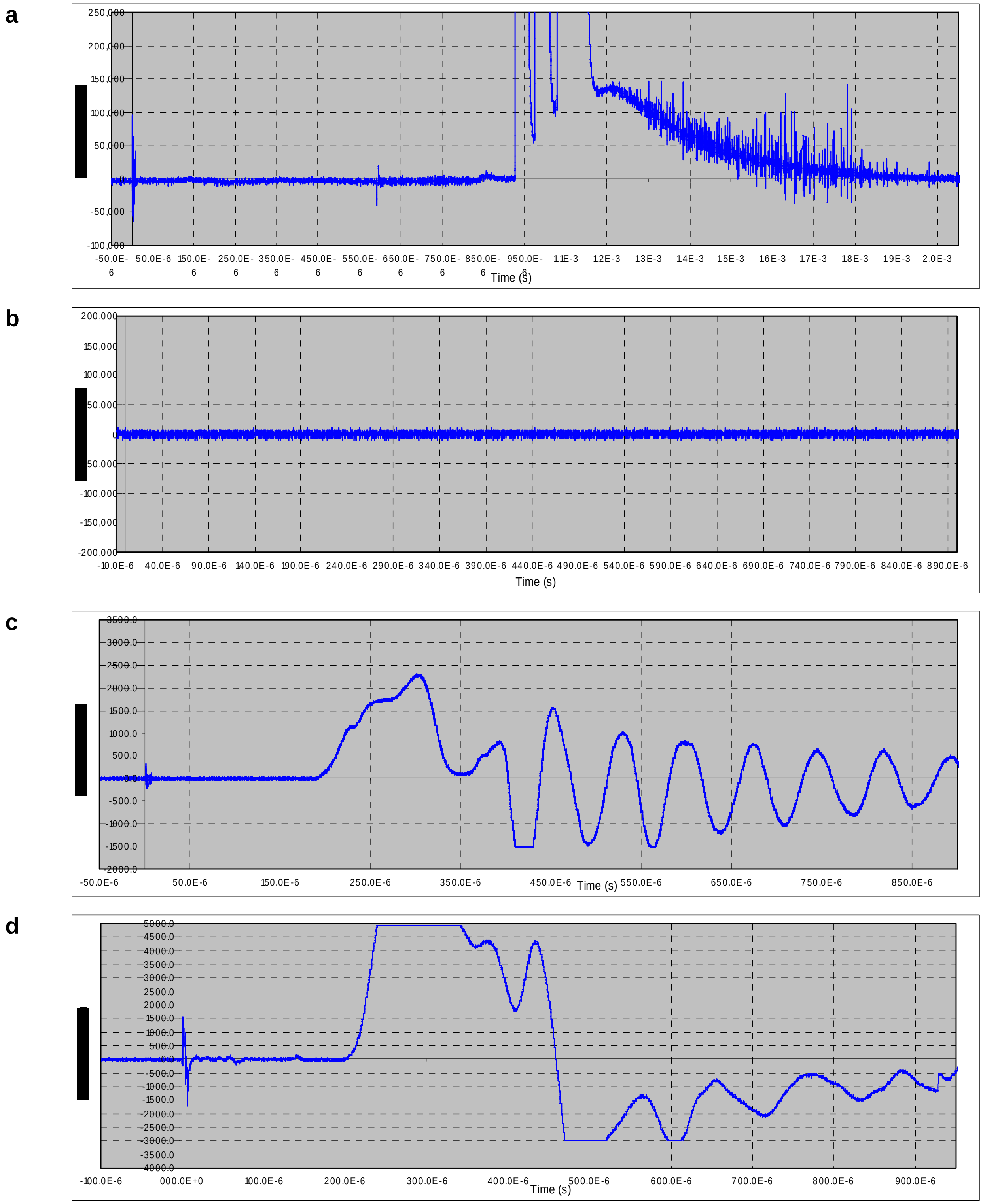

Figure 17. (a) 200kg accelerometer at 51 mm (b) 200kg accelerometer at 51 mm (c) 2kg exterior accelerometer at 457 mm (d) 2kg exterior accelerometer at 457 mm. All distances from center of charge.

Test 6 – Cylinder 10, 3 day cure time

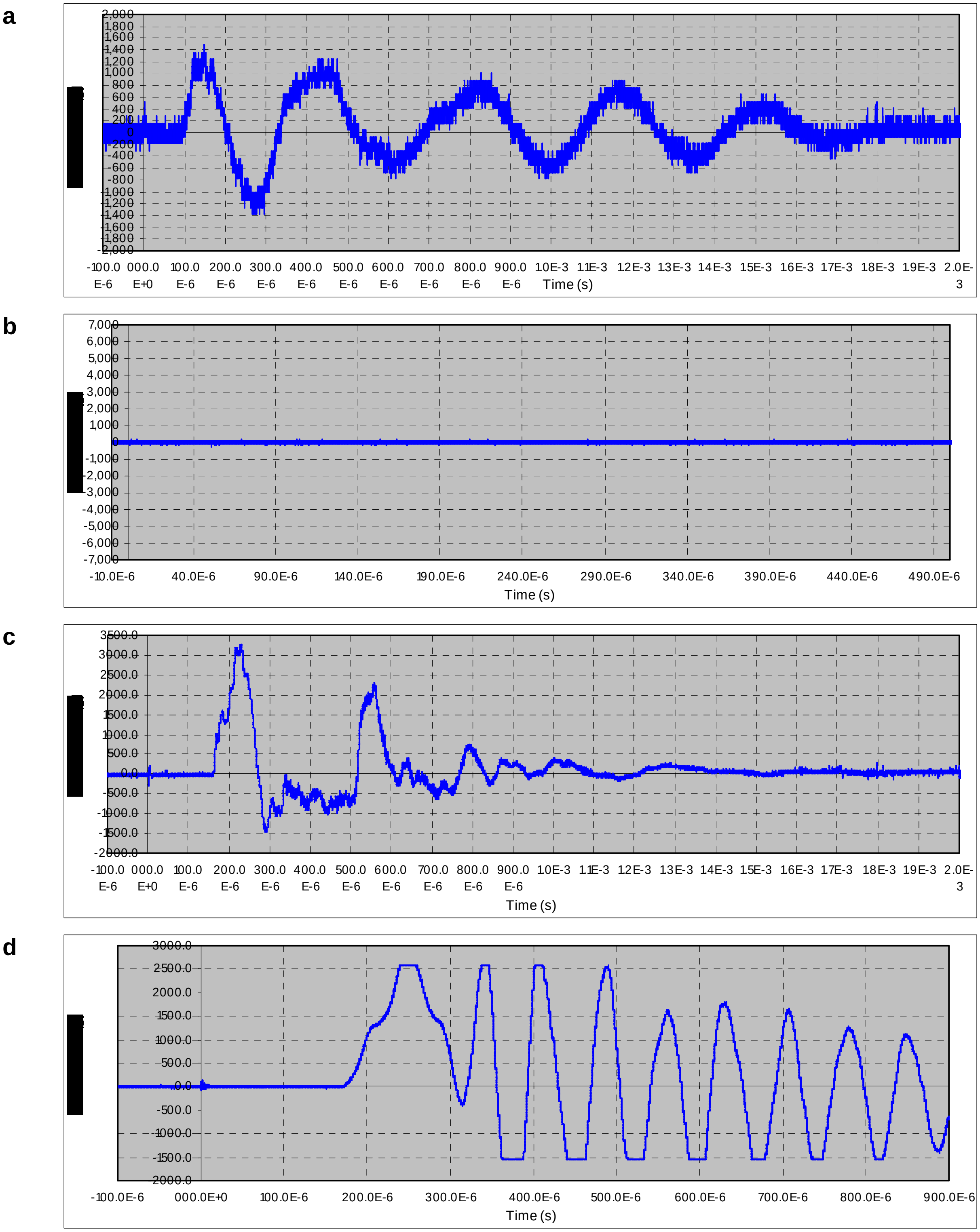

Figure 18. (a) 200kg accelerometer at 152 mm (b) 200kg accelerometer at 203 mm (c) 2kg exterior accelerometer at 457 mm (d) 2kg exterior accelerometer at 457 mm. All distances from center of charge.

Test 7 – Cylinder 6, 14 day cure time

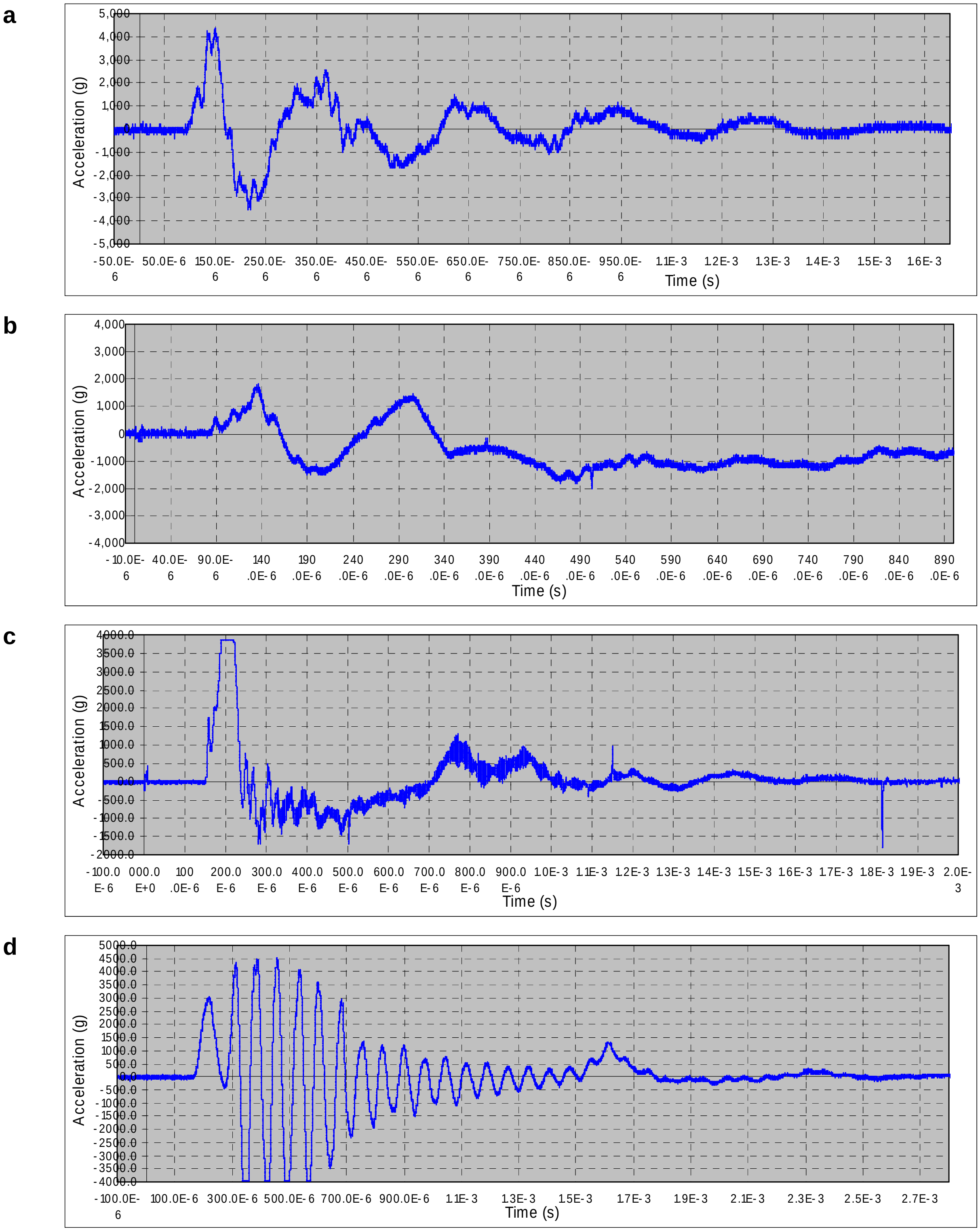

Figure 19. (a) 200kg accelerometer at 152 mm (b) 200kg accelerometer at 203 mm (c) 2kg exterior accelerometer at 457 mm (d) 2kg exterior accelerometer at 457 mm. All distances from center of charge.

Test 8 – Cylinder 5, 15 day cure time

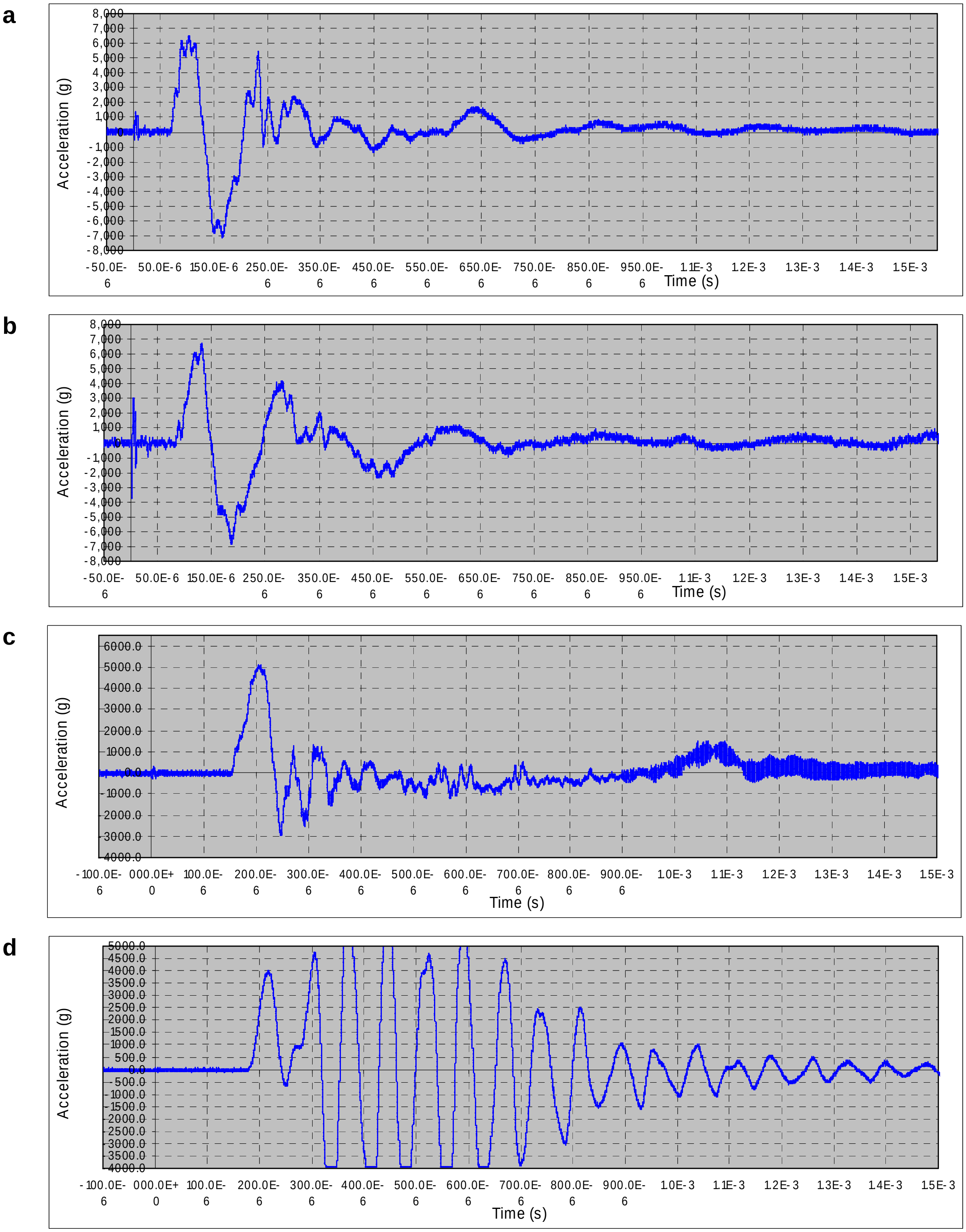

Figure 20. (a) 200kg accelerometer at 152 mm (b) 200kg accelerometer at 203 mm (c) 2kg exterior accelerometer at 457 mm (d) 2kg exterior accelerometer at 457 mm. All distances from center of charge.

Test 9 – Cylinder 3, 28 day cure time

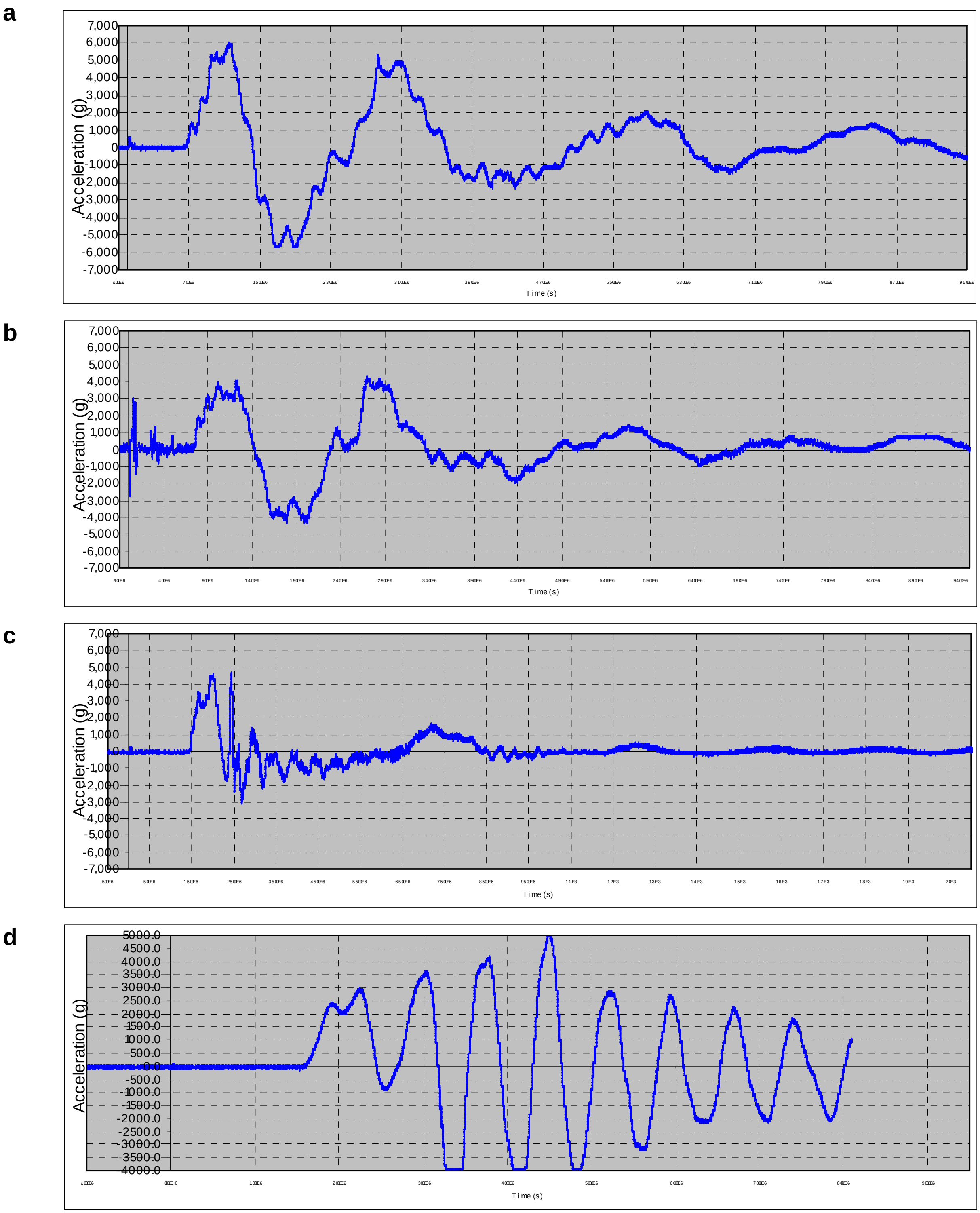

Figure 21. (a) 200kg accelerometer at 152 mm (b) 200kg accelerometer at 203 mm (c) 2kg exterior accelerometer at 457 mm (d) 2kg exterior accelerometer at 457 mm. All distances from center of charge.

Test 10, Cylinder 4, 28 day cure time

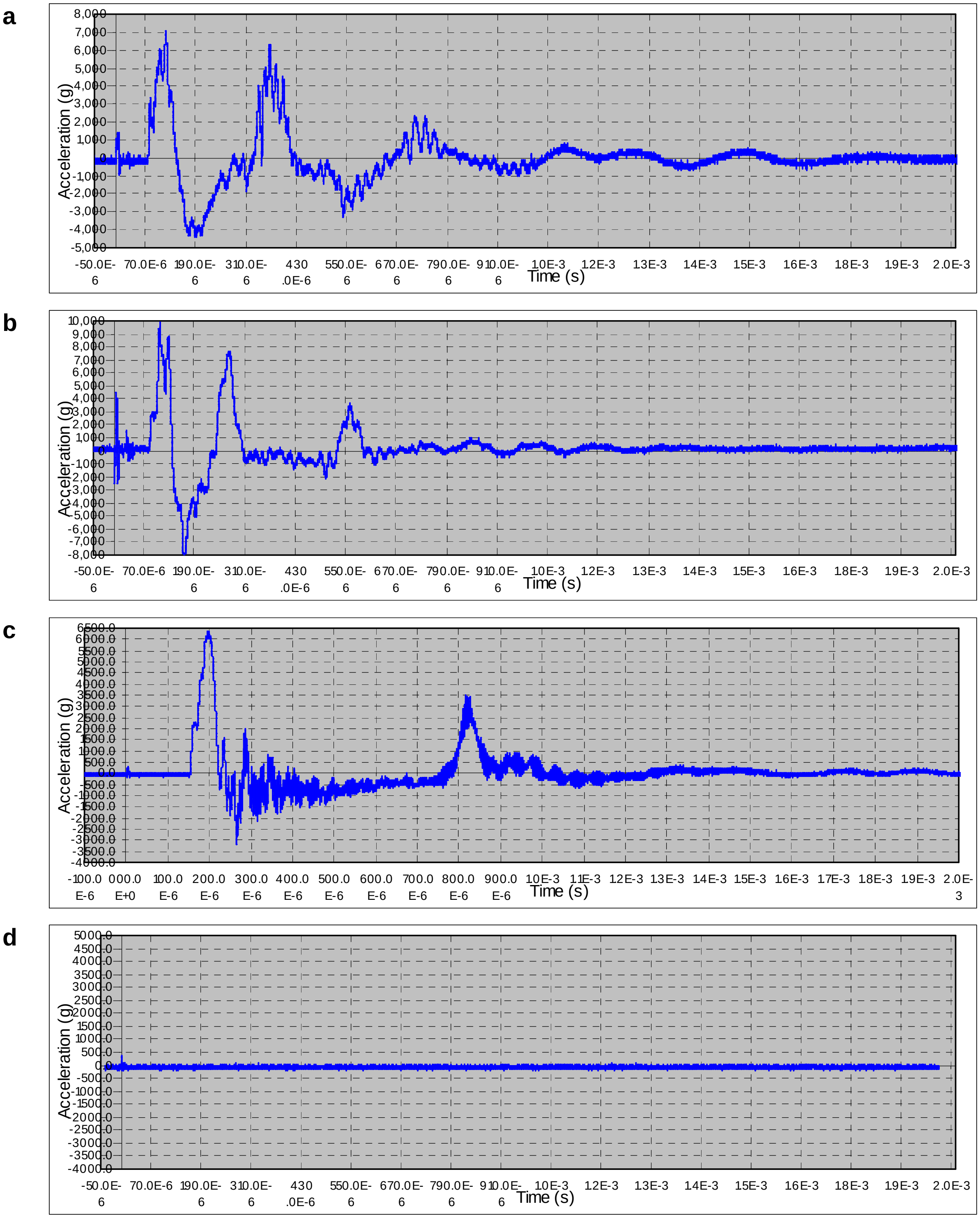

Figure 22. (a) 200kg accelerometer at 152 mm (b) 200kg accelerometer at 203 mm (c) 2kg exterior accelerometer at 457 mm (d) 2kg exterior accelerometer at 457 mm. All distances from center of charge.

Strain Measurements for Explosively-Loaded Cylinders

For each of the 10 cylinders, an attempt was made to measure the complete strain tensor, assuming the principal strains were aligned with the natural coordinate system of the cylinder and the explosives. Two three-axis arrays of strain gages were embedded in the concrete at mid-height, with gages aligned with the circumferential, radial and vertical axes. On the exterior of the cylinders, a two element array of gages was installed, aligned with the circumferential and vertical axes. As discussed earlier, the learning curve was steep, and it was not until the midpoint of the test series that we began to get reliable strain measurements. In what follows, the results of each test are presented in an identical set of three plots. Plot (a) shows the strains from the inner - most array of gages as a function of time, with the sign convention that compressive strain is positive. Accelerations measured by the closest accelerometer are overlaid on the strain plot. Plot (b) is similar, for the strain gage array at mid-distance, but with no accelerometer overlay, as none were in close proximity to this array. Finally, Plot (c) is for the exterior strain gages with the exterior accelerometer overlaid. Distances indicated on each plot show the position of the center of the array, relative to the explosive charge. From the center of the explosive charge, the distance to the center of the innermost array was 191 mm (7.5 in), the array at mid-distance was at 318 mm (12.5 in) and the exterior gages were 457 mm (18 in) distant. If no useful strain data were collected, the corresponding plots were omitted.

A few comments are in order concerning sign conventions and naming and plot ranges. Unfortunately the geomechanics community has chosen a sign convention for compression and tension that is the opposite of that chosen by almost every other discipline; compression is considered to be positive and tension is negative. We have perpetuated this difference and will treat compressive strains as positive and tensile strains as negative. A natural coordinate system is (r, c, z) where r is positive going outward from the cylinder axis, c is the circumferential direction and z of course is parallel to the cylinder axis. Data were collected for about 3 milliseconds after shot time, but the plots are truncated at 500 microseconds. This time interval contains the direct arrival and the arrival of the wave reflected off the free exterior surface that had traveled to the center and returned. It was felt that the sample damage by that time was such that the strains were no longer reflecting material behavior, but the behavior of individual pieces of broken concrete.

Cylinder 1, Test 1, 9 Day, Test Development

No useful strain data were obtained due to grounding problems and cross-coupling with the power supply.

Cylinder 2, Test 2, 10 Day, Test Development

No useful strain data were obtained due to grounding problems and cross-coupling with the power supply.

Cylinder 7, Test 3, 7 Day

No useful strain data were obtained due to grounding problems and cross-coupling with the power supply.

Cylinder 8, Test 4, 7 Day
No useful strain data were obtained due to grounding problems and cross-coupling with the power supply.

Cylinder 9, Test 5, 3 Day
This was the first test that was partially successful in terms of acquiring strain data. The common power supply was replaced by individual batteries for each strain gage circuit and care was taken to ground cable shields and the junction strip where the gage wires were connected to the data system cabling. With these changes we were successful in measuring strains on the exterior of the specimen, but not in the interior. Strains measured on the exterior of the sample (Figure 23a) indicated that ε_z (green line) was slightly tensile, reaching a maximum strain of -1×10^{-4} at the 500 microsecond limit. Circumferential strain, ε_c, (black line) began showing tensile strain at about 200 microseconds, which is the same time as the accelerometer (blue line in Figure 23a, right side axis) mounted on the exterior showed the compressional wave arriving, and reached a peak of $-4.5 \times 10^{-4.}$ A small value for ε_z is consistent with a state of plane strain which would be expected for the cylindrical symmetry of the specimen and of the explosive load. However other tests, discussed below, did not always show small strains in the Z direction. Circumferential strain is expected to be tensile from both the Poisson's effect of the compressive radial stress pulse, and from the increase in diameter as the cylinder expands outward. No data were obtained from the embedded strain gages; only coupled electrical noise was recorded. This gave us the final clue that the wire jig used to mount, orient and stabilize the embedded gages was acting as an antenna, coupling the electromagnetic pulse from the explosive into the gages. In subsequent tests, the jig was grounded and data were typically obtained from all gages.

Cylinder 10, Test 6, 3 Day
A second cylinder with a cure age of 3 days was the first fully successful test we conducted, with data obtained from all strain gages and accelerometers (Figure 24). The innermost gages, centered at 191 mm, show the expected pattern of compression in the radial direction and extension in the axial direction. In the radial direction, the stress pulse caused a compressive strain of roughly 10×10^{-4}; At the same time, axial strain was tensile with a magnitude of -9×10^{-4}. No data were obtained from the circumferential gage. Accelerations recorded by an accelerometer at 152 mm, 40 mm closer to the explosion ((Figure 24c, blue line) show a compressive stress pulse arriving about 10 microseconds earlier, and reaching a peak of 30,000 m/s^2.

Strain gages at the middle array (Figure 24b) tell a confusing story. Radial strain ε_r (red line) was positive, indicating compression as expected. Noise makes it difficult to decide what the baseline strain should be, but it appears to have been about 12×10^{-4} prior to arrival of the stress pulse. Peak radial strain then increased by 14×10^{-4}. Cirumferential strain (black line) was nearly constant with no obvious trend. Circumferential strain should always be tensile. On the other hand, axial strain (green line) did go into tension, starting at a baseline of 3×10^{-4} and peaking at -3×10^{-4} for a net tensile strain of -6×10^{-4}. This is not consistent with plane strain deformation.

Beginning at about 160 microseconds, in agreement with the arrival time of the compressive stress pulse at the accelerometer (Figure 24a, blue line) circumferential strain increased steadily, reaching -6×10^{-4} at 500 microseconds. This is comparable to the strain observed for Cylinder 9. Axial strain ε_z showed an abrupt extension coincident with the arrival of the stress wave. It is likely that a local crack was formed that influenced this gage as the tensile strain is large, occurred abruptly and then remained almost constant even though the accelerometer indicates rapid oscillation of the local deformation.

Cylinder 6, Test 7, 14 Day

Data acquired from Cylinder 6, cured for 14 days, are shown in Figure 25. Seven of the eight strain gages functioned properly and the eighth, measuring ε_z on the exterior, failed in tension when the stress wave arrived. The innermost gage set (Figure 25c) measured compressive strains in the radial and axial directions, and essentially no strain in the circumferential direction. The same pattern of strain was observed at the middle gage set (Figure 25b) making it unlikely that confused wiring or other experimental problems were responsible for the deviation from the expected pattern of compressive radial strain, tensile or near zero axial strain, and tensile circumferential strain. Instead this likely points to an asymmetry in the stress field generated by the explosion. Compressive strains were in excess of $15\text{x}10^{-4}$ at the inner gage set, 191 mm from the explosion shielded by 100 mm of concrete. At the middle gage set, compressive strains were about $6\text{x}10^{-4}$ and on the exterior the initial compressive strains were less than $1\text{x}10^{-4}$ before a long term trend toward tensile strain began. At both the inner and exterior gages, there was good temporal correlation between the onset of strains and the arrival of the stress pulse as indicated by the accelerometers.

Cylinder 5, Test 8, 15 Day

Cylinder 5 was intended to be tested at 14 days, but had to be tested one day later; a one day delay was not expected to materially change the concrete properties at this stage of the curing process. As Figure 26c shows, the sense of strains corresponded exactly to expectations: compression in the radial direction, tensile in the circumferential direction and tensile with small amplitude in the axial direction. Magnitudes were smaller than on Cylinder 6, the other 14 day test; radial and circumferential initial strains were less than $5\text{x}10^{-4}$. The passage of the radial stress pulse is seen in the radial strains; first a compression, beginning at 90 microseconds matching the arrival time from the accelerometer (blue line, Figure 26c), followed by tension as the wave is reflected off the outer free surface and propagates back through the cylinder as a tensile wave. A second passage of the twice reflected wave produced compression starting at about 200 microseconds.

A similar pattern was seen at the middle gage set (Figure 26b). However the exterior gages (Figure 26a) did not behave as expected. Both gages initially went into compression, in exact synchrony with the accelerometer output. We have no good explanation for this unexpected result; at a minimum ε_c should have been tensile. After the initial pulse, both gages did measure small tensile strains.

Cylinder 3, Test 9, 28 Day

The longest cure time studied was 28 days for Cylinders 3 and 4. All gages functioned properly for Cylinder 3, as shown in Figure 27, but with some unexpected results. Radial strain at the inner gage set was tensile which is very difficult to explain (Figure 27c, red line) . As expected, circumferential strain was tensile with an initial amplitude of about $12\text{x}10^{-4}$. Axial strain showed a small, initial tensile strain, and then oscillated around zero strain as would be expected for a plane strain test. At the middle gage set (Figure 27b), strains were in accordance with expectations. Radial strain was initially compressive with small amplitude, but did change over to tensile by 200 microseconds. Both axial and cicumferential strains were initially tensile and remained so, with amplitudes of 6 to $8x10^{-4}$. Axial strains were too large to be consistent with plane strain conditions. At the exterior, an initial compressive in the axial direction returned to near zero, consistent with plane strain. Circumferential strains also showed a clear initial pulse, but tensile in character, followed by a return to near zero with a trend toward tensile. Accelerations reflect a similar pattern (Figure 27a, blue line); a well defined pulse lasting about 100 microseconds, returning to near zero.

Cylinder 4, Test 10, 28 Day

The final test was also done after 28 days of curing. Two of the inner gages malfunctioned, leaving only the circumferential gage. Beginning with the arrival of the stress pulse (Figure 28c, blue line), ε_c became tensile and remained so. At the middle gage set , all three gages went into tension, which is totally unexpected and inexplicable for the radial gage. Finally, the exterior gage set response was consistent with the expectation of a plane strain expansion of the cylinder. Cicumferential strain became negative at the same time the stress pulse arrived (Figure 28a, black and blue lines, respectively) and remained tensile. Axial strain was briefly tensile, but then returned to nearly zero as expected if the cylinder was expanding in plane strain. Examining the magnitude of the initial pulse for circumferential strain, we see -10x 10^{-4} at the inner gages, $-5x10^{-4}$ at the middle set and -2 to -4 x 10^{-4} at the exterior.

Summary of strain gage results

From the symmetry of the loading, we expected that the cylinders would be deformed in plane strain with the strain along the axis of the cylinder, and of the explosive loading the cylinder, being close to zero. In about ½ of the tests this expectation was met, although as discussed above, the axial strain frequently showed a compressive or tensile excursion at the time of arrival of the stress pulse. However other tests, such as Cylinder 3, had axial gages showing strongly tensile strains that did not return to zero. Circumferential strains were the most consistent, nearly always being tensile and remaining tensile. Finally, initial radial strains should always be compressive, barring a major distortion of the loading. The fact that this was not always true is puzzling. Cylinders 3 and 4 both had radial strain gages that indicated an initial and continuing state of tensile strain in the radial direction.

A possible explanation lies in the long period of the strain waves and small amplitude, particularly for the compressional phase. In Figure 27b, the initial radial strain is small and compressional, starting at about 110 microseconds and continuing for 90 microseconds, before being swamped by the much larger tensile wave reflected off the exterior. A low signal-to-noise ratio for the strain gage signals necessitated extensive filtering before useful data could be retrieved. Although reasonable care was taken to avoid phase distortion and the pass band was as wide as possible, it would be easy to obscure a small signal. Indeed, if Figure 28b is examined closely, it is seen that the radial strain (red line) breaks positive when it separates from the negative-going circumferential strain (black line). However, the amplitude is barely more than the noise and in the same frequency range.

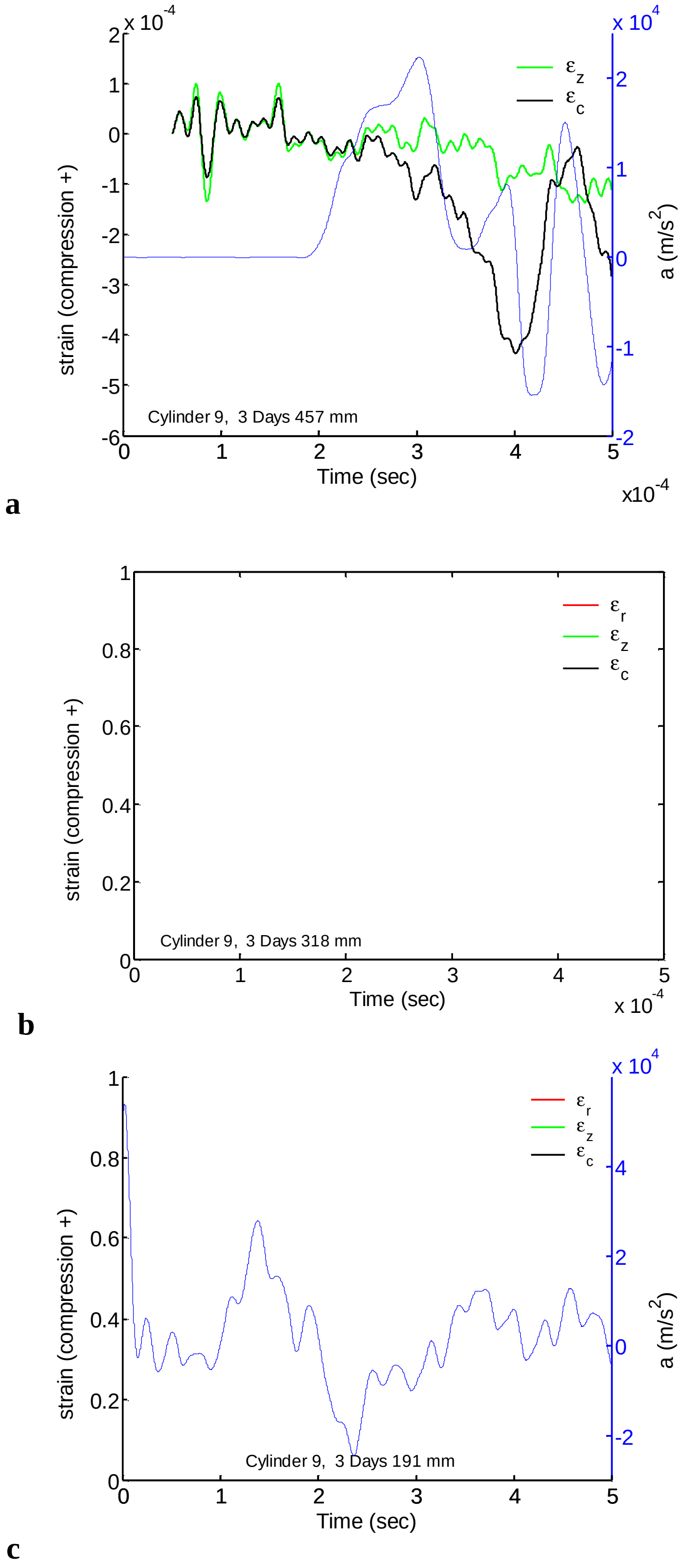

Figure 23. Cylinder 9 – All strains at (a) 457 mm (b) 318 mm (no data) and (c) 191 mm. Line color indicates strain component. Blue line is closest accelerometer (right axis).

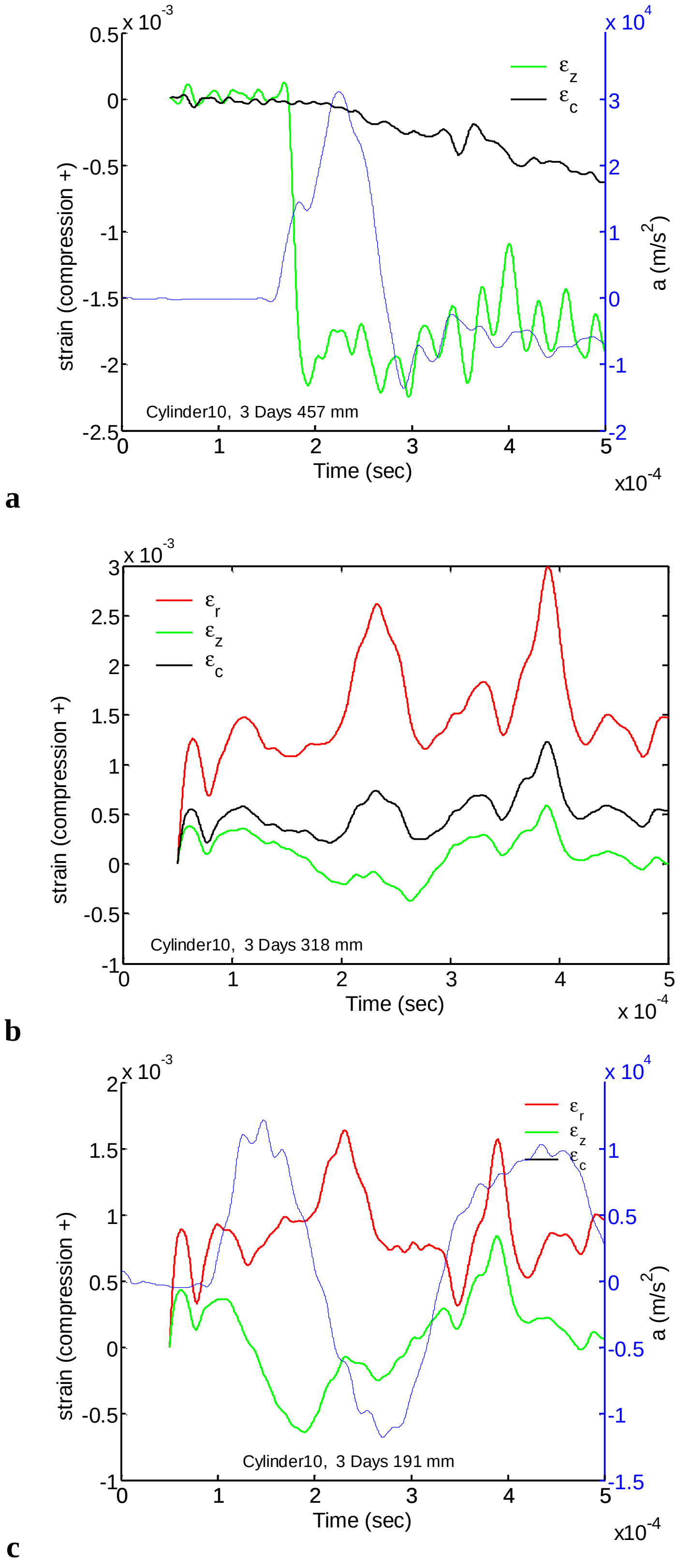

Figure 24. Cylinder 10 – All strains at (a) 457 mm (b) 318 mm and (c)191 mm. Line color indicates strain component. Blue line is closest accelerometer (right axis).

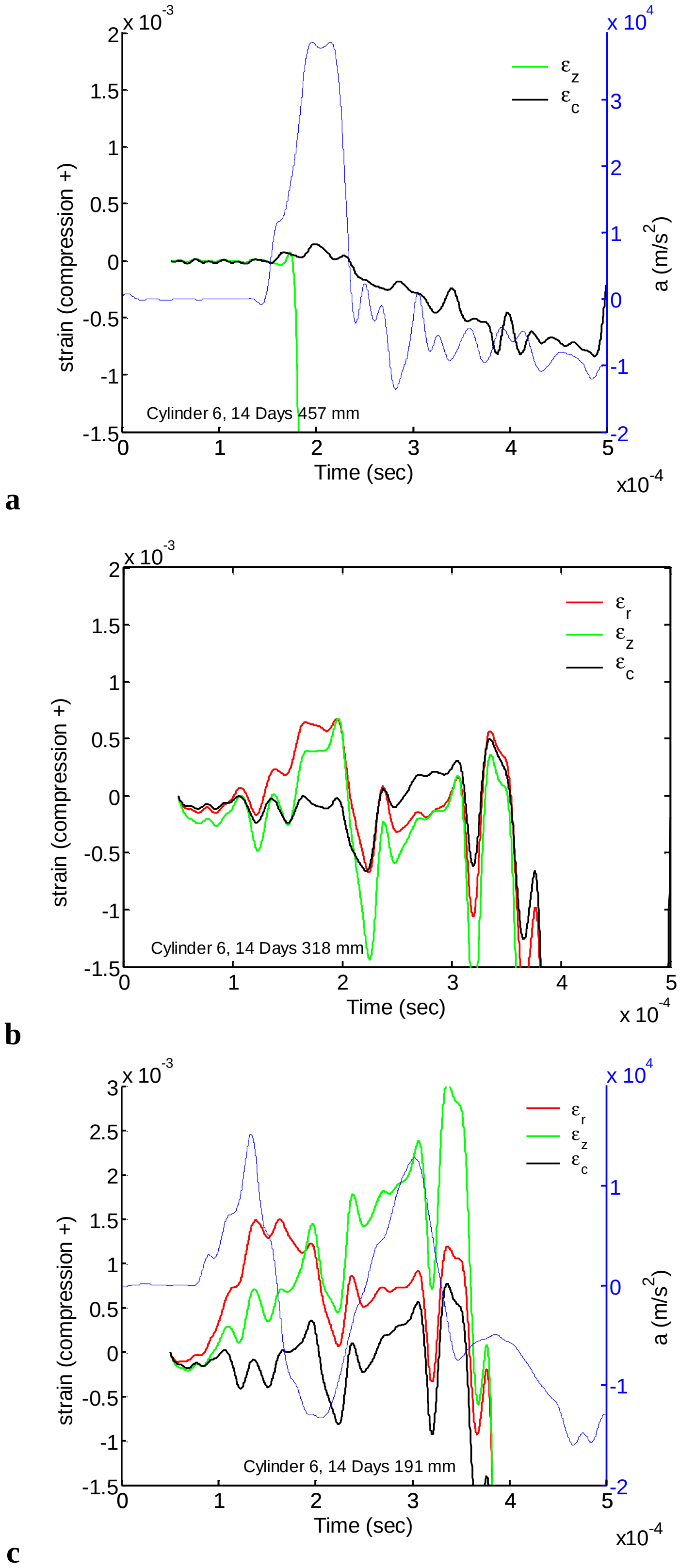

Figure 25. Cylinder 6 – All strains at (a) 457 mm (b) 318 mm and (c) 191 mm. Line color indicates strain component. Blue line is closest accelerometer (right axis).

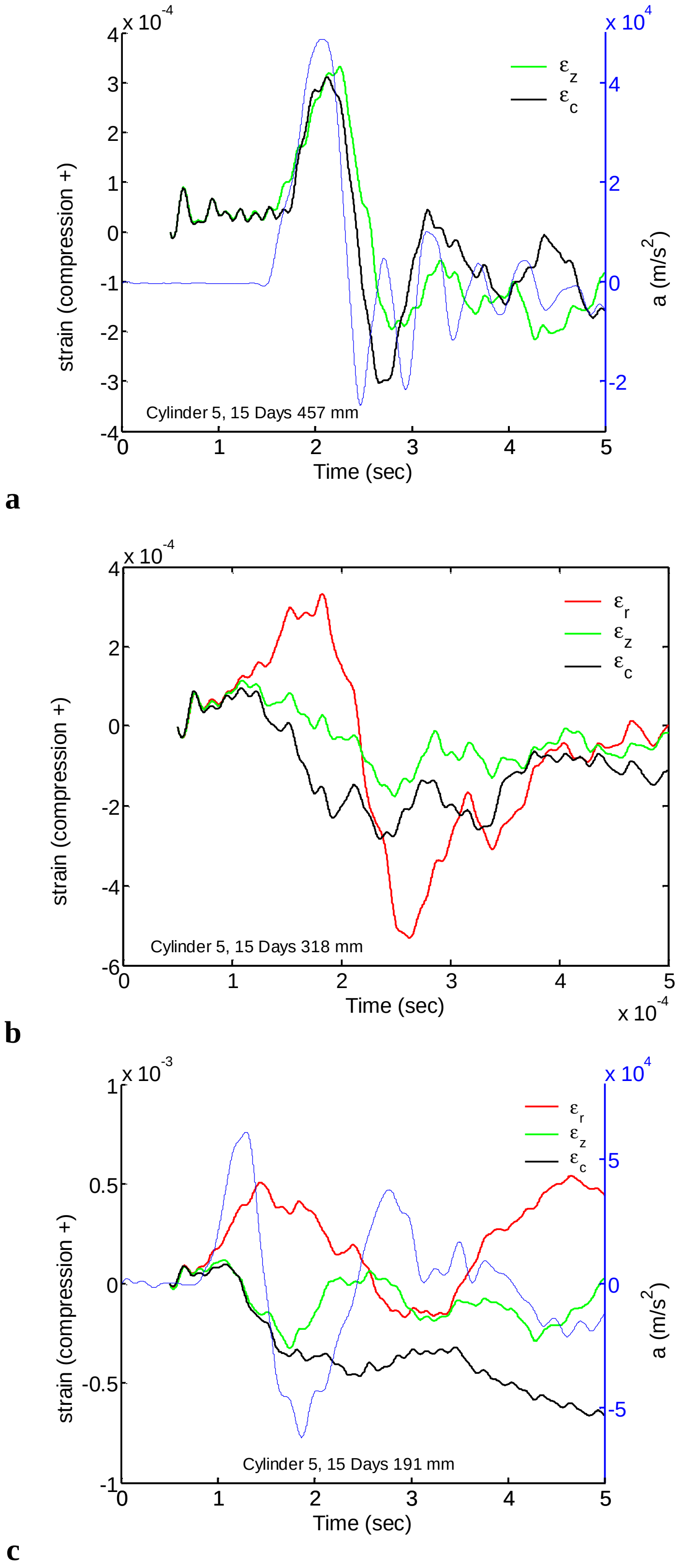

Figure 26. Cylinder 5 – All strains at (a) 457 mm (b) 318 mm and (c) 191 mm. Line color indicates strain component. Blue line is closest accelerometer (right axis).

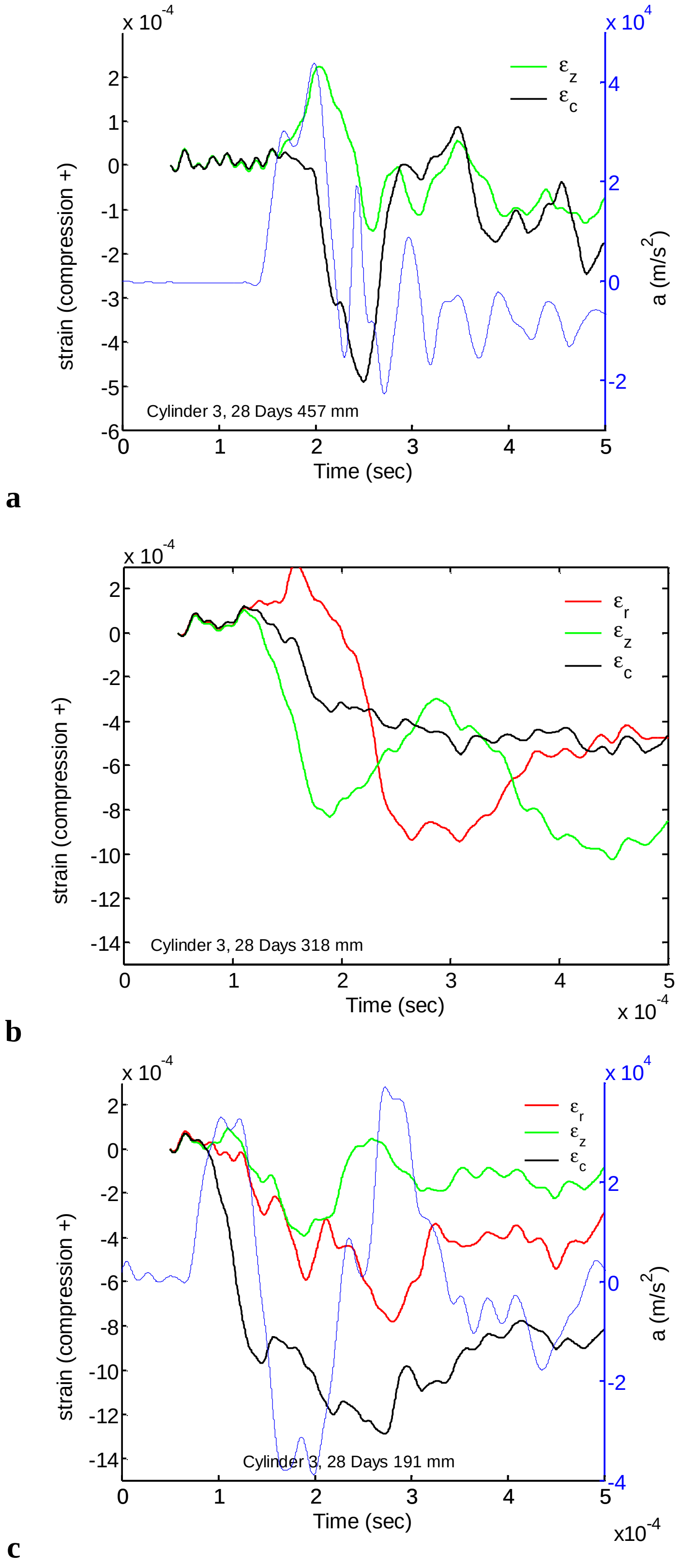

Figure 27. Cylinder 3 – All strains at (a) 457 mm (b) 318 mm and (c) 191 mm. Line color indicates strain component. Blue line is closest accelerometer (right axis).

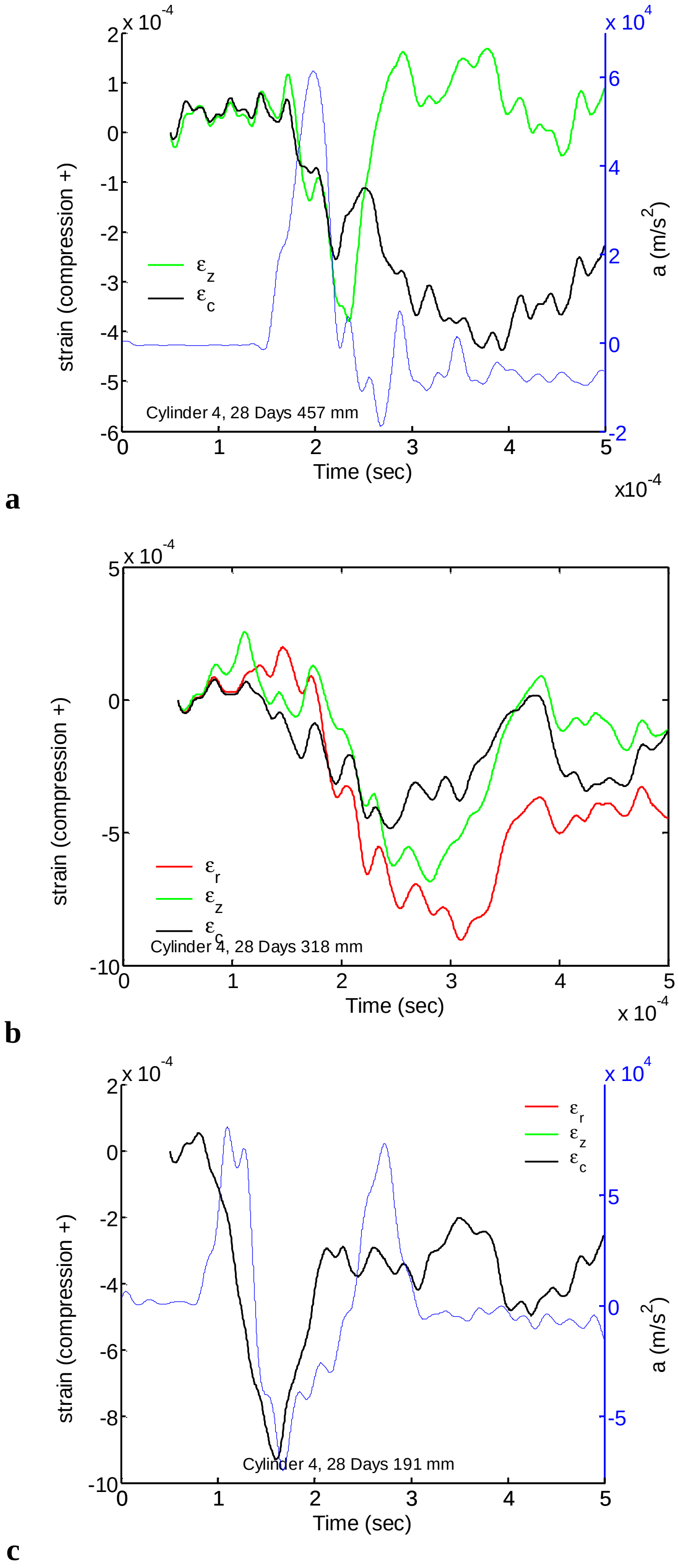

Figure 28. Cylinder 4 – All strains at (a) 457 mm (b) 318 mm and (c) 191 mm. Line color indicates strain component. Blue line is closest accelerometer (right axis).

Porosity and Moisture Content

Porosity, density, and water content measurements

The purposes of the porosity, density, and water content measurements were to:

- provide an inter-pour physical property comparison
- provide a framework to understand and normalize other measurements being made including yield stress, pore volume change during hydrostatic compression and elastic wave speeds.
- monitor the temporal changes in moisture content

The approach taken was to make repeat measurements on multiple samples cast at the time the main test cylinders were poured.

Sample preparation and handling:

Four to ten subsamples (nominal right cylinders of ~3.48 cm diameter, total volume from 40.0-48.0 cm^3) were cast at the same time as the casting of each test cylinder. Specimens were formed by placing the concrete into PVC tubing with duct tape acting as containment at the bottom, vibrated for approximately ten (10) seconds using a steel rod, then tape-sealed until measurement assays were initiated. All samples were kept in sealed plastic bags except during times in which measurements were made. Conditions of storage for the subsamples were similar to the main test cylinders, except for the temperature differentials experienced; subsamples experienced only the small differences expected in a climate-controlled building, while the main test cylinders were exposed to the diurnal cycles of about 20^o C. Packaging for subsamples and main test cylinders were moisture-proof or moisture resistant.

Method:

Mass, volume of solids (using He gas in a pycnometer, following Blum [1997]), and geometric volume (estimated from the diameter and height of each right cylinder) were measured on each subsample, in a respective pour set, on the day of mechanical/explosive testing. Error bounds on these measurements are ± 0.1 g, ± 0.25 cm^3, and ± 0.8 cm^3, respectively. In combination, these errors result in bulk density and porosity measurement errors of ± 0.7% and ± 2.4%, respectively.

To obtain estimates of void space (total porosity) in the concrete, 2 or 3 of the subsamples were placed in an oven and dried at 60 °C for a minimum of 48 hours after mass and volume measurements were made on each respective test day. After temperature equilibration following removal from the oven, mass and volume of solids were remeasured. Mass and volume changes could then be used to determine if the concrete structure had lost water due to evaporative drying or if significant water had been additionally incorporated into the microstructure by chemical reaction over the 48-hour interval. Mass-volume changes indicated that evaporation accounts for the systematic reduction in mass and volume over this period.

Samples from several pours were monitored as a function of cure time to examine the natural evaporative loss in the concrete.

Results:

Table 4 contains measurements and porosity, density (dry, grain, and bulk), and water content expressed as a fraction of total volume. Physical property estimates in highlighted regions (corresponding to the oven-dried samples) are directly computed from the measurements of mass, pycnometer volume and geometric volume; bulk density and water content are inferred from the raw measurements and averaged grain density and porosity of the dried samples. Note that specimens were tested at various ages, so a particular specimen will appear several places for a given pour.

Air-filled Porosity is the normalized volume difference between the *Geom*etric *Vol*ume and *Pyc*nometer *Vol*ume, expressed as a percentage. ρ_{dry} is the *Geom*etric *Vol*ume per mass, ρ_{grn} is the *Pycnometer Vol*ume per mass, and ρ_{wet} is the volume-weighted density average of water-filled porosity (defined as the fraction of total volume that is air-filled after dehydration) and the granular matrix (defined as the solid fraction of total volume after dehydration). *Water content* is calculated by subtracting the *Air-filled Porosity*, at a specified time, from the mean of the final porosity estimates (i.e., those data in bold in the *Air-filled Porosity* column) from the oven-dried samples. The non-bold values in the ρ_{wet} column are the calculated volume-weighted average of the *Air-filled Porosity* (having a density of 0.0 g/cm^3), granular matrix (having a density of ρ_{grn}), and *Water content* (having a density of 1.0 g/cm^3). These data are representative of the in situ density of the concrete on each respective test day (with the caveats discussed below).

Total porosity as a function of pour date is presented in Figure 29a and water content as a function of cure time is shown in Figure 29b. Only two points are shown for the test pour, representing the final measurements after 4 drying cycles. Excluding the test pour (C1/2), the average total porosity of the concrete was 26.4 ± 1.5%, which compares very well with the 25.5 % porosity observed by Warren et al. (2004), whose specification for the concrete mix was used in the present work. The intra-pour sample variability is less than the error bounds (±0.006-0.007 porosity units), meaning the same-pour data are statistically equivalent for all datasets, though there is significant inter-pour variability (e.g., between C8 versus C9).

Water content exhibits more within- and between-pour variability, for a given cure time, than can be explained directly by the total pore volume variation (excluding C1/2). Figure 30 shows that the average water content change is characterized by a drop from ~22% at 3-day cure time, to ~10% at 14-day cure time, to ~5% for a 28-day cured material. The variability in water content, with respect to both intra- and inter-pour measurements, does diminish with cure time--indicating that the effect of a distinct microstructure, imparted at the cast time, controls the early aspects of the evaporative process.

Discussion:

In terms of intra-pour variability, the total volume (porosity) measurements appear to be statistically identical given the error bounds above, except for one outlier associated with C3/4. Inter-pour variability, particularly between pours to be tested for the same cure time (3-day: C9 and C10 and 7-day: C7 and C8) is significant only for the 7-day test. With regard to water content, the variability was approximately a factor of two greater than the differences in total porosity for concrete poured for equivalent cure times. While puzzling, the difference does not obscure the consistent trend in water content as a function of time:

- ~1.2%/day for the 3-14 day period
- ~0.4%/day for the 14-28 day period

We used lab-scale measurements as proxies for the actual test cylinders, which forces consideration of how 'representative' are measurements made on ~48.0 cm^3 subsamples when discussing the water content of the ~795,000 cm^3 concrete specimens. The surface area S to volume V ratios of the two scales is markedly different, with

- S/V ~1.2 for the porosity samples
- S/V ~0.06 for the test cylinders

assuming that all surfaces were exposed to the surrounding air. In fact, the laboratory specimens were sealed on the sides by the PVC cylinders in which they were cast but by duct tape on the ends. With the test cylinders jacketed by the water-proof Sonotube, covered on top by a tarp, and sealed by a steel plate on the bottom, it is not possible to say with certainty that the laboratory measurements are representative of the test cylinders state of saturation. In future work, core samples will be taken directly from the test cylinders to determine saturation state.

Microstructural evidence of similarity is shown in Figure 31. The thin section images, from the split-cores extracted from tested cylinders, represent the 3/7/14/28-day cure stages and thus document the consistency in composition, porosity systematics, and cement-grain bonding. Thin sections from the untested 4”-diameter samples (used for velocity measurements) show essentially identical structural characteristics.

Table 4. Porosity and moisture content of concrete

specimen	**date poured**	**Test date**	**age**	**dry?**	**mass** g	**Pyc Vol** cm^3	**Geom Vol** cm^3	**Air-filled Porosity** vol %	ρ_{dry} g/cm^3	ρ_{grn} g/cm^3	ρ_{wet} g/cm^3	**Water content** vol %
TEST Cylinders 1,2												
C-1-J	6/15	06/18	3	N	95.80	40.27	44.74	10.0	---	---	2.14	11.8
C-1-M	6/15	06/18	3	N	93.67	38.04	43.13	11.8	---	---	2.12	10.0
C-1-K	6/15	06/18	3	N	80.65	34.19	37.45	8.7	---	---	2.15	13.1
C-1-L	6/15	06/18	3	N	94.26	39.14	43.57	10.2	---	---	2.13	11.6
C-1-J	6/15	06/22	7	**Y**	88.91	34.95	44.74	**21.9**	**1.99**	**2.54**	**2.21**	
C-1-M	6/15	06/22	7	**Y**	87.54	34.33	43.13	**20.4**	**2.03**	**2.55**	**2.23**	
C-1-K	6/15	06/22	7	N	78.90	31.85	37.45	14.9	---	---	2.09	6.9
C-1-L	6/15	06/22	7	N	92.60	37.54	43.57	13.8	---	---	2.10	8.0
C-1-J	6/15	06/25	10	**Y**	88.81	34.58	44.74	**22.7**	**1.99**	**2.57**	**2.21**	
C-1-M	6/15	06/25	10	**Y**	87.41	34.15	43.13	**20.8**	**2.03**	**2.56**	**2.23**	
C-1-K	6/15	06/25	10	N	78.75	32.10	37.45	14.3	---	---	2.09	7.5
C-1-L	6/15	06/25	10	N	92.48	37.44	43.57	14.1	---	---	2.09	7.7
C-1-J	6/15	06/29	14	**Y**	88.85	34.49	44.74	**22.9**	**1.99**	**2.58**	**2.22**	
C-1-M	6/15	06/29	14	**Y**	87.44	33.91	43.13	**21.4**	**2.03**	**2.58**	**2.24**	
C-1-K	6/15	06/29	14	N	78.33	30.95	37.45	17.3	---	---	2.06	4.5
C-1-L	6/15	06/29	14	N	92.05	36.72	43.57	15.7	---	---	2.08	6.1
C-1-J	6/15	07/13	28	**Y**	88.85	34.49	44.74	**22.9**	**1.99**	**2.58**	**2.22**	
C-1-M	6/15	07/13	28	**Y**	87.44	33.91	43.13	**21.4**	**2.03**	**2.58**	**2.24**	

specimen	**date poured**	**Test date**	**age**	**dry?**	**mass** g	**Pyc Vol** cm^3	**Geom Vol** cm^3	**Air-filled Porosity** vol %	ρ_{dry} g/cm^3	ρ_{grn} g/cm^3	ρ_{wet} g/cm^3	**Water content** vol %
C-1-K	6/15	07/13	28	N	78.04	30.73	37.45	17.9	---	---	2.06	3.9
C-1-L	6/15	07/13	28	N	91.77	36.29	43.57	16.7	---	---	2.07	5.1
28 DAY Cylinders 3,4												
C-3-M	6/17	06/29	12	N	95.15	39.27	45.22	13.2	---	---	2.03	11.8
C-3-N	6/17	06/29	12	N	96.30	41.06	46.31	11.3	---	---	2.05	13.7
C-3-O	6/17	06/29	12	N	98.17	41.90	48.00	12.7	---	---	2.04	12.3
C-3-M	6/17	07/01	14	**Y**	88.79	34.64	45.22	**23.4**	**1.96**	**2.56**	**2.20**	
C-3-N	6/17	07/01	14	**Y**	88.21	34.58	46.31	**25.3**	**1.90**	**2.55**	**2.16**	
C-3-O	6/17	07/01	14	**Y**	89.97	35.36	48.00	**26.3**	**1.87**	**2.54**	**2.14**	
C-3-J	6/17	07/01	14	N	91.38	38.59	45.22	14.7	---	---	2.02	10.3
C-3-K	6/17	07/01	14	N	90.59	37.44	44.37	15.6	---	---	2.01	9.4
C-3-L	6/17	07/01	14	N	92.18	38.22	44.73	14.6	---	---	2.02	10.4
C-3-J	6/17	07/15	28	N	89.21	36.07	45.22	20.2	---	---	1.96	4.8
C-3-K	6/17	07/15	28	N	89.17	35.85	44.37	19.2	---	---	1.97	5.8
C-3-L	6/17	07/15	28	N	90.84	36.35	44.73	18.7	---	---	1.98	6.3
14 DAY Cylinders 5,6												
C-5-L	6/29	07/06	7	N	90.63	39.78	43.60	8.8	---	---	2.06	17.0
C-5-M	6/29	07/06	7	N	99.04	42.58	47.71	10.8	---	---	2.04	15.0
C-5-N	6/29	07/06	7	N	94.64	40.03	45.70	12.4	---	---	2.03	13.4
C-5-P	6/29	07/06	7	N	94.27	40.21	45.45	11.5	---	---	2.03	14.3
C-5-J	6/29	07/06	7	N	94.08	40.93	45.00	9.0	---	---	2.06	16.8
C-5-Q	6/29	07/06	7	N	94.52	40.44	46.19	12.4	---	---	2.03	13.4
C-5-L	6/29	07/09	10	**Y**	82.40	32.30	43.60	**25.9**	**1.89**	**2.55**	**2.15**	
C-5-M	6/29	07/09	10	**Y**	90.47	35.46	47.71	**25.7**	**1.90**	**2.55**	**2.15**	
C-5-N	6/29	07/09	10	**Y**	86.44	33.82	45.70	**26.0**	**1.89**	**2.56**	**2.15**	
C-5-P	6/29	07/09	10	N	94.12	40.66	45.45	10.5	---	---	2.04	15.3
C-5-J	6/29	07/09	10	N	93.82	40.35	45.00	10.3	---	---	2.05	15.5
C-5-Q	6/29	07/09	10	N	94.34	40.33	46.19	12.7	---	---	2.02	13.1
7 DAY Cylinder 7												
C-7-K	6/30	07/07	7	N	95.43	42.35	44.16	4.1	---	---	2.10	23.5
C-7-L	6/30	07/07	7	N	96.26	42.95	45.71	6.0	---	---	2.08	21.6
C-7-M	6/30	07/07	7	N	95.49	42.85	45.46	5.7	---	---	2.08	21.9
C-7-O	6/30	07/07	7	N	93.77	41.80	44.07	5.2	---	---	2.09	22.4
C-7-K	6/30	07/09	9	N	95.07	42.07	44.16	4.7	---	---	2.09	22.9
C-7-L	6/30	07/09	9	N	95.45	41.84	45.71	8.5	---	---	2.05	19.1
C-7-M	6/30	07/09	9	**Y**	83.98	32.62	45.46	**28.2**	**1.85**	**2.57**	**2.13**	
C-7-O	6/30	07/09	9	**Y**	82.88	32.20	44.07	**26.9**	**1.88**	**2.57**	**2.15**	
7 DAY Cylinder 8												
C-8-J	7/1	07/08	7	N	91.96	39.86	44.45	10.3	---	---	2.06	14.9
C-8-K	7/1	07/08	7	N	91.25	39.75	43.48	8.6	---	---	2.08	16.6
C-8-L	7/1	07/08	7	N	91.51	39.95	43.88	9.0	---	---	2.07	16.2
C-8-M	7/1	07/08	7	N	93.69	41.73	44.57	6.4	---	---	2.10	18.8
C-8-J	7/1	07/10	9	N	91.80	39.56	44.45	11.0	---	---	2.05	14.2
C-8-K	7/1	07/10	9	N	91.08	39.48	43.48	9.2	---	---	2.07	16.0
C-8-L	7/1	07/10	9	**Y**	83.62	32.76	43.88	**25.3**	**1.91**	**2.55**	**2.16**	

specimen	**date poured**	**Test date**	**age**	**dry?**	**mass** g	**Pyc Vol** cm^3	**Geom Vol** cm^3	**Air-filled Porosity** vol %	ρ_{dry} g/cm^3	ρ_{grn} g/cm^3	ρ_{wet} g/cm^3	**Water content** vol %
C-8-M	7/1	07/10	9	**Y**	85.26	33.37	44.57	**25.1**	**1.91**	**2.56**	**2.16**	
3 DAY Cylinder 9												
C-9-J	7/6	07/09	3	N	96.00	42.70	45.44	6.0	---	---	2.07	22.4
C-9-K	7/6	07/09	3	N	91.08	40.29	43.20	6.7	---	---	2.06	21.7
C-9-L	7/6	07/09	3	N	99.05	44.32	46.20	4.1	---	---	2.09	24.3
C-9-M	7/6	07/09	3	N	90.23	39.71	43.79	9.3	---	---	2.03	19.1
C-9-N	7/6	07/09	3	N	97.15	43.85	46.61	5.9	---	---	2.07	22.5
C-9-M	7/6	07/12	6	**Y**	80.50	31.32	43.79	**28.5**	**1.84**	**2.57**	**2.12**	
C-9-N	7/6	07/12	6	**Y**	86.02	33.40	46.61	**28.3**	**1.85**	**2.58**	**2.13**	
3 DAY Cylinder 10												
C-10-J	7/9	07/12	3	N	95.57	43.08	45.90	6.1	---	---	2.10	21.2
C-10-K	7/9	07/12	3	N	94.69	41.98	46.42	9.6	---	---	2.07	17.7
C-10-L	7/9	07/12	3	N	101.03	44.35	48.62	8.8	---	---	2.08	18.5
C-10-M	7/9	07/12	3	N	94.28	41.19	44.92	8.3	---	---	2.08	19.0
C-10-L	7/9	07/15	6	**Y**	91.32	35.16	48.62	**27.7**	**1.88**	**2.60**	**2.16**	
C-10-M	7/9	07/15	6	**Y**	85.48	32.83	44.92	**26.9**	**1.90**	**2.60**	**2.17**	

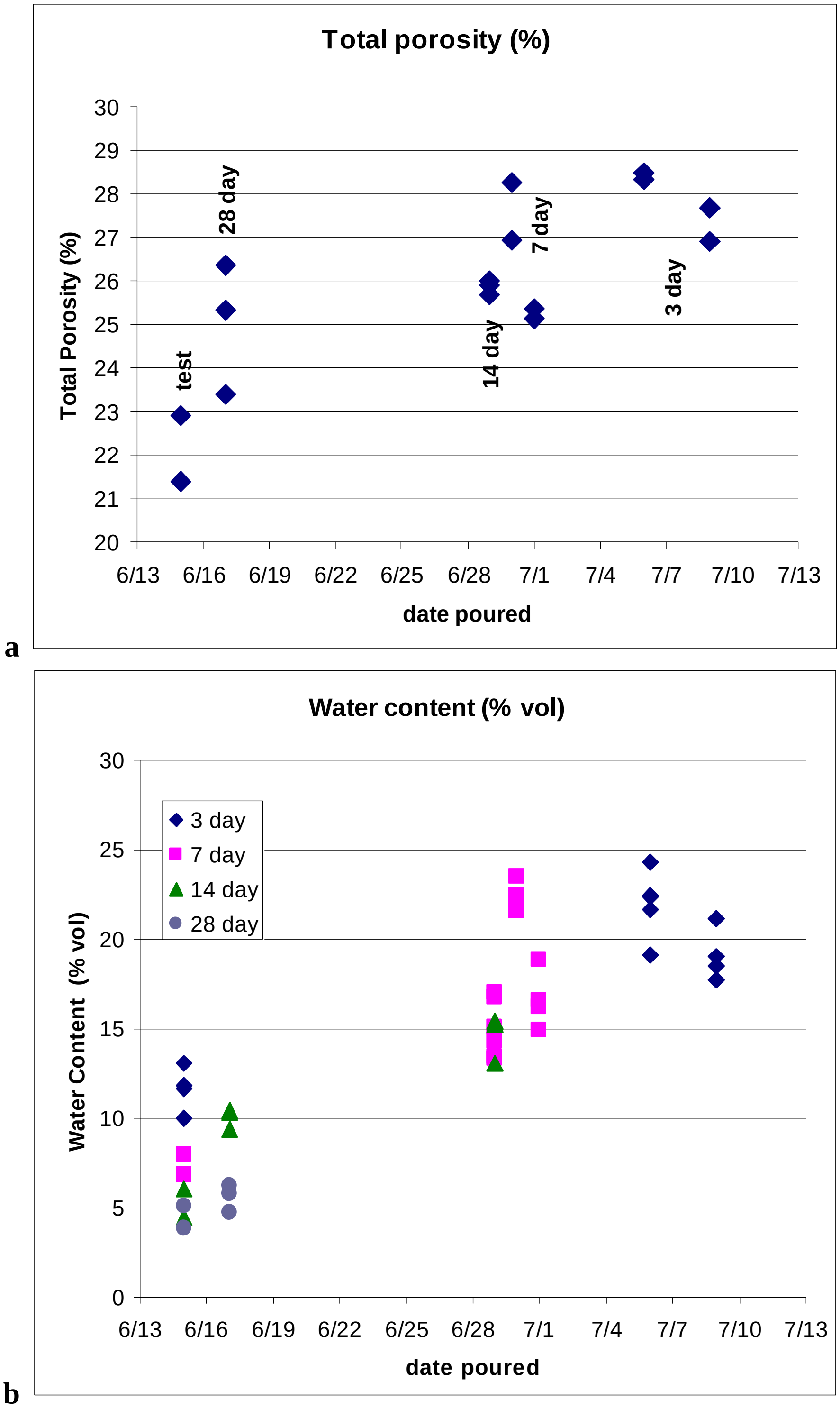

Figure 29. (a) Total porosity and (b) moisture content for each of the distinct concrete pours plotted versus the pour date. Age at time of testing is shown by colored symbols in (b) diamonds for 3 day, squares for 7 day, triangles for 14 day and circles for 28 day.

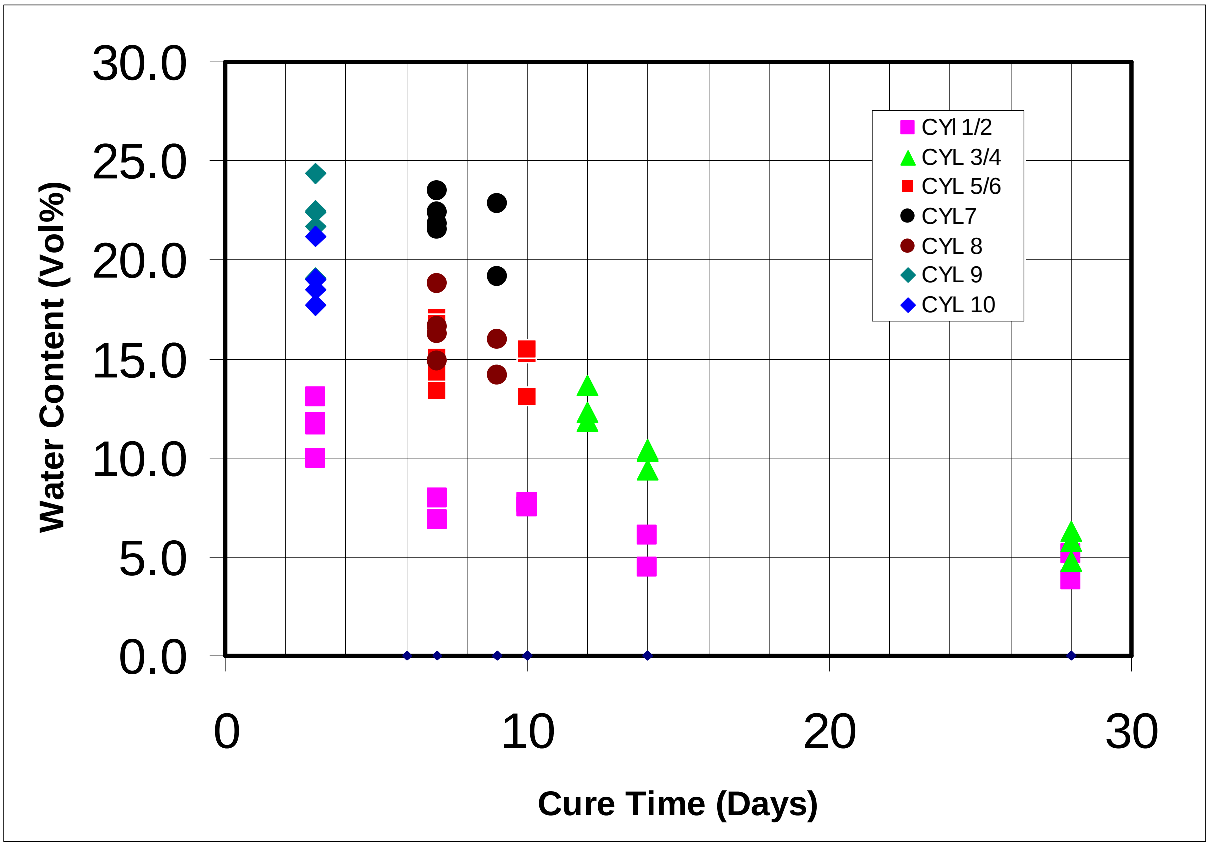

Figure 30. Water content of samples as a function of cure time showing a steady decrease in moisture content. Note that Cylinders 1 and 2 were anomalously dry, especially in the early stages of curing.

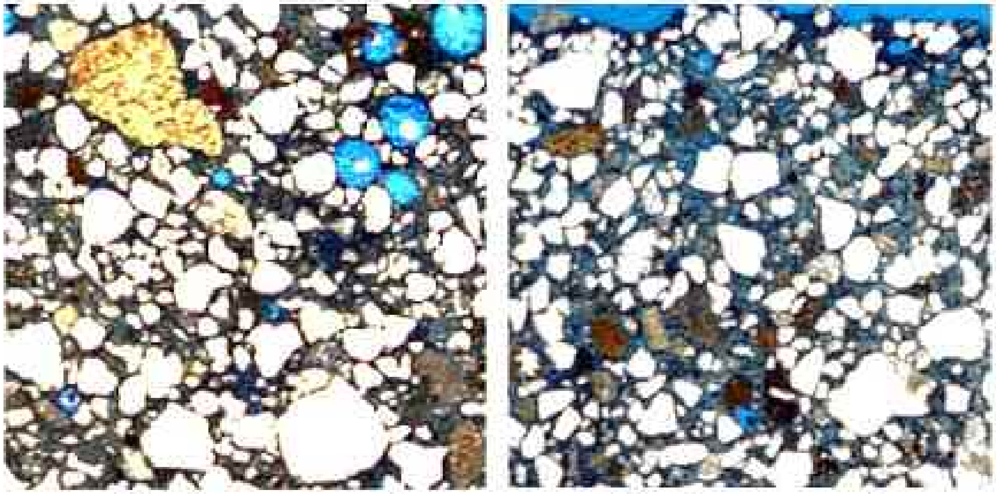

Cylinder 10 3-day Cylinder 7 7-day

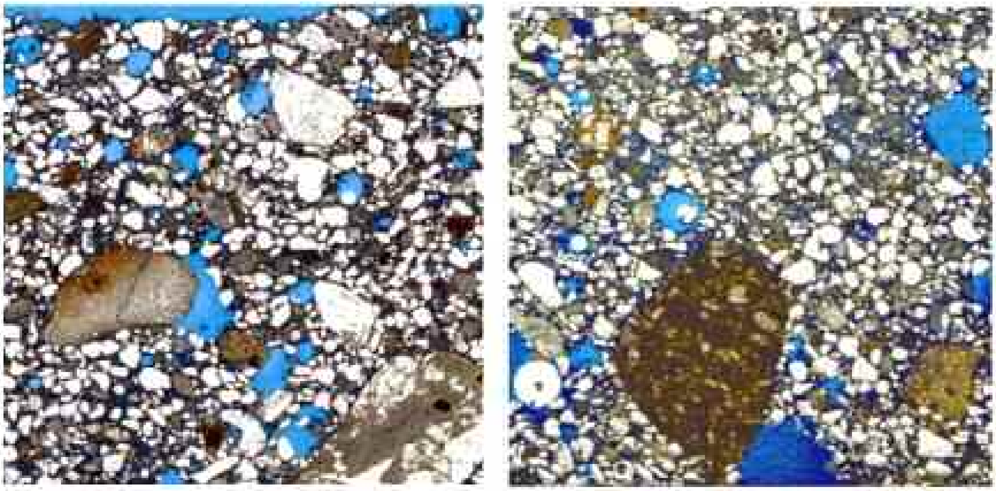

Cylinder 6 14-day Cylinder 4 28-day

Figure 31. Representative material from the 3, 7, 14 and 28 day pours. All samples show a mixed porosity system of (dominantly) <1 mm-scale vugs (blue dye), intra-cement volume, and some grain cracks. [Field of view in each image is 10 mm.]

Elastic Wave Velocities

Penetration into rock and rock-like materials such as concrete is fundamentally a damaging process; damage degrades the elastic moduli, thus lowering the elastic wave speeds. Measurement of the elastic wave speeds as a function of spatial position relative to the explosives or as a function of cure time or loading conditions would be expected to show changes that would correlate with the history of the specimen. When velocities are measured on specimens from different pours, but under identical conditions, differences point to differences in the starting concrete. This is important to know when attempting to correlate changes between cylinders cast from different batches of concrete that are nominally the same. Examined as a function of cure time, elastic wave velocities give information on the temporal evolution of the moduli of the concrete, showing how the curing is progressing. Velocity measurements made on specimens after a known loading history can be compared with specimens from the explosively loaded cylinders, whose loading history is not known. Finally and most importantly for the present work, the spatial variation of wave speeds as a function of distance from the explosive charge can be used to quantify the extent and magnitude of the damage.

Several sets of velocity data were collected including:

- Compressional wave (V_P) and shear wave (V_S) velocities on as-poured specimens from all the pours, as a function of cure time.
- V_P measured on specimens subjected to hydrostatic stress past the point of lock-up, where the tangent bulk modulus increases rapidly.
- V_P for cores taken along a radius of the explosively-loaded cylinders, post-test.

Sample preparation and handling:

Samples from each pour (4-6 per pour; ~8" length) were prepared by rodding the concrete 25 times and then lightly vibrating the container with 10-15 taps on the exterior of a standard 102-mm-diameter (4 inch) concrete testing sleeve. Samples were then capped and stored at ~20 ºC in standard laboratory conditions. After extracting a specimen from its sleeve, velocity measurements were made in two orthogonal directions, perpendicular to the cylindrical specimen's axis (see Figure 32); following the measurements, all samples were put back into their respective container, capped, and stored as above until needed. Specimens used for hydrostatic compression testing were handled similarly prior to testing. Following the hydrostatic tests, these samples were unjacketed and cut in 3 sections, and stored as above. At a later date, Vp measurements were made across the center of the bottom half of the original sample on the same day as the split-core Vp data were collected. In all cases, more than 45 days had elapsed since the specimens were cast.

Specimens were extracted from cylinders C10, C7, C6 and C4 after they were explosively loaded on the 3rd, 7th, 14th and 28th day after casting, respectively. As shown in Figure 32, 51-mm (2") -diameter cores were taken at approximately the mid-height of the tested cylinders. All cores were taken perpendicular to the exterior wall, from material located within 200 mm of the vertical centerline and sampled the tested cylinder all the way to the borehole wall. Cores were split with the cut face oriented in the *r-z* plane to facilitate both velocity measurements and microscopy investigations (see Microstructural imaging). The split cores were bubble-wrapped and stored in the laboratory as above. Since Vp measurements on the hydrostatically-loaded specimens and the explosively-loaded specimens were made between 45 and 60 days after pouring, the water content of these samples was <3% by volume based on the moisture content measurements discussed earlier (see Figure 30).

The source and receiver used were 2.25 MHz shear-polarized transducers powered by a Panametrics signal generator, with signals recorded by a Nicolet 4090 oscilloscope. Molasses was used as a couplant for all measurements. Travel path distances were measured using a standard mechanical caliper, accurate to 0.01 mm. Absolute travel time errors associated with determining the first break of the respective phase picks are ~0.1 μs in 30.0 μs (Vp) and ~0.3 μs in 50 μs (Vs); travel path errors are ~0.2 mm in 100 mm. Table 5 provides the recording and processing parameters used in the reduction of raw waveforms following the standard pulse-transmission technique (Christensen, 1985).

Results:

Tabulations of all Vp and Vs measurements associated with the 102mm-diameter as-poured specimens are in Table 6 and are plotted in Figure 33 for the various pore dates and Figure 34 as a function of cure age. Within the limits set by the error estimates in Table 5 (Vp ± 20 m/s; Vs ± 20 m/s), no evidence of anisotropy in P- or S-wave velocities was observed. The large range of values for Vs measured on C3 and C4 at a 28 day cure age seems to represent an anomaly. Intra-pour variability can be on the order of 2-3% (e.g., C3 and C4), but overall is considered sufficiently low such that the large test cylinders are expected to be effectively homogeneous

Table 5. Velocity measurement parameters

Test	Compressional wave	Shear wave
102 mm (4”)-diam,		
untested	10	100
sample rate (10^{-9} s)	0.6	0.9
error (%)	none	low-pass zero-phase Butterworth,
filtering		100 kHz
102 mm (4”)-diam,		not determined
hydrostatic	5	
sample rate (10^{-9} s)	0.6	
error (%)	none	
filtering		
51 mm (2”)-diam split		not determined
core	5	
sample rate (10^{-9} s)	0.6	
error (%)	none	
filtering		

From Figure 33, inter-pour variability for a given cure time is seen to be on the order of 200 m/s for both Vp and Vs. Over the 3 to 28 day cure time, velocity increases of ~350 m/s (Vp) and

~300 m/s (Vs) were observed. These changes occur over the period during which the majority of the pore volume is dewatered which would tend to increase both Vp and Vs due to the lower density. Shear waves are not much affected by the state of saturation, but higher saturations, approaching 100% do cause V_P to increase. The observed increase in velocities as a function of cure time reflects significant moduli increases, presumably due to increased grain-cement paste bonding and cement paste stiffening.

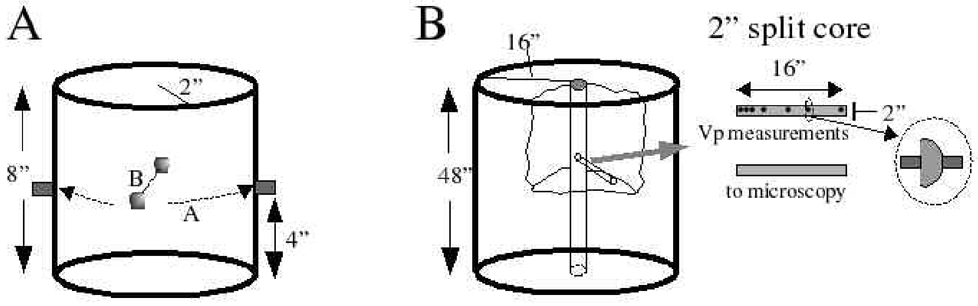

Figure 32. Travel paths for velocity measurements. (a) 102 mm (4 in) diameter specimens from as-poured and hydrostatic tests. (b) 51 mm (2 inch)-diameter radial core retrieved from explosively loaded cylinders.

Figure 35 and Table 7 present the compressional-wave velocities measured on core retrieved from the explosively-loaded cylinders. Measurements were made perpendicular to the axis of the original 51 mm core, which had been split to obtain specimens for thin sections. As a result, the path length was approximately 25 mm. Column two in Table 7 records the position of measurement relative to the inner end of the core, instead of relative to the axis of the test cylinder. The difference is 50.8 mm (2 “). Path length (column 3) varies slightly due unevenness in cutting the core in half lengthwise. Actual travel time (column 4) was recorded but a correction factor of 0.29 microseconds must be subtracted to account for travel time through the transducers. The final two columns contain the results of normalizing V_P with respect to V_P measured on hydrostatically-loaded specimens and as-poured, untested specimens, using data found in Table 8.

A clear reduction in wave speed over the 0-50 mm radial distance is seen for core from all test cylinders, with moduli reduction extending out to ~150 mm. In Figure 35 it is clear that concrete cured for 3 and 7 days exhibited reduced velocities over the entire length of the core, while the concrete cured 14 and 28 days regained the as-poured velocities for the outer portions of the core, which were farther from the explosives. There is a suggestion of lowered velocities in the outer 100 mm. To quantify the extent of the damage incurred by the explosively-loaded cylinders, another set of measurements was made on the hydrostatically-loaded and as-poured 102 mm-diameter cylinders. For comparability these measurements were made at the same time as those made on the retrieved core (Figure 35 and Table 7). Results of these measurements are in the final columns of Table 7. The significance of these results will be discussed in the section Analysis of Experiments.

Table 6. Compressional and shear-wave velocities measured on 102 mm (4")-diameter as-poured cylinders, by pour date and cure time

Cylinder #	**Pour date**	**Cure time** (days)	**Phase** (P/S)	**Velocity** (m/s)
C1/2	15-Jun	3	P	3102
C1/2	15-Jun	3	P	3079
C1/2	15-Jun	3	P	3059
C1/2	15-Jun	3	P	3023
C9	6-Jul	3	P	2863
C9	6-Jul	3	P	3033
C9	6-Jul	3	P	3108
C9	6-Jul	3	P	3117
C10	9-Jul	3	P	3104
C10	9-Jul	3	P	3120
C10	9-Jul	3	P	3083
C10	9-Jul	3	P	3065
C1/2	15-Jun	3	S	2134
C1/2	15-Jun	3	S	2126
C1/2	15-Jun	3	S	2085
C1/2	15-Jun	3	S	2119
C9	6-Jul	3	S	2001
C9	6-Jul	3	S	2056
C9	6-Jul	3	S	2104
C9	6-Jul	3	S	2054
C10	9-Jul	3	S	2177
C10	9-Jul	3	S	2170
C10	9-Jul	3	S	2150
C10	9-Jul	3	S	2147
C1/2	15-Jun	7	P	3190
C1/2	15-Jun	7	P	3128
C1/2	15-Jun	7	P	3152

Table 6. Compressional and shear-wave velocities measured on 102 mm (4")-diameter as-poured cylinders, by pour date and cure time

Cylinder #	**Pour date**	**Cure time** (days)	**Phase** (P/S)	**Velocity** (m/s)
C1/2	15-Jun	7	P	3170
C5/6	29-Jun	7	P	3381
C5/6	29-Jun	7	P	3349
C7	30-Jun	7	P	3078
C7	30-Jun	7	P	3041
C7	30-Jun	7	P	3058
C7	30-Jun	7	P	2996
C8	1-Jul	7	P	3358
C8	1-Jul	7	P	3253
C8	1-Jul	7	P	3359
C8	1-Jul	7	P	3323
C1/2	15-Jun	7	S	2166
C1/2	15-Jun	7	S	2284
C1/2	15-Jun	7	S	2151
C1/2	15-Jun	7	S	2201
C5/6	29-Jun	7	S	2344
C5/6	29-Jun	7	S	2280
C7	30-Jun	7	S	2069
C7	30-Jun	7	S	2100
C7	30-Jun	7	S	2095
C7	30-Jun	7	S	2077
C8	1-Jul	7	S	2309
C8	1-Jul	7	S	2329
C8	1-Jul	7	S	2370
C8	1-Jul	7	S	2327
C1/2	15-Jun	14	P	3235
C1/2	15-Jun	14	P	3252
C1/2	15-Jun	14	P	3230
C1/2	15-Jun	14	P	3190
C3/4	17-Jun	14	P	3394
C3/4	17-Jun	14	P	3421
C3/4	17-Jun	14	P	3352
C3/4	17-Jun	14	P	3355
C5/6	29-Jun	14	P	3469
C5/6	29-Jun	14	P	3484
C1/2	15-Jun	14	S	2208
C1/2	15-Jun	14	S	2200
C1/2	15-Jun	14	S	2155
C1/2	15-Jun	14	S	2168
C3/4	17-Jun	14	S	2362

Table 6. Compressional and shear-wave velocities measured on 102 mm (4")-diameter as-poured cylinders, by pour date and cure time

Cylinder #	Pour date	Cure time (days)	Phase (P/S)	Velocity (m/s)
C3/4	17-Jun	14	S	2330
C3/4	17-Jun	14	S	2275
C3/4	17-Jun	14	S	2236
C5/6	29-Jun	14	S	2333
C5/6	29-Jun	14	S	2376
C1/2	15-Jun	28	P	3329
C1/2	15-Jun	28	P	3353
C1/2	15-Jun	28	P	3302
C1/2	15-Jun	28	P	3317
C3/4	17-Jun	28	P	3440
C3/4	17-Jun	28	P	3499
C3/4	17-Jun	28	P	3455
C3/4	17-Jun	28	P	3493
C1/2	15-Jun	28	S	2288
C1/2	15-Jun	28	S	2375
C1/2	15-Jun	28	S	2292
C1/2	15-Jun	28	S	2322
C3/4	17-Jun	28	S	2447
C3/4	17-Jun	28	S	2330
C3/4	17-Jun	28	S	2306
C3/4	17-Jun	28	S	2328

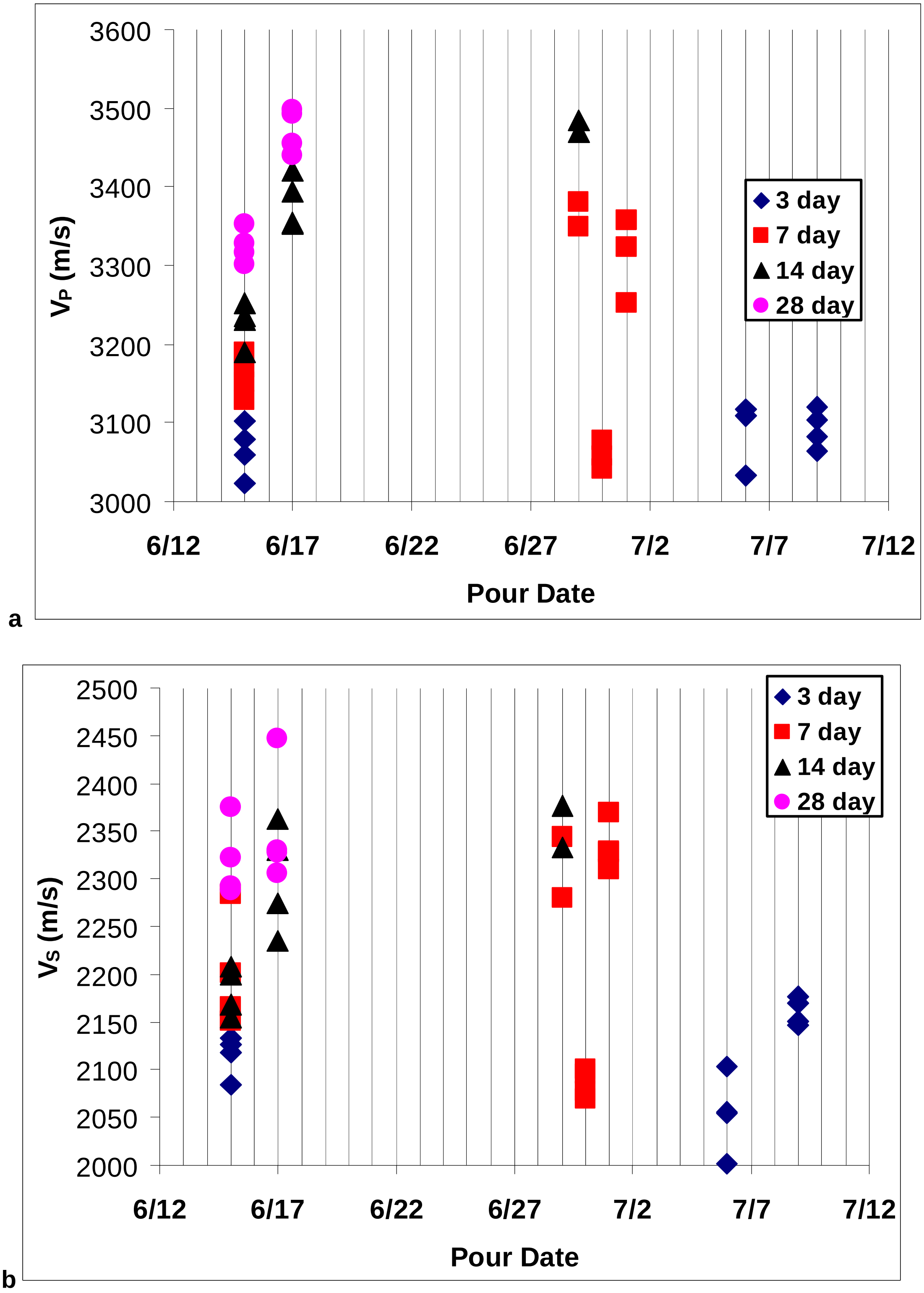

Figure 33. (a) Vp versus pour date (b). Vs versus pour date. Symbols indicate the cure time for each point. Differences in velocity for different pours at the same cure time can be seen by following the same symbol horizontally across the figure

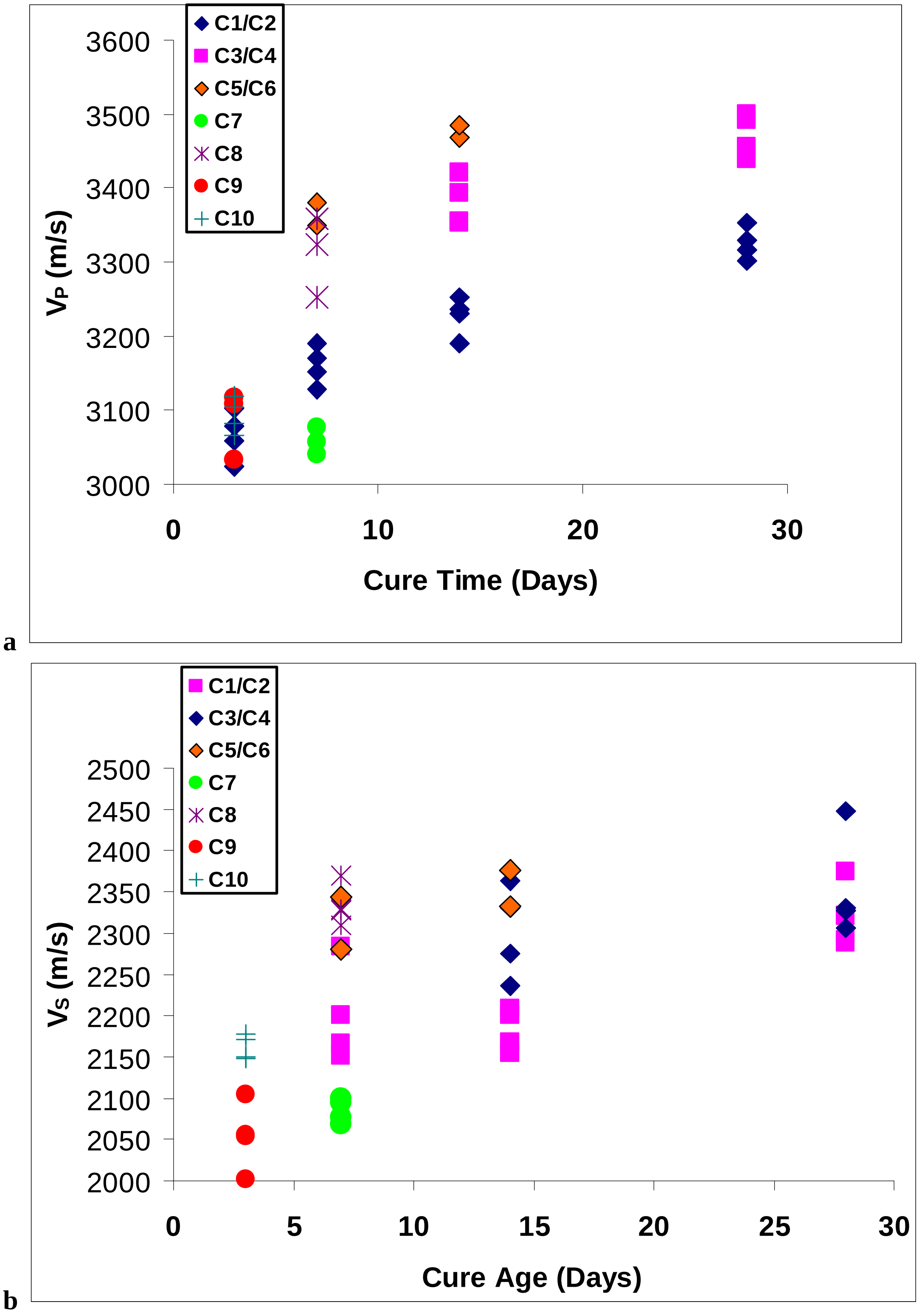

Figure 34. Velocities measured on as-poured specimens for all unique pours as a function of cure time (a) V_P (b) V_S

Table 7. Vp measurements on cores taken post-test from the explosively-loaded cylinders.

Cylinder# -cure age	radial position (mm)	path length (mm)	Travel Time (μs)	Vp (km/s)	normalized to Vp from hydrostatically loaded	normalized to Vp from as-poured
C6 - 14 day	12.7	24.12	13.30	1.854	1.68	0.54
6	35.2	23.62	8.82	2.769	2.52	0.81
6	61.5	23.42	7.35	3.320	3.02	0.97
6	107.6	22.17	6.47	3.590	3.26	1.05
6	274.9	19.15	5.78	3.488	3.17	1.02
6	373.0	22.46	7.57	3.085	2.80	0.90
C7 - 7 day	11.6	22.95	16.34	1.430	0.92	0.45
7	30.5	23.48	12.43	1.935	1.24	0.61
7	58.3	23.66	9.28	2.633	1.69	0.84
7	130.0	25.8	9.12	2.922	1.87	0.93
7	230.0	22.47	8.18	2.850	1.83	0.90
7	295.0	22.2	7.94	2.902	1.86	0.92
7	375.0	22.38	8.50	2.728	1.75	0.87
7	395.0	22.11	9.18	2.488	1.59	0.79
C4 - 28 day	10.5	23.45	10.64	2.266	1.79	0.68
4	29.3	23.8	8.02	3.079	2.43	0.92
4	53.0	23.3	7.71	3.142	2.48	0.94
4	82.0	23.22	7.44	3.248	2.57	0.97
4	193.0	22.96	6.58	3.650	2.89	1.09
4	260.0	22.72	7.00	3.386	2.68	1.01
4	390.0	19.93	5.96	3.518	2.78	1.05
C10 - 3 day	13.7	21.3	8.68	2.539	1.15	0.78
10	33.5	24.36	8.83	2.854	1.30	0.87
10	62.0	24.65	8.49	3.006	1.37	0.92
10	118.0	25.76	9.03	2.947	1.34	0.90
10	186.0	26.71	9.34	2.953	1.34	0.90
10	247.0	27.86	9.01	3.197	1.45	0.98
10	350.0	24.29	7.69	3.285	1.49	1.01

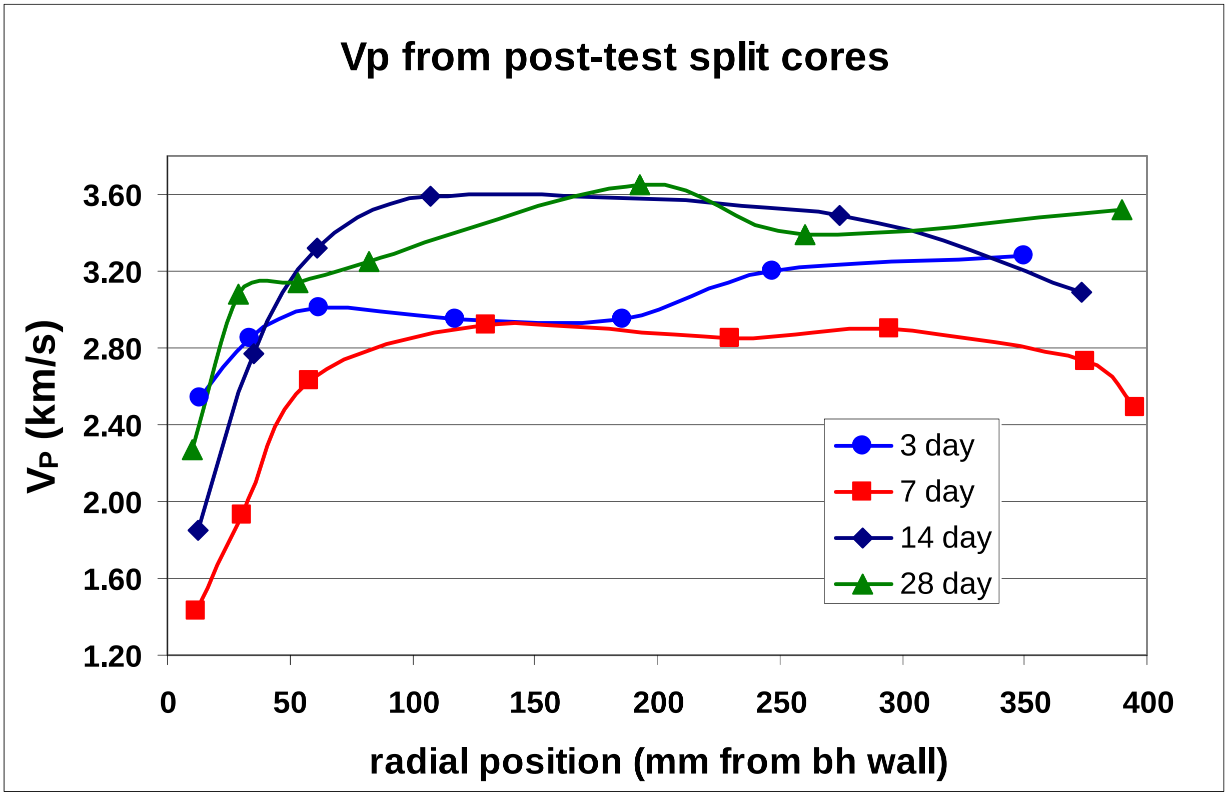

Figure 35. Vp as a function of distance from the borehole wall, measured on specimens cored post-test from cylinders C10, C7, C6 and C4 which were explosively-loaded at 3, 7, 14, and 28 days after pouring.

Table 8. Vp measurements on 102 mm-diameter cylinders, as-poured and after hydrostatic compression. Paths A and B are orthogonal to each other and perpendicular to the axis of the cylinder.

Cylinder#-cure age-Type		**path length (mm)**	**Travel Time** (µs)	**Vp** (km/s)	**Vp (avg)** (km/s)
C3-28-day, Hydrostatic					
	A	99.40	76.24	1.31	**1.26**
	B	99.90	82.10	1.22	
C3-28-day, As-poured					
	A	101.94	30.66	3.36	**3.35**
	B	101.68	30.70	3.34	
C5-14-day,Hydrostat					
	A	98.02	89.28	1.10	**1.10**
	B	97.67	89.12	1.10	
C5-14-day, As-poured					

A	101.98	30.06	3.43	**3.43**
B	101.14	29.72	3.44	
C8-7-day,Hydrostat				
A	99.54	63.46	1.58	**1.56**
B	99.80	64.82	1.55	
C7-7-day-Untested				
A	101.75	32.40	3.17	**3.15**
B	100.90	32.48	3.13	
C10-3-day,Hydrostat				
A	99.37	45.32	2.21	**2.20**
B	99.54	45.68	2.19	
C10-3-day,As-poured				
A	101.35	31.58	3.24	**3.26**
B	101.42	31.12	3.29	

Mechanical Properties:

Hydrostatic compression strains, uniaxial compressive strengths, tensile strengths and strengths under a confining pressure of 50 and 100 MPa were determined for all unique pours. Uniaxial compressive strength was determined by a commercial testing laboratory, using industry standard techniques, applied to cylinders of concrete. These specimens were cast in standard cylindrical molds (102 mm diameter by 200 mm long) at the same time and from the same batch as the large test cylinders. In general these strengths will be somewhat lower than would be observed if the same tests were conducted to ASTM standards with carefully ground and trued ends on the test cylinders. However, the trends and relative magnitudes would be similar. All tests are listed and summarized in Table 9.

Table 9. Summary of mechanical properties tests

Cyl #	Cast Date	Specimen	Test type	Date	age (day)	σ_{11}, Peak (MPa)	σ_{33}, Peak (MPa)	σ_D, Peak (MPa)	ρ (g/cc)
1	6/15/04	C-1-D-UCS	Unconfined	7/13/04	28	8.79	0	8.79	
1	6/15/04	C-1-C-UCS	Unconfined	6/18/04	3	5.39	0	5.39	
1	6/15/04	C-1-B-UCS	Unconfined	6/18/04	3	5.41	0	5.41	
1	6/15/04	C-1-D-UCS	Unconfined	6/22/04	7	6.48	0	6.48	
2	6/15/04	C-2-B-UCS	Unconfined	6/18/04	3	5.51	0	5.51	
2	6/15/04	C-2-C-UCS	Unconfined	6/30/04	15	7.54	0	7.54	
2	6/15/04	CYL2_1	Triaxial	6/28/04	13	170.00	50	120.00	2.01
2	6/15/04	CYL2_2	Triaxial	6/29/04	14	175.00	50	125.00	

Cyl #	Cast Date	Specimen	Test type	Date	age (day)	σ_{11}, Peak (MPa)	σ_{33}, Peak (MPa)	σ_{D}, Peak (MPa)	ρ (g/cc)
2	6/15/04	CYL2_3	Triaxial	6/30/04	15	320.00	100	220.00	2.08
3	6/17/04	C-3-D-UCS	Unconfined	7/15/04	28	12.03	0	12.03	1.96
3	6/17/04	CYL3_1	Triaxial	7/15/04	28	145.00	50	95.00	1.96
3	6/17/04	CYL3_2	Brazilian	7/15/04	28	7.26	-2.42	2.42	1.95
3	6/17/04	CC3-28HC	Hydrostat	7/15/04	28	193.00	193	0.00	2.04
4	6/17/04	CYL4_1	Triaxial	7/15/04	28	205.00	100	105.00	2.01
4	6/17/04	CYL4_2	Brazilian	7/15/04	28	7.23	-2.41	2.41	1.94
5	6/29/04	C-5-D-UCS	Unconfined	7/13/04	14	11.10	0	11.10	1.99
5	6/29/04	C-5/6	Unconfined	7/27/04	28	14.68	0	14.68	1.99
5	6/29/04	CYL5_1	Triaxial	7/13/04	14	130.00	50	80.00	1.99
5	6/29/04	CYL5_2	Triaxial	7/13/04	14	192.00	100	92.00	1.96
5	6/29/04	CYL5_3	Brazilian	7/13/04	14	4.77	-1.59	1.59	1.89
5	6/29/04	CC5-03HC	Hydrostatic	7/2/04	3	219.00	219	0.00	
5	6/29/04	CC5-14HC	Hydrostatic	7/13/04	14	285.00	285	0.00	1.96
7	6/30/04	C-7-C-UCS	Unconfined	7/7/04	7	7.54	0	7.54	1.93
7	6/30/04	CYL7_1	Triaxial	7/7/04	7	165.00	50	115.00	1.93
7	6/30/04	CYL7_2	Triaxial	7/7/04	7	305.00	100	205.00	1.93
7	6/30/04	CYL7_3	Brazilian	7/7/04	7	4.38	-1.46	1.46	1.90
7	6/30/04	CYL7_4	Brazilian	7/7/04	7	4.11	-1.37	1.37	1.90
7	6/30/04	CYL7_5	Brazilian	7/7/04	7	4.41	-1.47	1.47	1.75
7	6/30/04	CC7-07HC	Hydrostatic	7/7/04	7	275.00	275	0.00	
8	7/1/04	C-8	Unconfined	7/29/04	28	14.20	0	14.20	1.97
8	7/1/04	C-8-C-UCS	Unconfined	7/8/04	7	8.35	0	8.35	1.97
8	7/1/04	CYL8_1	Triaxial	7/8/04	7	149.00	50	99.00	1.97
8	7/1/04	CYL8_2	Triaxial	7/8/04	7	210.00	100	110.00	1.93
8	7/1/04	CYL8_3	Brazilian	7/8/04	7	4.41	-1.47	1.47	1.90
8	7/1/04	CYL8_4	Brazilian	7/8/04	7	4.2	-1.4	1.40	1.91
8	7/1/04	CC8-07HC	Hydrostatic	7/8/04	7	94.00	94	0.00	2.03
8	7/1/04	CC8-07H2	Hydrostatic	7/8/04	7	199.00	199	0.00	
9	7/6/04	C-9-C-UCS	Unconfined	7/9/04	3	4.12	0	4.12	1.92
9	7/6/04	CYL9_1	Triaxial	7/9/04	3	165.00	50	115.00	1.92
9	7/6/04	CYL9_2	Triaxial	7/9/04	3	262.00	100	162.00	1.86
9	7/6/04	CYL9_3	Brazilian	7/9/04	3	2.79	-0.93	0.93	1.70
9	7/6/04	CYL9_4	Brazilian	7/9/04	3	2.91	-0.97	0.97	1.74
9	7/6/04	CC9-03HC	Hydrostatic	7/9/04	3	352.00	352	0.00	2.03
10	7/9/04	C-10-C-UCS	Unconfined	7/12/04	3	7.07	0	7.07	1.93
10	7/9/04	C-10	Unconfined	7/27/04	18	11.21	0	11.21	1.93
10	7/9/04	CYL10_1	Triaxial	7/12/04	3	154.00	50	104.00	1.93
10	7/9/04	CYL10_2	Triaxial	7/12/04	3	250.00	100	150.00	1.89
10	7/9/04	CYL10_3	Brazilian	7/12/04	3	4.14	-1.38	1.38	1.81
10	7/9/04	CYL10_4	Brazilian	7/12/04	3	4.17	-1.39	1.39	1.82
10	7/9/04	C10-03HC	Hydrostatic	7/12/04	3	163.00	163	0.00	2.00

Tensile strengths were determined from a Brazilian test which involves loading a disk of concrete along a diameter until failure occurs, typically as the result of a tensile crack propagating parallel to the loading axis, as in Figure 36. A standard formula relates the load at crack propagation to the tensile strength. Specimens for testing were 50-mm-diameter disks cut from subcores of 150 mm diameter cylinders cast as described above. A number of these larger cylinders were cast for use in the laboratory testing program. Similar subcores were used for the triaxial testing.

Figure 36. Post-test photograph of a Brazilian test specimen, showing the tensile crack induced by loading along the axis parallel the crack.

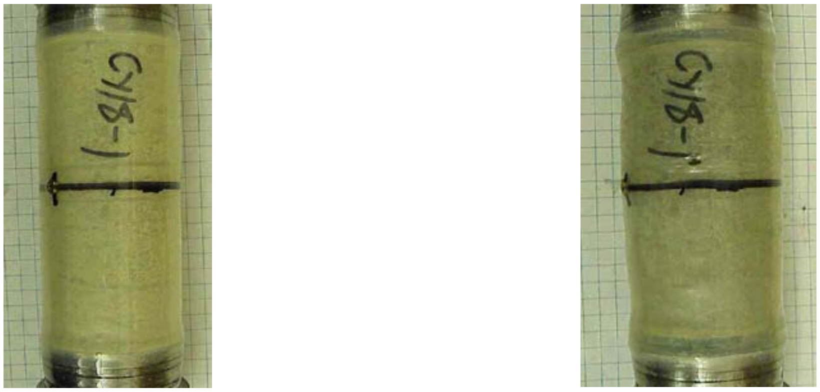

Figure 37. Photographs of triaxial test specimens before (left) and after (right) testing. The black line is to aid in mounting gages. The pattern of deformation is typical: axial shortening with radial bulging and no indication of shearing.

Triaxial tests were conducted with carefully prepared 50-mm-diameter specimens, with a length to diameter ratio of approximately 2.1. Specimen ends were ground flat and parallel to approximately 10 micrometers total runout. Prior to jacketing, surface pits were filled with Ultracal 30 plaster. To exclude the confining pressure medium, a multilayer jacket was used. The first layer was polyethylene shrink tube applied and trimmed to sample length. Pits in the end and edge chips from the grinding were filled with Ultracal. A second layer of shrink tubing was applied over the first tube and end caps. Finally the entire assembly was coated with a UV-cured polyurethane. Pre- and post-test photographs of the jacketed sample may be seen in Figure 37.

Concrete inevitably has large vugs due to trapped air and a heavy and durable jacketing process is required if punch-throughs are to be avoided at higher confining pressures.

All testing was done with a servo-controlled testing machine that applied strain rates of 1 x 10^{-4}/s along the direction of maximum compressive stress, while strains were measured on the specimen using LVDT gages. Testing was typically continued until a clear peak in stress was observed or about 15% axial strain was reached.

Brazilian tests (tensile strength)

Results for all of the tensile strength tests are listed in Table 9 under “Brazilian Tests” and plotted in Figure 38 as a function of cure time for all cylinders except C1 and C2. A clear increase in strength as a function of time was observed, beginning at about -1 MPa (tension is negative) and reaching -2.4 MPa by 28 days. Inter-pour consistency was good for C7 and C8, but C9 and C10 showed a significant difference in strength. The strength trend was nearly linear at 0.06 MPa/day.

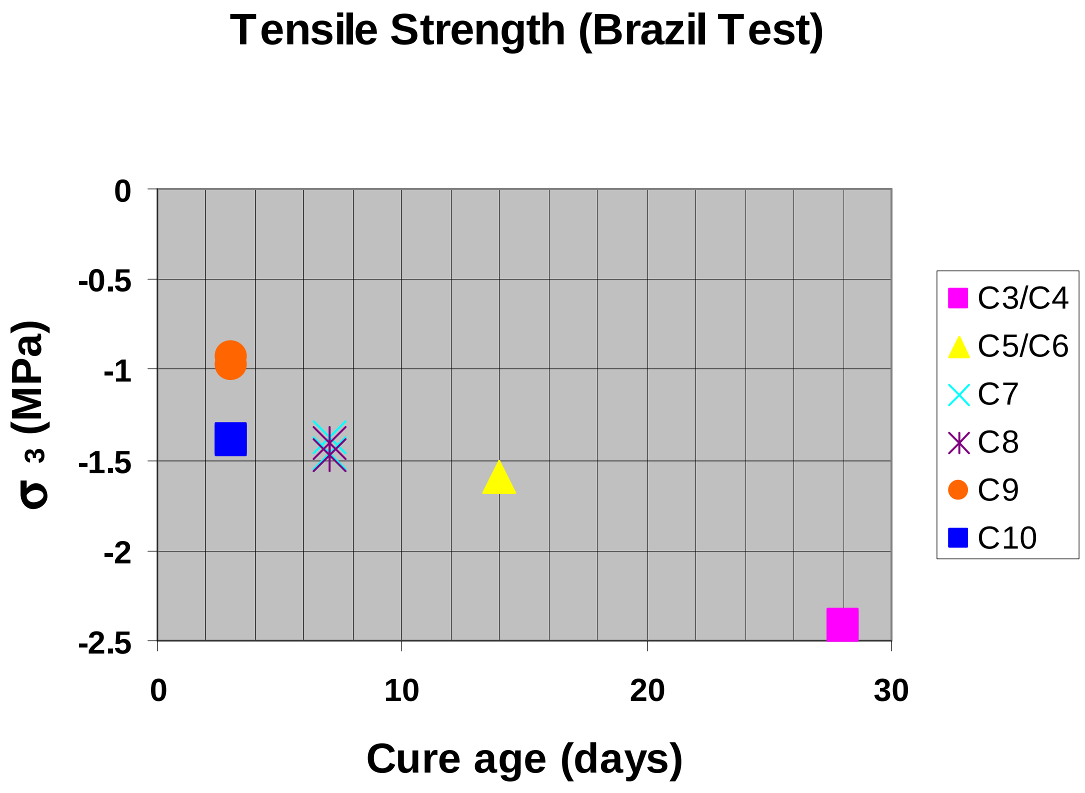

Figure 38. Tensile strength from Brazilian tests as a function of cure age.

Unconfined Compressive Strength (UCS)

The values reported for UCS were obtained by a commercial concrete testing firm using standard methods to test 102-mm (4 inch) -diameter cylinders cast from each pour. Because of the importance of UCS in penetration modeling, a number of tests were done at each cure stage for various cylinders. The results in Figure 39 show increasing strength with cure age and good consistency between pours, except for C1 and C2, the developmental specimens. Up to 7 days, strengths for C1 and C2 are inline with results for the others, but then fell below and were significantly lower by 28 days. Strength was about 14 MPa after 28 days, which is considerably below the 22 MPa reported by Warren, et al. (2004). However their specimens had cured considerably longer. Extrapolating the trend in Figure 39, it is reasonable to expect that by 60 days sstrength of the concrete we used would have been close to the strength of the concrete tested by Warren, et al. (2004).

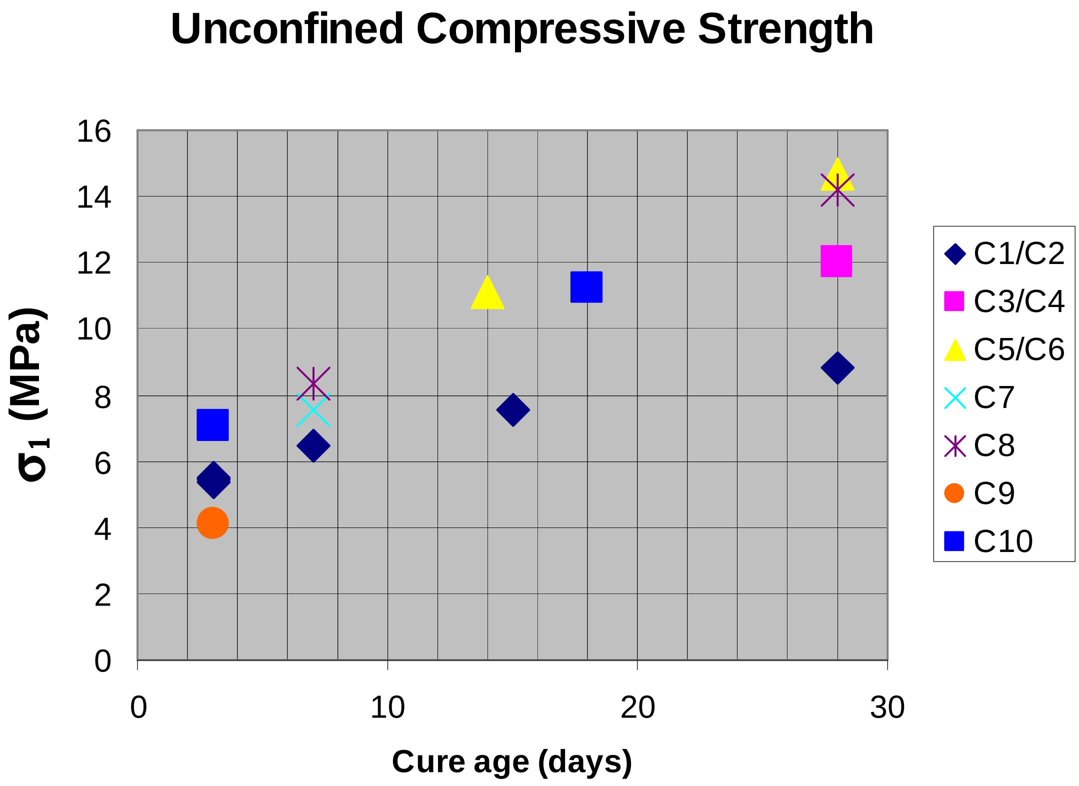

Figure 39. Unconfined compressive strength as a function of cure age for all cylinders.

Triaxial and Hydrostatic Loading

On the same day as the explosive loading test, four tests were carried out on specimens prepared from the same pour as the test cylinder: hydrostatic loading to lock-up, UCS and triaxial tests at 50 and at 100 MPa confining pressure. The goal was to determine material properties that were representative of the properties of the test cylinder at the same cure stage. In Figure 40, the stress difference $\sigma_D = \sigma_1 - \sigma_3$ is plotted as a function of the confining pressure σ_3. Values from the UCS and the tensile strengths from Brazilian tests are also plotted. When the entire data set is viewed as one, it is not clear what, if any relationship there is between strength and confining pressure. Separating the results by cure age on test day clarifies the cause of the variability. Figure 41 consists of four plots which are identical to Figure 40, but only the results from specimens cured for 3, 7, 14 and 28 days, respectively are shown on each plot. Figure 41a shows that specimens from both 3 day cylinders, C9 and C10, poured on different days, exhibit an increase in peak stress difference, reaching 150 MPa at a confining pressure of 100 MPa. Results for the two cylinders are nearly identical. A different response was observed for cylinders C7 and C8, tested at 7 days and poured on different days (Figure 41b). Strength of specimens from the C7 pour increased with pressure, similar to C9 and C10, but the strength of specimens from the C8 pour was the same at 50 MPa and 100 MPa. A nearly identical pattern of results was found for the 14 day cylinders, C1/C2 and C5/C6. Strength of the specimens from the C1/C2 pour exceeded 220 MPa at a confining pressure of 100 MPa., while strength of the C5/C6 specimens increased only slightly between 50 and 100 MPa confining pressure. Only one set of tests was done on specimens representing the 28 day cylinders as they were from the same pour. No sensitivity to pressure was observed above 50 MPa confining pressure.

The most likely explanation for the insensitivity to confining pressure is water. As discussed earlier, the moisture content of specimens could be quite high, approaching saturation in the early stages of curing. As the pressure compresses the specimens, removing void space, there may come a point where saturation is reached. Higher pressures then have no effect as the effective pressure remains fixed at the pressure required to produce saturation. Until saturation is induced, the effect of pressure is as expected; σ_D increases steadily as σ_3 increases.

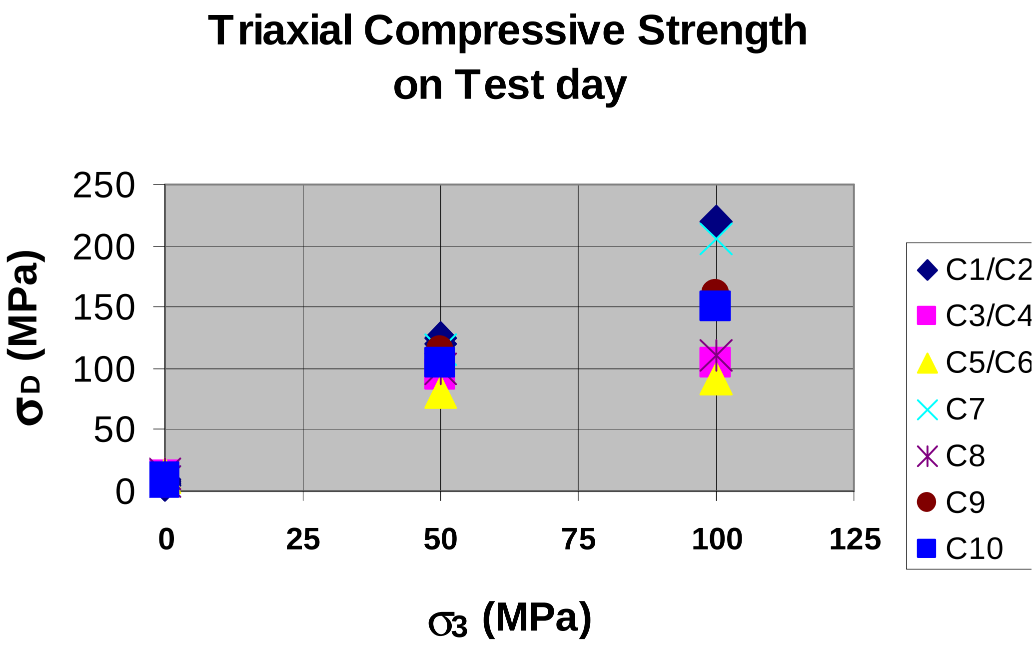

Figure 40. Peak differential stress $\sigma_D = \sigma_1 - \sigma_3$ as a function of confining pressure σ_3 for specimens tested at the same cure age as the cure age of the corresponding explosively loaded cylinders.

The effect of curing on strength is obscured by the pore pressure effect. However if the strengths are plotted separately as a function of cure time for $\sigma_3 = 50$ and 100 MPa, the effects of pore pressure and cure time can be separated. Uniaxial compressive strength (Figure 39) showed a clear dependence on cure time, which is not surprising because in the absence of a jacket to confine internal moisture, there can be no pore pressure, assuming loading is slower than the liquid diffusion time. For the tests with confining pressure this is not the case. Figure 42 separates the data set into tests at (a) 50 MPa and (b) 100 MPa. As the samples cure, there is a splitting of each data set, with some tests showing no effect of aging and a constant peak differential stress and the others, at the same pressure showing an increasing strength. At 50 MPa (Figure 42a) the effect is small but visible. At 100 MPa (Figure 42b), there is a clear split between pressure insensitive, constant strength specimens and specimens with strength increasing as a function of time.

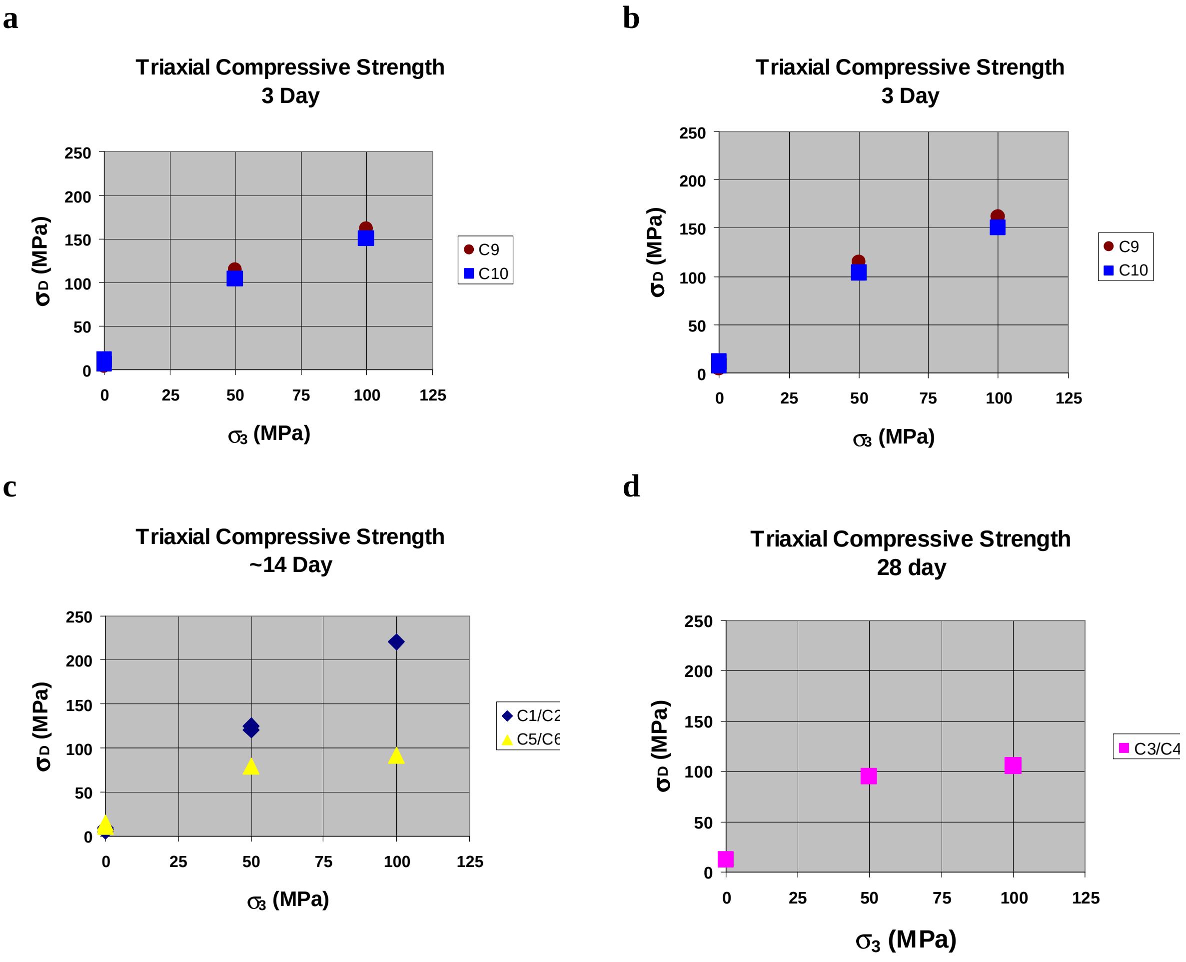

Figure 41. Peak differential stress $\sigma_D = \sigma_1 - \sigma_3$ as a function of confining pressure for all specimens, plotted separately for each cure age, shows two distinct forms of response: (a) pressure-sensitive, (d) pressure-insensitive, and in (b) and (c) a mixed response, depending on the pour.

Strain measurements were made on each of the hydrostatic and triaxial tests, with the exception of the tests on unconfined specimens. Results are presented in a series of three-panel figures (Figure 43 to Figure 45) showing (a) volume strain ε_{kk} versus mean stress $\sigma_m = (\sigma_{11} + 2\sigma_{33})/3$ (b) strains parallel (ε_{11}) and perpendicular (ε_{33}) to the maximum compressive stress σ_{11} and (c) ε_{11} and ε_{33} versus the stress difference $\sigma_D = \sigma_{11} - \sigma_{33}$. Results for the three tests used to characterize each pour are plotted on the same axes. In all three panels, the red curves are from the 100 MPa test and the black lines are from the 50 MPa test. Compression is positive so the curves going to the right in panels (b) and (c) represent ε_{11} and the others are for ε_{33}. In many of the tests, unload cycles, which appear

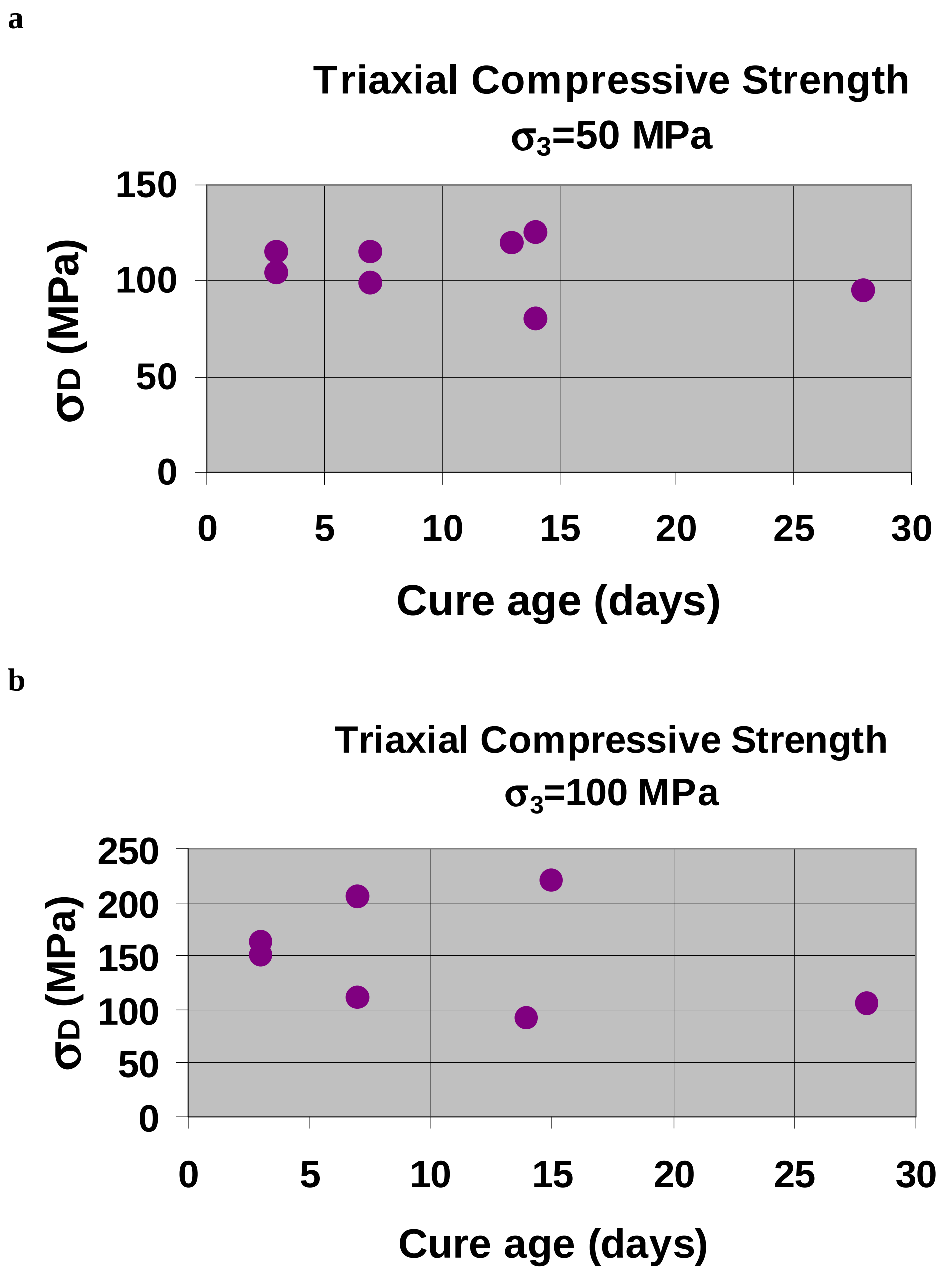

Figure 42. Peak differential stress σ_D as a function of cure age for confining pressure (a) σ_3 = 50 MPa and (b) 100 MPa.

as short vertical lines, were done to allow determination of the elastic moduli. Panel (a) is slightly different as, in addition to the triaxial test results, it also shows the volume strain from the hydrostatic test. As before the red and black lines correspond to the 100 and 50 MPa tests, respectively. Initially the volume strains are positive, indicating compression, but eventually as σ_{11} increases, the sense of volume strain reverses and the specimens dilate. The complete load-unload curves are shown, which makes the plots complex. To clarify the various unload curves, the hydrostatic unloading portion of the two triaxial tests is shown as a dotted line. A third curve, in blue, represents the volume strain from the pure hydrostatic tests, where ε_{kk} is always in compression and positive.

A detailed discussion of one data set will convey the main points concerning the types of behavior exhibited by specimens under hydrostatic and triaxial loading. All observed phenomena may be seen in the results for Cylinders 7 and 8, from separate pours, but tested at the same cure age, 7 days. In the (a) panels of Figure 45 volume strain measured during the hydrostatic test is initially small until a threshold of about 5 MPa is exceeded; then, ε_{kk} increases rapidly as porosity is reduced by the increasing pressure. For Cylinder 7, compaction ceased abruptly at ε_{kk} = 0.03 as the specimen stiffness increased suddenly. Increased stiffness is attrributed to the presence of sufficient water in the pores to cause saturation when the sample volume was reduced by 0.03. All cylinders had a dry porosity of about 20% so the stiffening cannot be due to removing all porosity. A somewhat different behavior was observed for Cylinder 8 (Figure 45a2). Compaction continued for about twice as much strain, before the specimen stiffened at ε_{kk} = 0.06. A second test, using a different specimen from Cylinder 8 was run and showed almost identical behavior, although the second test was not continued beyond 70 MPa. The unloading behavior was linear, indicating that the porosity reduction during loading was permanent, with little recovery. The associated damage is responsible for the reduced velocities measured on the specimens post-test.

ε_{kk} measured in the triaxial tests followed the hydrostat up to the point where the specimen stiffened under hydrostatic loading. For both cylinders and all 6 tests, the plots of σ_m vs- ε_{kk} are virtually identical up to the stress where stiffening occurred in the hydrostatic tests, indicating that the material properties are similar. The difference in stress required to reach stiffening or lock-up are believed to be due to differing amounts of water in the specimens. Just prior to peak stress, the deformation mode changed abruptly from compaction to dilatation. Most of the samples had no obvious failure feature. During unloading, little of the volume strain was recovered, indicating permanent damage.

Figure 45b1 and b2 plots the strains corresponding to the volumetric strains in the (a) panels, as a function of the maximum compressive stress σ_1. Only volumetric strain was measured during the hydrostatic tests, so no results from those tests are included in the (b) and (c) panels. Strains measured during the hydrostatic portion of these tests were identical between specimens and $\varepsilon_{11} = \varepsilon_{33}$, which indicates that the concrete was isotropic. During unloading there was almost no recovery of strain and the behavior was fairly linear, implying that the compacted, damaged concrete behavior is elastic, or nearly so.

The final set of plots, Figure 45c1 and c2, are the same as Figure 45b1 and b2, with the hydrostatic portion of the test removed. Strains have been shifted to start at zero at the beginning of shear loading to allow comparison of the strains. Cylinder 7 specimens were pressure sensitive as can be seen by the large difference in peak stress difference, while Cylinder 8 was not. Note that the scales on the vertical axes are not the same.

Other tests were variations on this theme. Details are summarized in
Table 9. Variations in the lockup stress, where the specimen stiffens under hydrostatic loading, point to a problem of moisture control. Specimens were stored under identical conditions, but it is clear that some unknown factor was responsible for large variations in moisture content.

a

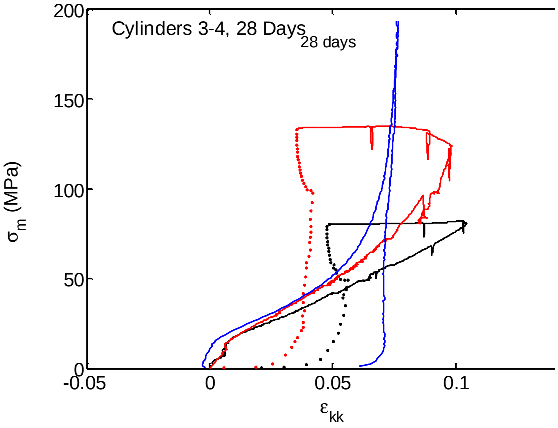
Cylinders 3-4, 28 Days
28 days
σ_m (MPa)
200
150
100
50
0
-0.05
0
0.05
0.1
ε_{kk}

b

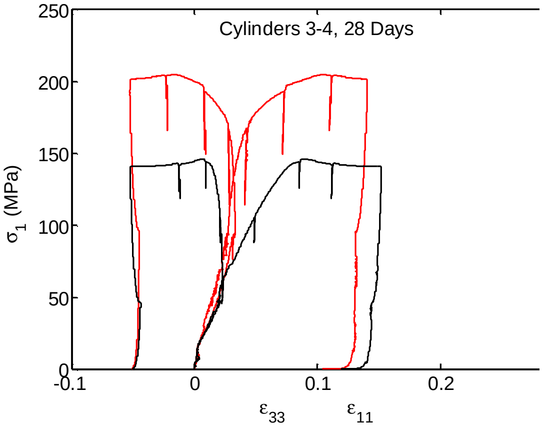
Cylinders 3-4, 28 Days
σ_1 (MPa)
250
200
150
100
50
0
-0.1
0
0.1
0.2
ε_{33}
ε_{11}

c

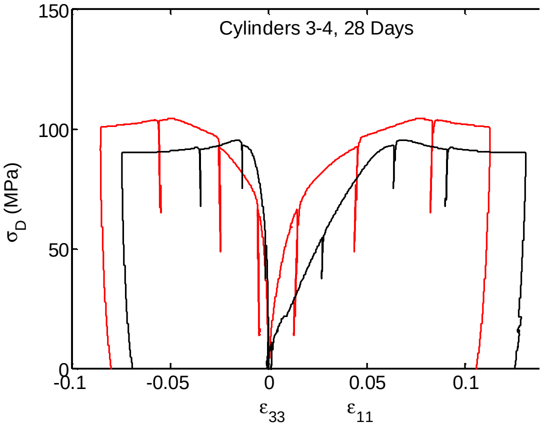
Cylinders 3-4, 28 Days
σ_D (MPa)
150
100
50
0
-0.1
-0.05
0
0.05
0.1
ε_{33}
ε_{11}

Figure 43. Strains measured on specimens from Cylinders 3 and 4 at 28 days. (a) Mean stress-vs-volumetric strain for hydrostatic and triaxial tests, (b) axial stress-vs-axial and lateral strains for triaxial tests, (c) stress difference-vs-axial and lateral strains. Black and red curves represent the 50 and 100 MPa triaxial tests in all panels, while the blue curve in (a) represents the hydrostatic test.

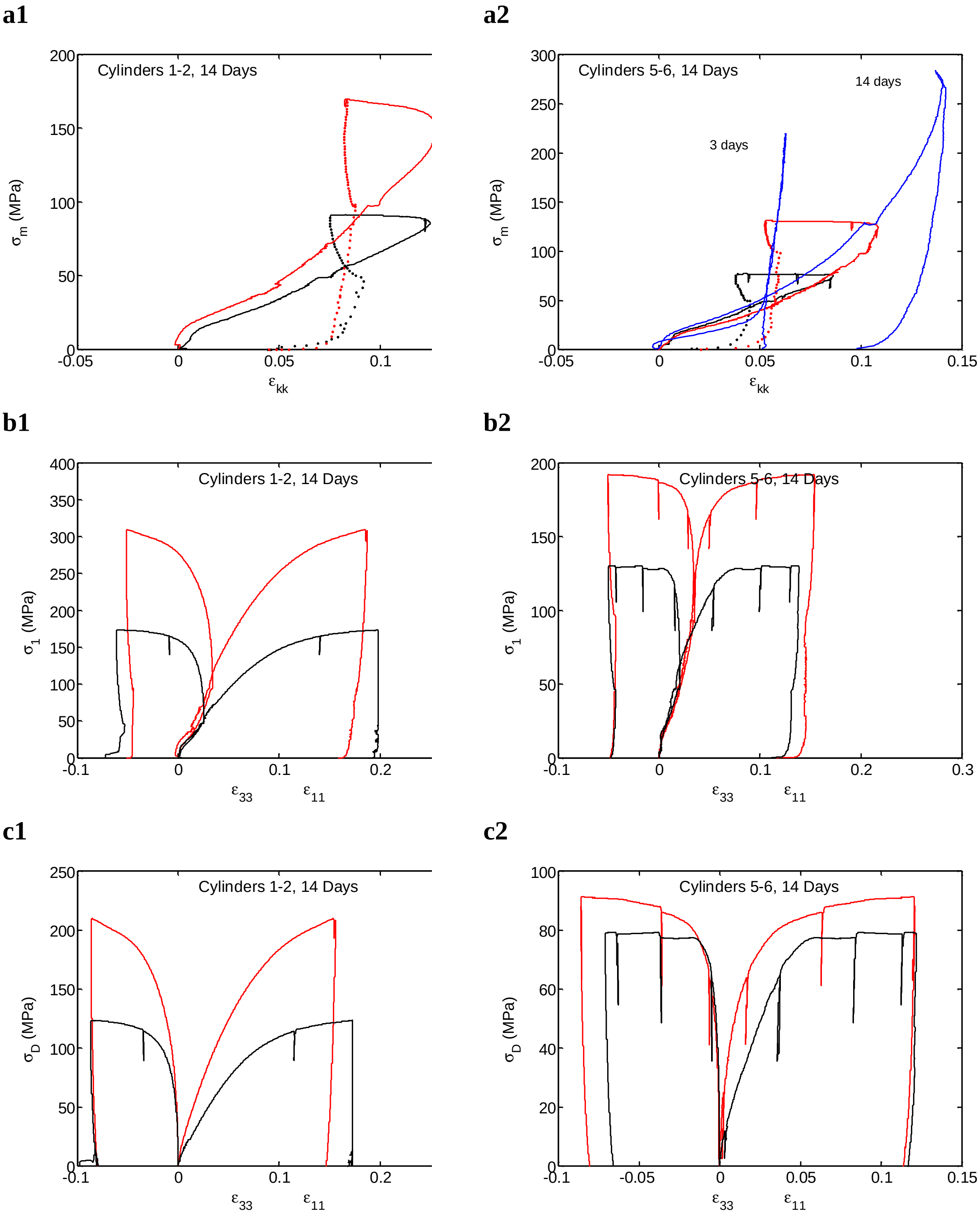

Figure 44. Strains measured on specimens from Cylinders 1, 2, 5 and 6 at 14 days. (a) Mean stress-vs-volumetric strain for hydrostatic and triaxial tests, (b) axial stress-vs-axial and lateral strains for triaxial tests, (c) stress difference-vs-axial and lateral strains. Black and red curves represent the 50 and 100 MPa triaxial tests in all panels, while the blue curve in (a) represents the hydrostatic test.

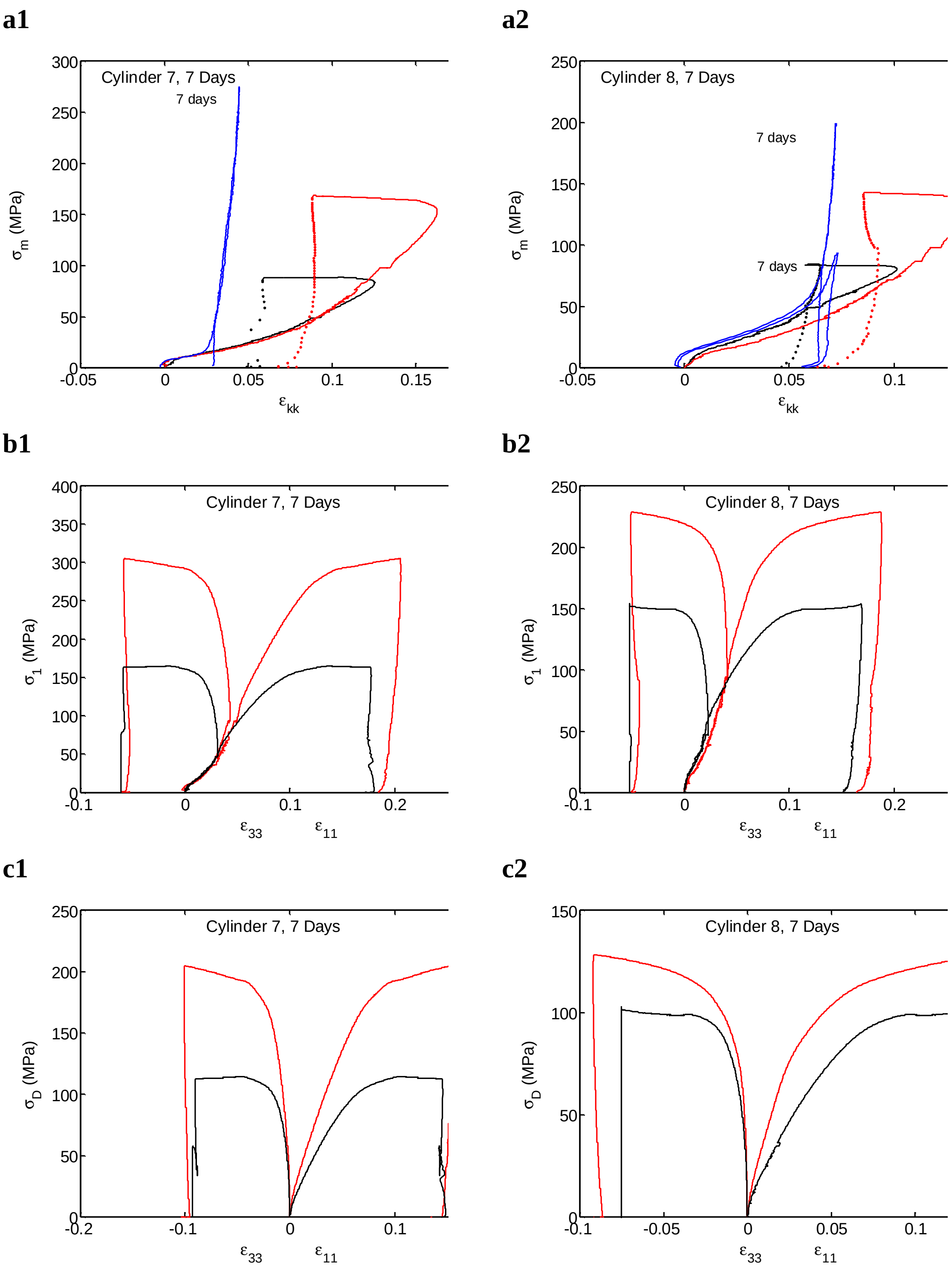

Figure 45. Strains measured on specimens from Cylinders 7 and 8 at 7 days. (a) Mean stress-vs-volumetric strain for hydrostatic and triaxial tests, (b) axial stress-vs-axial and lateral strains for triaxial tests, (c) stress difference-vs-axial and lateral strains. Black and red curves represent the 50 and 100 MPa triaxial tests in all panels, while the blue curve in (a) represents the hydrostatic test.

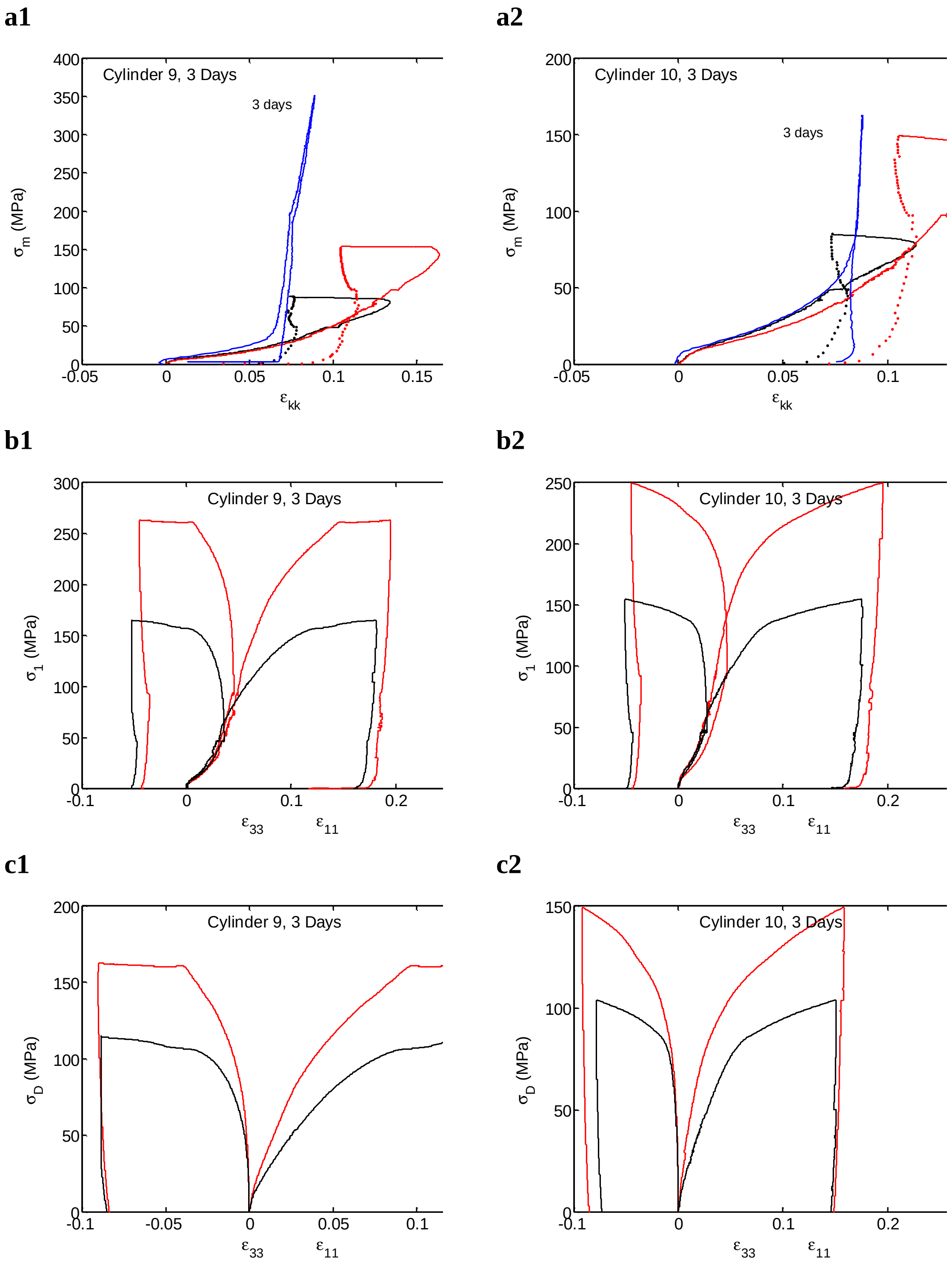

Figure 46. Strains measured on specimens from Cylinders 9 and 10 at 3 days. (a) Mean stress-vs-volumetric strain for hydrostatic and triaxial tests, (b) axial stress-vs-axial and lateral strains for triaxial tests, (c) stress difference-vs-axial and lateral strains. Black and red curves represent the 50 and 100 MPa triaxial tests in all panels, while the blue curve in (a) represents the hydrostatic test.

Microstructural imaging

Introduction:

Microstructural investigations were undertaken on three effective states of each of the unique concrete cylinder pours. Details of the cement paste (CAH) cohesion evolution, CAH-grain bonding, and potential inelastic strain effects can be studied by analysis of these states:

- untested – provides undeformed basic structural model
- hydrostatic compression – provides structural response to quasi-static compression (~200 MPa); expected maximum in grain-grain crushing and other inelastic deformation mechanisms
- explosive tested – high strain rate response to (dominantly) compressive stress wave experienced during ~300 microseconds post-explosion, before the cylinder is destroyed under dominantly tensile stress from reflected energy off top and side boundaries

A combination of surface topographic (optical binocular, scanning electron microscopy [SEM/secondary electron (SE)]) and thin section (transmitted light, SEM/backscatter scanning electron (BSE)) imaging was used to identify the effects described above. Due to time limitations, the analysis is restricted to qualitative description and interpretation.

Sample preparation and handling:

The untested and hydrostatic-tested microscopy samples were obtained from 4”-diameter cylinders (4-6 per pour; ~8” length) which were poured, rodded (25 times), lightly vibrated (10-15 taps on the exterior of the container) in standard concrete testing sleeves, capped, and then stored at ~20 ºC in standard laboratory conditions. Following the completion of all hydrostatic compression experiments (after 3, 7, 14 and 28 days curing) which were performed on trued 4”x8” cylinders), a central ~0.75”-thick disc from both the untested cylinders and their hydrostatic equivalents was extracted; one quarter of this disc was then wrapped for shipping to a petrographic service company to have ultra-thin, fine-polished thin sections prepared. A small chip was chiselled off the center region of the remaining disc to be used in binocular and SEM/SE investigations. The remaining material from each disc was wrapped and stored for possible further use.

Cores were obtained from a representative test cylinders C10, C7, C6 and C4, which had cured 3, 7, 14 and 28 days respectively (see Figure 32). The cores were split so that the cut face would be oriented in the *r-z* plane, to facilitate both velocity measurements and microstructural visualization as a function of radial distance from the explosive source. One of the two split-cores was bubble-wrapped and shipped to the petrographic service company for thin section preparation.

Methods:

- Optical microscopy

  Two perpendicular ultra-thin, fine-polished (<1 mm) thin sections were cut from each of the unique quarter-discs from the untested/hydrostatic material pairs. Orientation of the sections was in the r-z (R notation used in Table 10) and r-θ (P notation) planes with respect to the cylindrical coordinate system of the samples. Blue dye was used to impregnate the concrete billets to enhance identification of porosity and microcrack/grain deformation.

  Each 2”-diameter split core was radially assayed (thin sections cut in the r-z plane) along its entire length (9-11 sections), with each section covering approximately 1.5”(r) X 0.75”(z) in area. The two inner-most sections (denoted C#-A,B below) were cut ultra-thin and fine-polished as with the untested/hydrostatic samples described above; the remainder are standard thin sections.

- SEM

  SEM/SE mounts were prepared using small chips which were mounted on thin circular 1” metal plates and carbon-coated following standard procedures. Samples from all untested, hydrostatic, and test cylinder concrete were made. These mounts could be used for both SE and binocular study to address deformation signatures at multiple scales.

  SEM/BSE samples could be prepared using any of the ultra-thin, polished sections simply by the deposition of a carbon coat as with the SE mounts. Only the 3-day and 28-day inner thin sections were prepared (C10-A, C4-A, respectively).

Results:

Table 10 lists the microscopy samples used in the analysis that follows, and demonstrates the comprehensive microstructural imaging coverage of the three states as described above. Figure 47 depicts a 1-cm^2 area of the 3-day and 28-day-cure materials from each state (untested, hydrostatic, explosively loaded). No significant macroscopic differences can be observed in terms of grain size distribution, vug size and distribution, or localized strain indicators both between material states and between respective concrete batches (note that porosity differences of ~3% [volume] were measured). The images all show a consistent effective medium—that is, a three-component grain-Calcium-Aluminum-Hydrox (CAH) paste-vug material, further illustrated in Figure 48 which displays a representative 1 mm-scale view of the 28-day cure concrete (C3/4). The blue-dye content of each image (excepting any obvious vugs) essentially represents the volume “lost” to the inelastic strain for a particular test (hydrostatic, explosive-generated compressive shock wave). Three products of this strain are separately labelled:

D – deformed CAH paste (intra-cement porosity loss)
R – grain-CAH parting or dislocation surface (termed herein as a '***R***ind')
F – CAH or CAH-grain dislocation that clearly demonstrates strain localization through the matrix and along or through at least one grain

Note also that intra-grain microcracks are common, both in single grains and lithic fragments that make up the sand-sized component of the concrete. This observation necessitates the **F** definition above. In this analysis, only grain cracks clearly associated with matrix deformation will be defined as test-produced 'fractures'. The distinction is clarified by the two examples shown in Figure 48; the results of hydrostatic compression produce both R and F features, with the fractures resolving generally around the grains but clear links to deformation within the matrix (M) itself.

SEM/SE images provide a three-dimensional view of the microstructural components and deformational accommodation seen in the concrete medium. Figure 49A depicts a typical grain-cement paste view, showing both the nature of the surface-coating bonds that develop and the weathered surface of the sand component of the concrete mix. A close-up of the cement phase (Figure 49B) shows the amorphous mineral composition and intra-CAH porosity; in this study, no attempt was made to further analyze the additional complications associated with the effect of cure-time on both the structure and phase composition of the paste. A general depiction of the deformation associated with the explosively-driven compression wave is shown in Figure 49C, where both the F and R elements interact within a vug-CAH paste-grain domain. Figure 50 and Figure 51 catalog the deformation and microstructural interactions due to the hydrostatic- and explosive-testing, respectively, for the cure-time end members of the study (3- and 28-day cure). The most striking result gathered from these figures, and those derived from thin sections, is the consistency in modes of deformation accommodation. The grain 'rind' (R) features that are identified by blue-dye in the thin sections are clearly associated with volume lost (i.e., intra-CAH porosity loss) during the dominantly compressional stress regimes of the hydrostatic and explosively-driven tests; small deviatoric shear stresses occur, localized in space, resulting in F elements both within the matrix and possibly, under relatively rare conditions, acting through grain-tip or -edge discrete cracks.

An important observation is the lack of a clear gradient of deformation-induced damage that correlates with distance from the explosive source. Compressional wave velocities show a 50 to 75 mm-thick highly damaged zone in material recovered from around the central hole of the explosively-loaded cylinders (Figure 35). Study of the 3/7/14/28-day cure thin-sections did not reveal substantially more grain fracturing or CAH matrix deformation near the inner wall. This result may be due to subtle features being missed by the relatively unsophisticated image analysis. However, there is certainly no obvious gradient of damage visible in the microscopic observations, in contrast to the damage gradient that was observed using elastic wave velocities.

Discussion:

Strain accommodation in the explosively-loaded concrete is similar to that seen in the hydrostatically-tested samples for all cure ages. This is a critical point as it relates to the ability to parametrize constitutive models using the results from quasi-static mechanical tests. Also, even with the limits of this analysis, the deformation observed in thin section/SEM images is at least qualitatively greater for the quasi-static hydrostatic compression stress regime than for the explosion-generated compressional wave. As will be discussed in more detail in the Analysis section, this observation is consistent with the finding that compressional wave velocities measured through material within 10 mm of the wall of the central borehole are greater than or equal to Vp measured through hydrostatically-loaded samples.

The rare occurrence of through-grain fracturing highlights the mechanical role played by the cement paste. The most plausible micromechanical model of the concrete must have the grains/lithic fragment component embedded in the porous, variably saturated, low moduli CAH matrix; this matrix then predominantly both transmits, and inelastically responds to, the time-varying stress field.

Table 10. Inventory of microscopy samples

Sample type/sample		**SEM/SE**	**thin sections**	**Notes**
untested	(cure time)			
C3	28-day	C3-U	C3-U-R, C3-U-P	
C5	14-day	C5-U	C5-U-R, C5-U-P	
C8	7-day	C8-U	C8-U-R, C8-U-P	
C10	3-day	C10-U	C10-U-R, C10-U-P	
hydrostatic				
C3	28-day	C3-H	C3-H-R, C3-H-P	
C5	14-day	C5-H	C5-H-R, C5-H-P	
C8	7-day	C8-H	C8-H-R, C8-H-P	
C10	3-day	C10-H	C10-H-R, C10-H-P	
test split core				
C4	28-day	C4-T	C4-T-{A-K}	radial log: 15”
C6	14-day	C6-T	C6-T-{A-L}	radial log: 16”
C7	7-day	C7-T	C7-T-{A-L}	radial log: 16”
C10	3-day	C10-T	C10-T-{A-L}	radial log: 16”

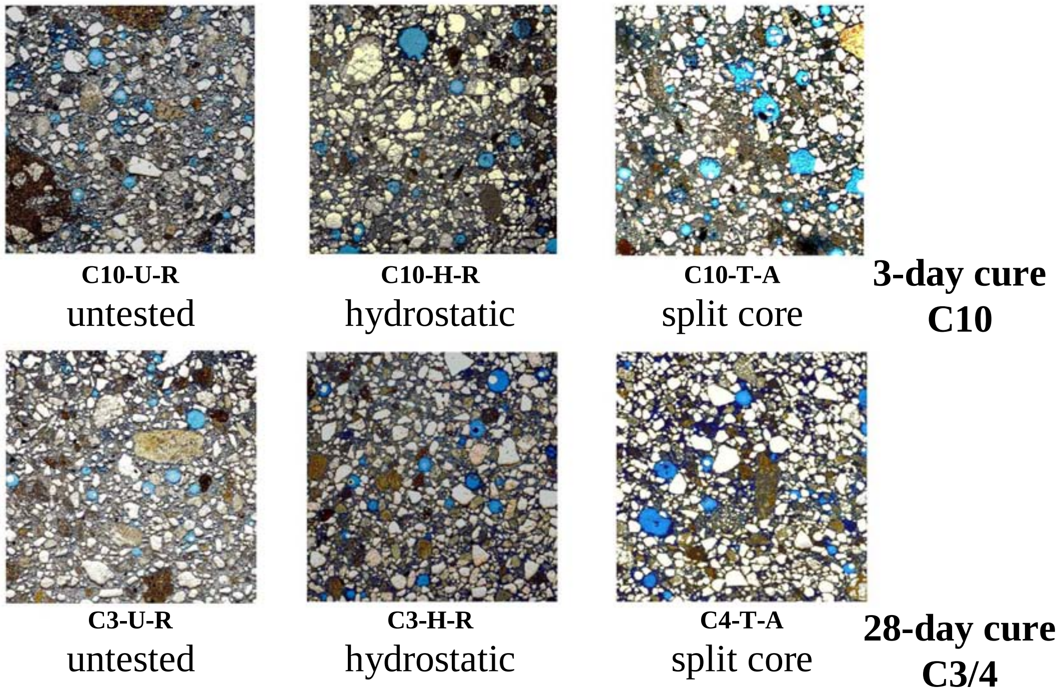

Figure 47. Mesoscopic view of cement microstructure for 3- and 28-day cured concrete. Views of untested, hydrostatically-loaded , and explosively-loaded material are shown. Note similarities in grain size distribution, vug size distribution, and lack of any macroscopic deformation. [Field of view: 10 mm]

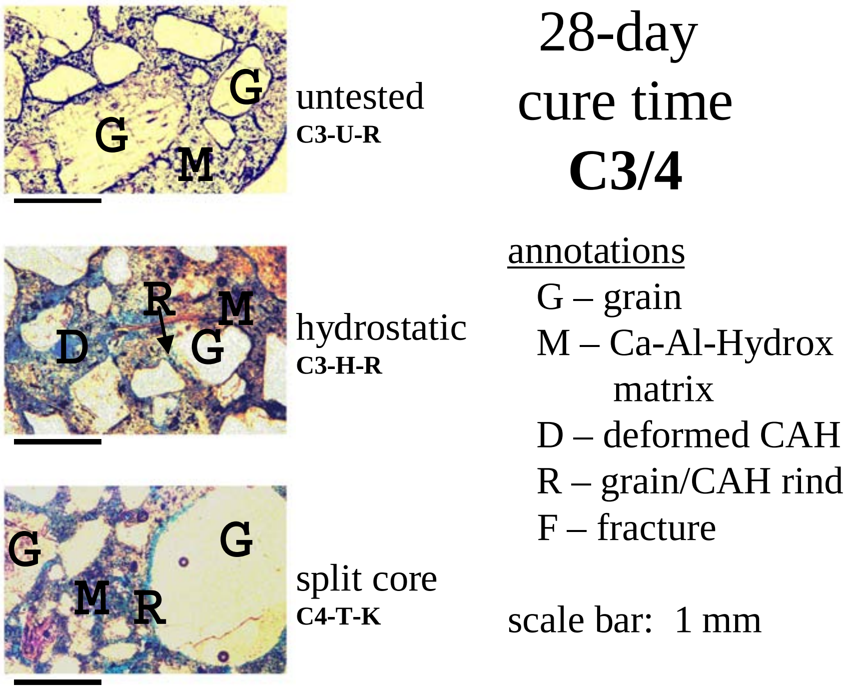

Figure 48. Thin section (plane light) comparison of 28-day (C3/4) concrete samples. Nomenclature used in discussion is defined. Blue dye identifies open or pore-space. The strain accommodation mechanisms are D, R, and F.

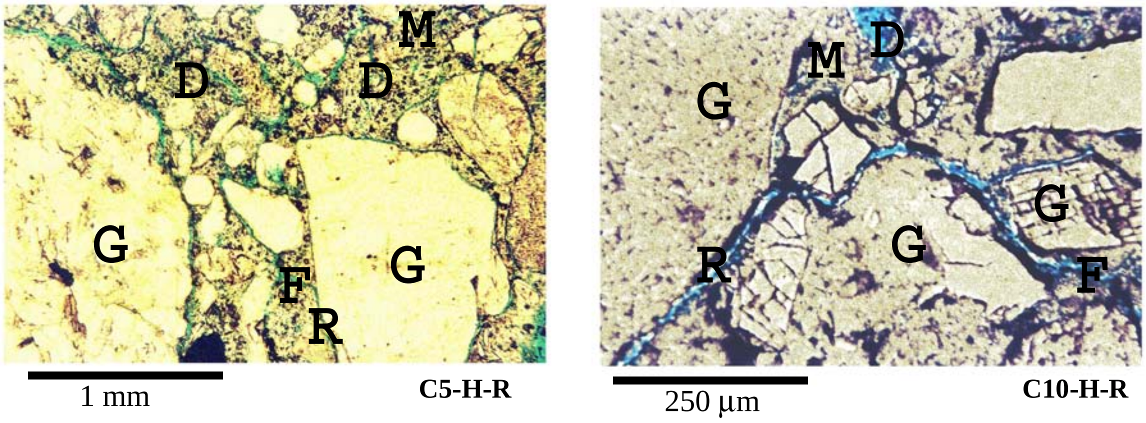

C5 hydrostatic (14-day)   C10 hydrostatic (3 day)

Figure 49. Thin section (plane light) images illustrating distinct deformation mechanisms within hydrostatically-tested 14- and 3-day cured samples. Fractures (F) and blue-dye 'rind' (R) interact at discrete locales, but never form cohesive strain accommodation zones beyond ~2 grain/lithic fragment domains.

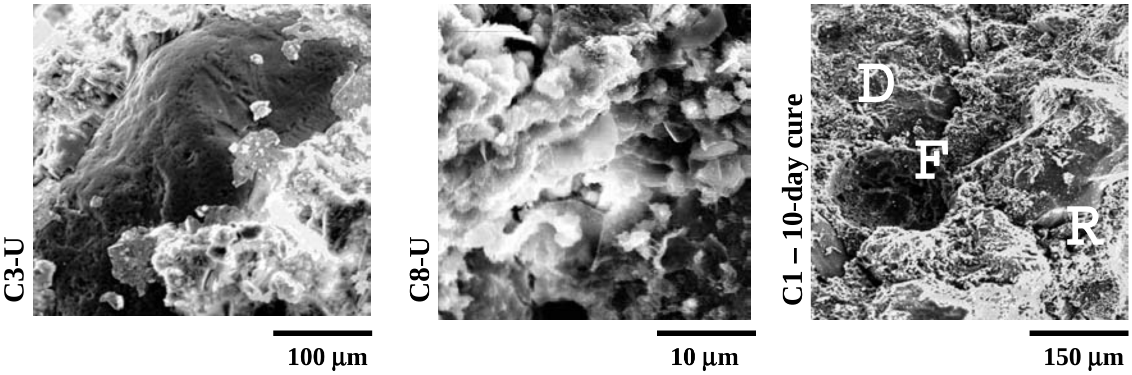

A grain-CAH untested

B CAH matrix

C deformation accomodation

Figure 50. SEM/SE images illustrating concrete medium components. See text for additional discussion.

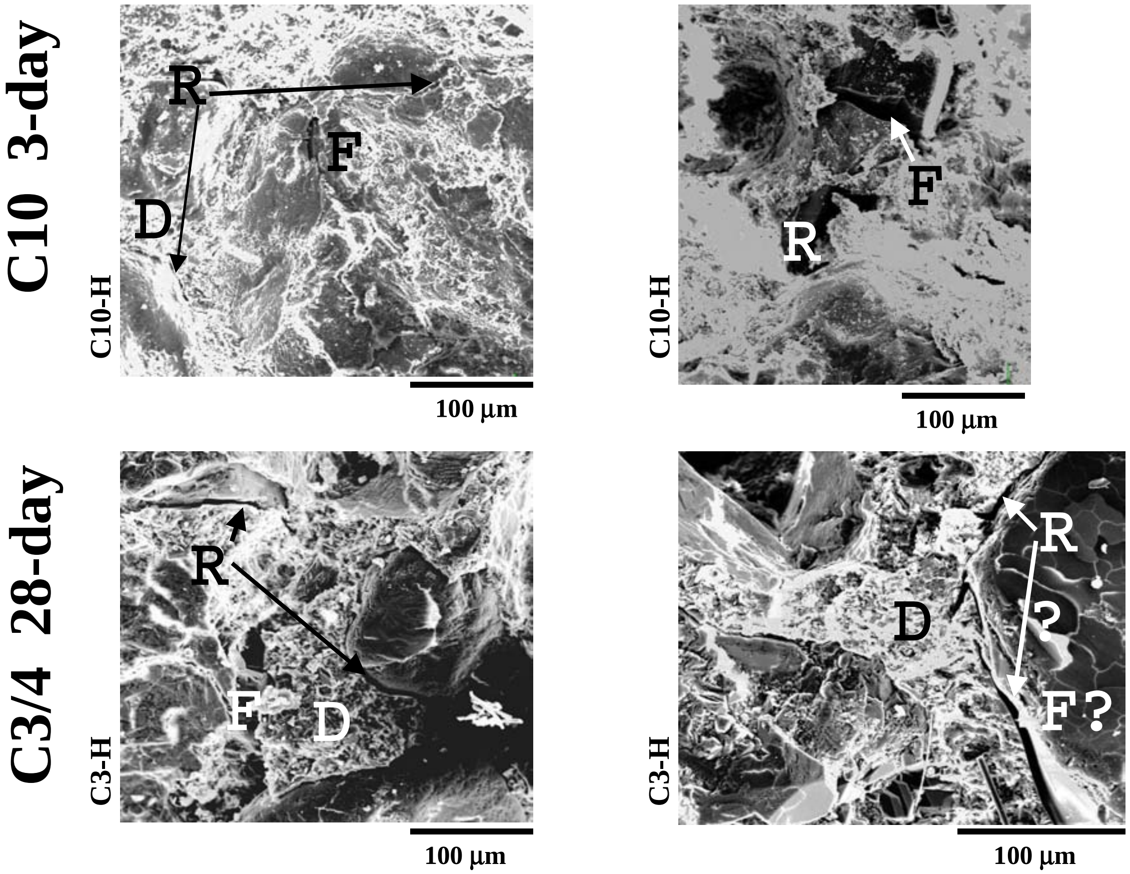

Figure 51. SEM/SE image comparison of cure-time endmembers (3- and 28-day, respectively) after hydrostatic testing. Deformation modes R and F are identified. See text for additional discussion.

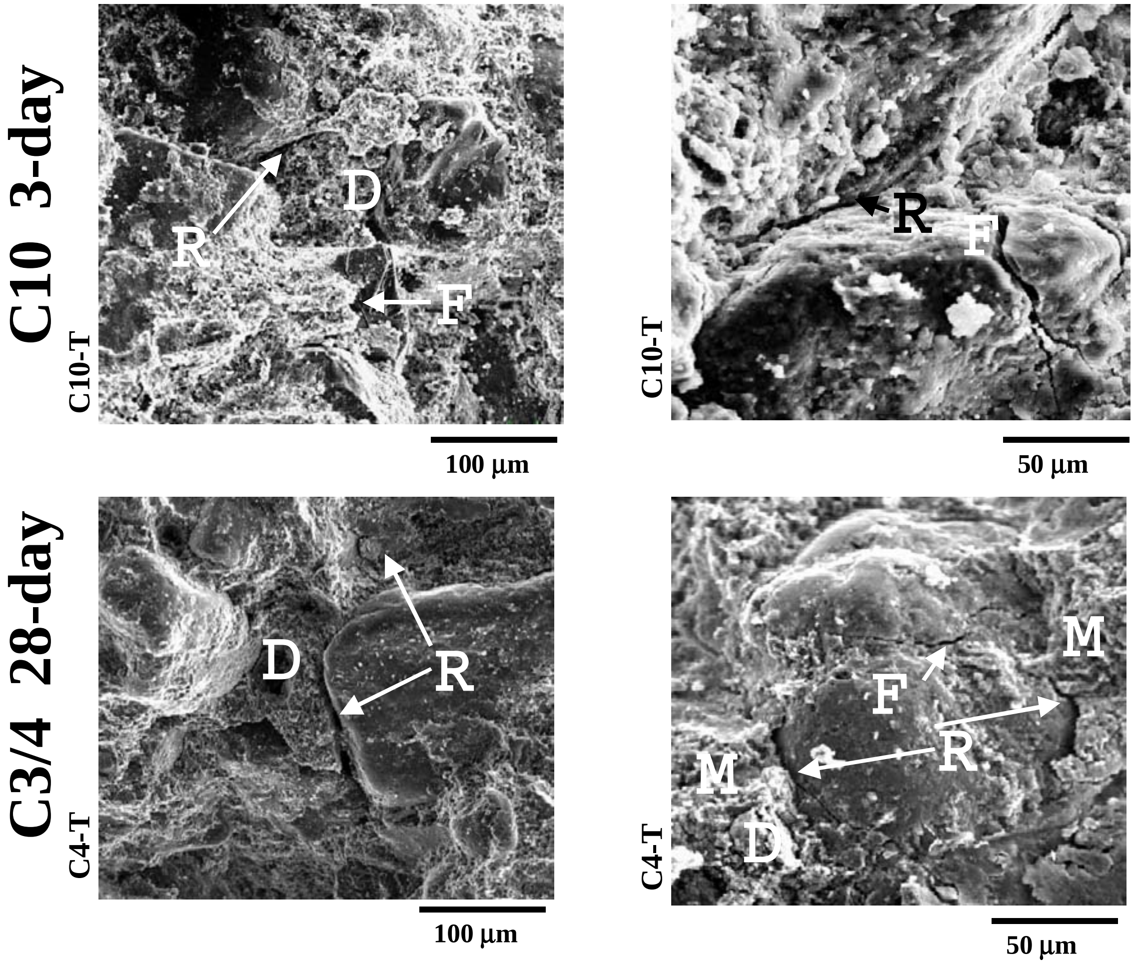

Figure 52. SEM/SE image comparison of specimens from cure-time end members (3- and 28-day, respectively) after explosive loading. Samples were taken ~0.25" from inner wall of tested cylinders. Images are oriented looking radially outward (z-θ plane). Although grain fractures are identified in these images, the qualitative assessment of grain-cracking as revealed in the radially-logged thin sections indicates that deformation was less than that experienced under the hydrostatic tests.

Analysis of Experiments

Our overall goal was to develop an experimental approach to the problem of understanding target response to penetration. A technique was sought that would be more flexible than a real penetration event and allow more instrumentation and greater control over the target deformations.

A secondary goal was to make progress toward creation of a science-based S number. The S number has proved very useful as a pragmatic approach to predicting penetration depths, but the only way to determine S is to do penetrator experiments. It is not always possible or desirable to do a series of penetrator tests, so it would be useful to have an approach that yielded the equivalent of S, but in a more tractable and impartial way.

Several types of information were collected to characterize the effects of the explosive loading of the concrete: accelerations, strains, elastic wave speeds and microscopic imaging. In addition, the various pours of concrete were characterized by determining unconfined compressive strength, triaxial strength and strains, tensile strength, porosity and moisture content. The balance of the report is an analysis and discussion of the results of the various data, with an emphasis on those directly related to the explosive loading.

Results of Accelerometer Measurements

Accelerometers were used to observe the stress wave propagating outward from the explosion. From the acceleration data, the speed of the stress wave can be measured from the travel time between accelerometers at known distances. By integrating the accelerations, particle velocities can be determined, and a second integration gives the displacement. The travel time to the exterior of the specimen was about 200 microseconds, and the rarefaction wave from the exterior, free surface would reach the center in a similar time. Our intention was to study the effects of the explosive loading, not the nearly endless ringing of reflected waves. Therefore we only show most data for times less than 500 microseconds, or slightly more than one round trip.
The following plot series presents the accelerations and associated particle velocities for all the accelerometers that clearly functioned properly, with an accompanying brief discussion of each data set. Accelerometers on the borehole wall, directly exposed to the explosion, are a special case, to be discussed later. The results derived from each test are summarized in Table 11.

Cylinder 1, Test 1, 9 Day

What turned out to be a very large explosive loading was used on the first cylinder. As a result, only one of the three accelerometers on this specimen functioned properly. In Figure 53a, acceleration measured on the outer surface, 457 mm from the explosion showed that the compressive wave arrived at the outer surface about 165 microseconds after detonation. Apparently the accelerometer was damaged, as evidenced by the constant acceleration after peaking at 17,000 m/s^2 which is below the rating of the accelerometer. The velocity, from integrating the acceleration –time data, was only about 0.2 m/s at that point and is meaningless after about 200 microseconds (Figure 53b).

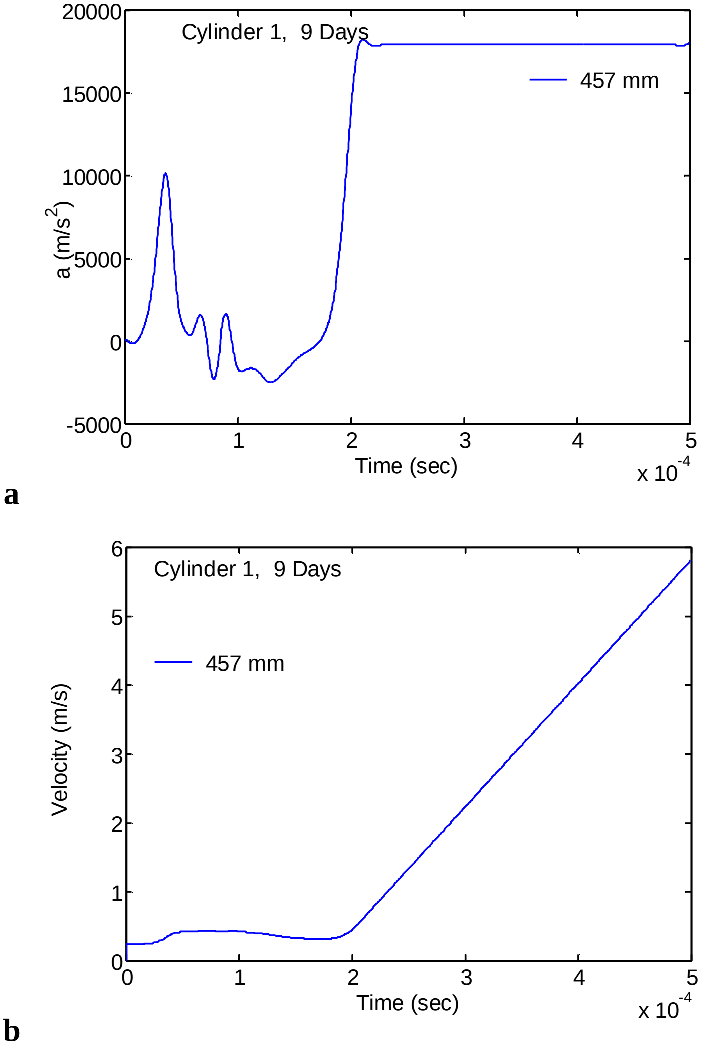

Figure 53. Cylinder 1 - (a) Accelerations and (b) velocities for all accelerometers that functioned. Only the first 500 microseconds of data are shown.

Cylinder 2, Test 2, 10 Day

A second test cylinder (Figure 54) was tested with a substantially lower explosive loading (262 g C-4). A 2kg accelerometer on the exterior surface provided what appears to be sensible results, even though overrange, reaching a peak acceleration of 35,000 m/s^2 which raised the particle velocity to 3.2 m/s. Figure 54a shows a broad wave of acceleration, with a period of perhaps 300 microseconds.

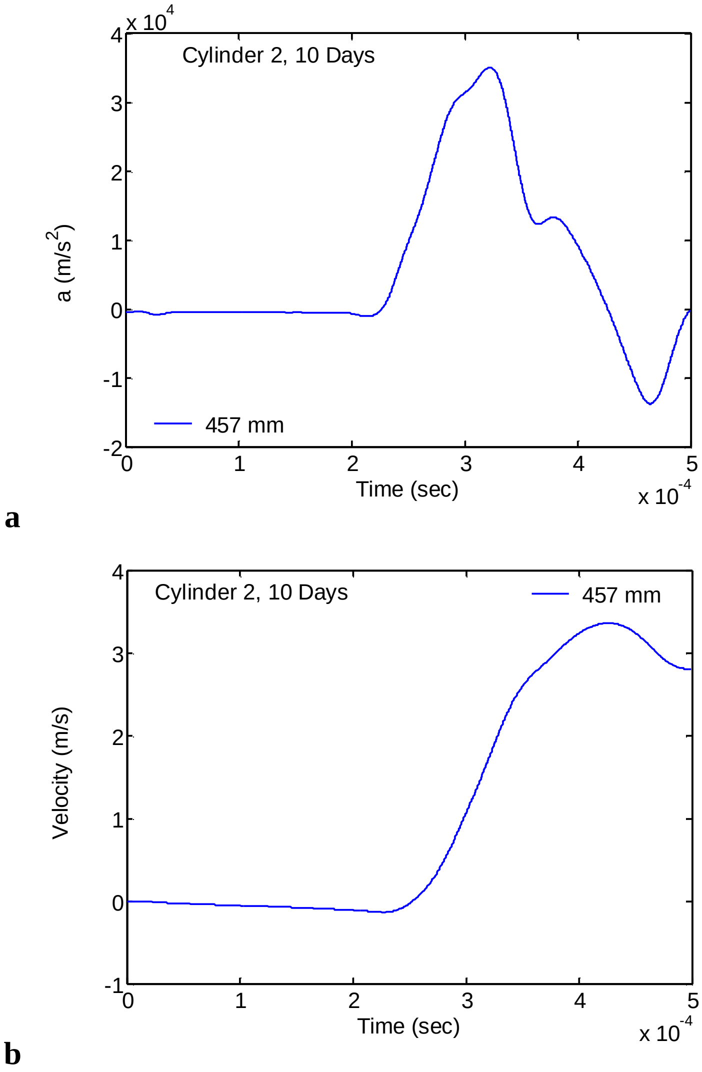

Figure 54. Cylinder 2 - (a) Accelerations and (b) velocities for all accelerometers that functioned. Only the first 500 microseconds of data are shown.

Cylinder 7, Test 3, 7 Day

Only the 2 kg accelerometer on the exterior yielded clean results. A clean signal shows a stress wave arriving at 199 microseconds and reaching a peak acceleration of 37,000 m/s^2 with a very slow return to zero or negative acceleration (Figure 55a). As a result of the lengthy interval of positive, although declining, acceleration, particle velocities reached 4 m/s, which was somewhat higher than usual (Figure 55b).

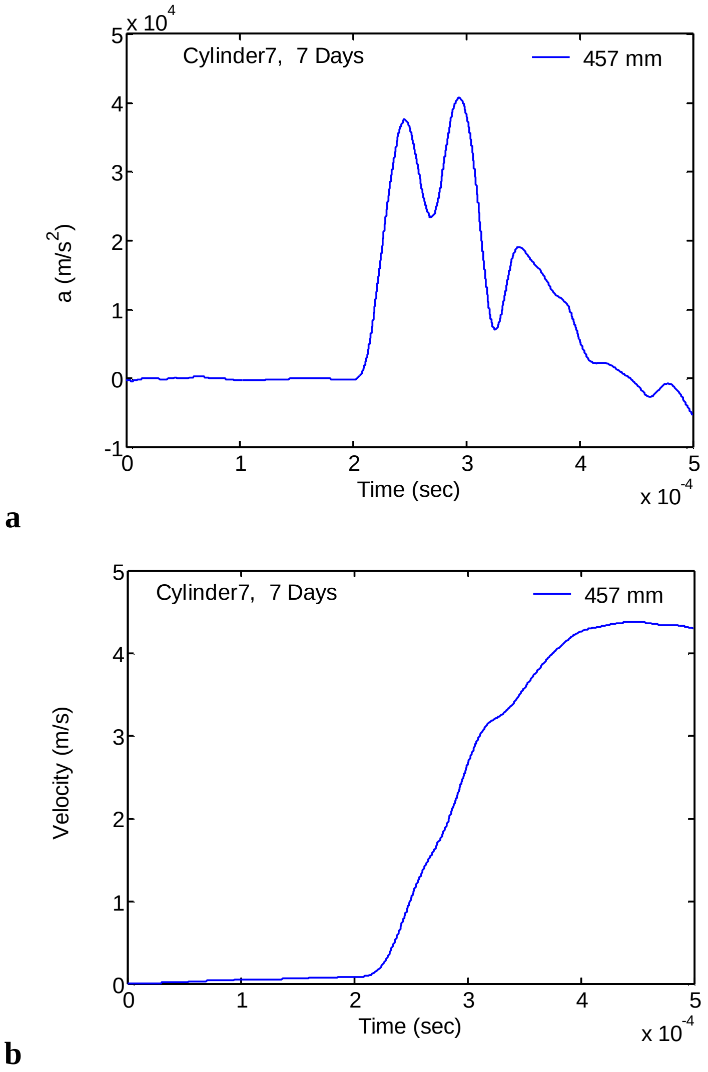

Figure 55. Cylinder 7 - (a) Accelerations and (b) velocities for all accelerometers that functioned. Only the first 500 microseconds of data are shown.

Cylinder 8, Test 4, 7 Day

Accelerometers on Cylinder 8, the second cylinder cured for 7 days, fared no better than those installed on Cylinder 7. Arrival times could be determined and are recorded in Table 11, but no reliable peak accelerations could be determined. From Figure 56a, it is clear that the 2kg accelerometer was not functioning properly, clipping at 750 g's, well below its rating. Velocities could not be calculated beyond the clipping point.

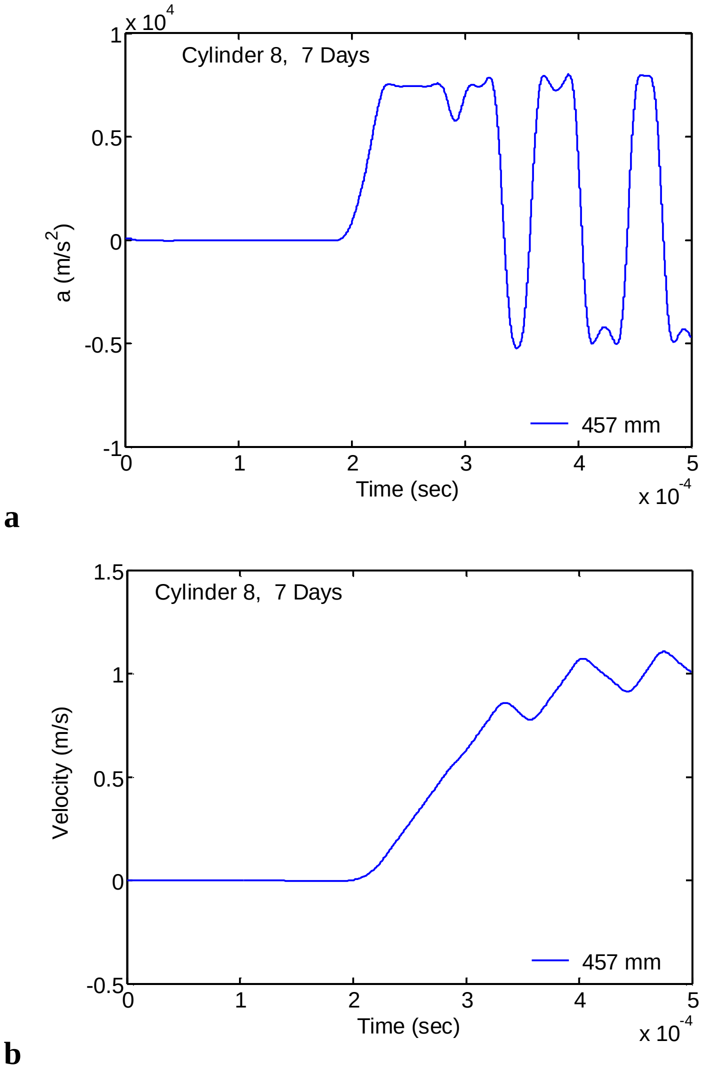

Figure 56. Cylinder 8 - (a) Accelerations and (b) velocities for all accelerometers that functioned. Only the first 500 microseconds of data are shown.

Cylinder 9, Test 5, 3 Day

It appeared that the 200kg accelerometer on the interior borehole wall might have yielded a valid measurement Figure 57a, (blue line). Extensive filtering was required to reduce the noise, resulting in an apparent acceleration curve. However, the arrival time is around 100 microseconds which is too late to be consistent with 50.8 mm separation between explosive and accelerometer face. If the signal is real, it does not represent the acceleration at 50.8 mm. Once again the exterior accelerometer functioned well, measuring a peak acceleration of 23,000 m/s^2 and, after integration, a peak velocity for the exterior surface of 2.1 m/s.

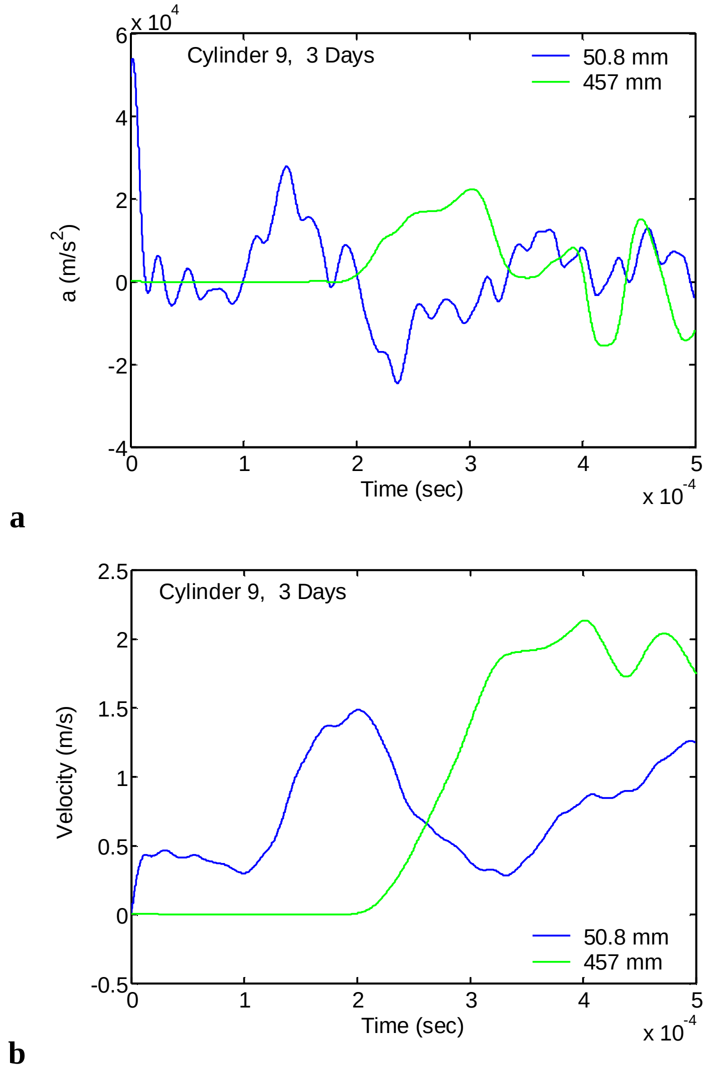

Figure 57. Cylinder 9 - (a) Accelerations and (b) velocities for all accelerometers that functioned. Only the first 500 microseconds of data are shown.

Cylinder 10, Test 6, 3 Day

Test 6 was the first test with the reconfigured accelerometers (see Figure 12). The innermost accelerometer was moved to 152 mm (6 inches) from the explosive, placing 100 mm of concrete between them. Difficulties installing the accelerometer in the newly-bored hole resulted in a poor coupling and unreasonably low accelerations (Figure 58a) at 152 mm. A clean acceleration record was obtained at 457 mm and the integrated acceleration showed that the exterior surface reached a peak velocity of 2 m/s (Figure 58b). Arrival times for both accelerometers are reasonable at 96 and 160 microseconds, respectively.

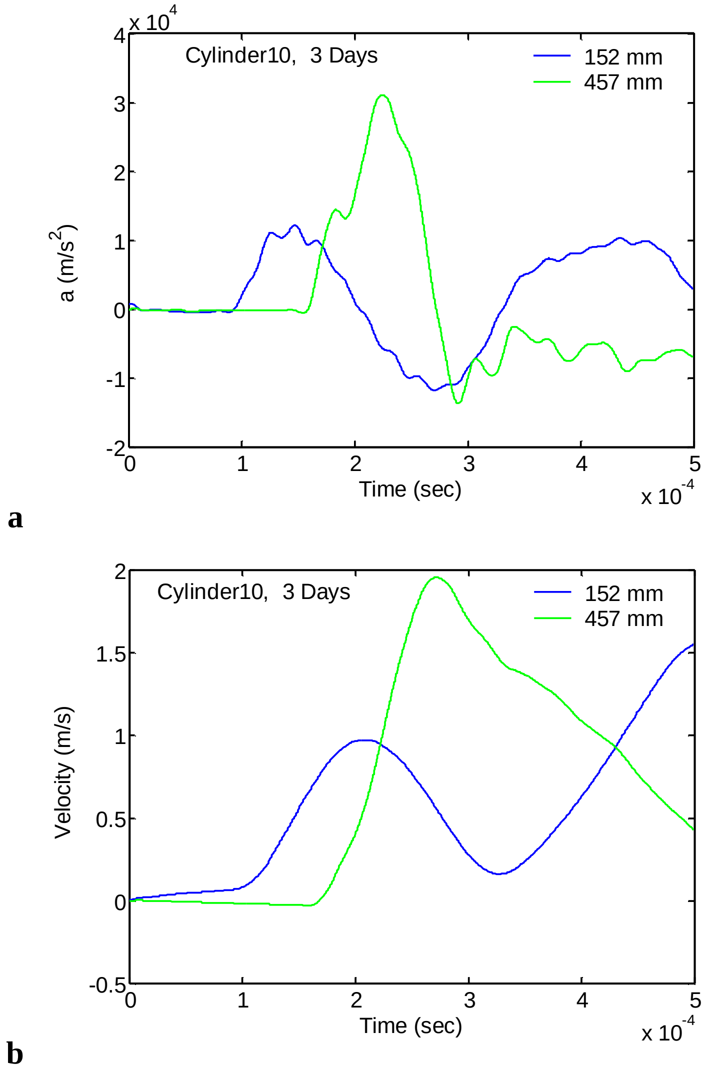

Figure 58. Cylinder 10 - (a) Accelerations and (b) velocities for all accelerometers that functioned.

Cylinder 6, Test 7, 14 Day

Data were obtained at all distances, 152, 203 and 457 mm from the explosion. The accelerations at 203 mm seem small and the arrival time precedes the arrival of the stress pulse at 152 mm, a physical impossibility. Most likely this is an installation problem. After the installation configuration was changed, new emplacement holes were drilled and cored and we had difficulty getting as high a quality as we would have liked. Acceleration at 152 mm reached 39,000 m/s^2 with an arrival time of 93 microseconds (blue line, Figure 59a). At the exterior, the stress wave arrived after 151 microseconds, giving an apparent wave velocity between 203 mm and 457 mm of 3.58 km/s, in good agreement with the post-test velocity measurements (Figure 35) in the region. Note that the acceleration at the outer surface is essentially identical to the acceleration observed at 152 mm from the explosion. Geometric spreading reduces the acceleration by r$^{-1/2}$, so the acceleration should decrease by a factor of 0.57 between 152 and 457 mm. The free surface then amplifies the acceleration by a factor of 2, leaving the amplitude essentially unchanged, and that is what is observed in Figure 35. Velocities were similarly affected.

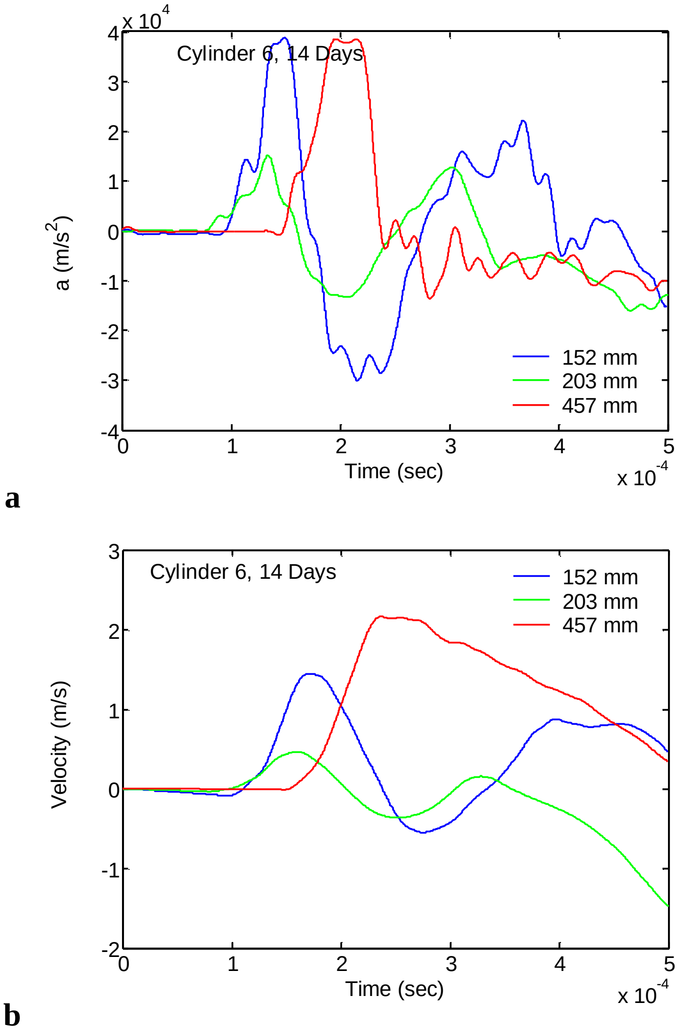

Figure 59. Cylinder 6 - (a) Accelerations and (b) velocities for accelerometers that functioned. Only the first 500 microseconds of data are shown.

Cylinder 5, Test 8, 15 Day

Results for Cylinder 5 (Figure 60) tested at 15 days after pouring are very similar to the results of Cylinder 6 (Figure 59).

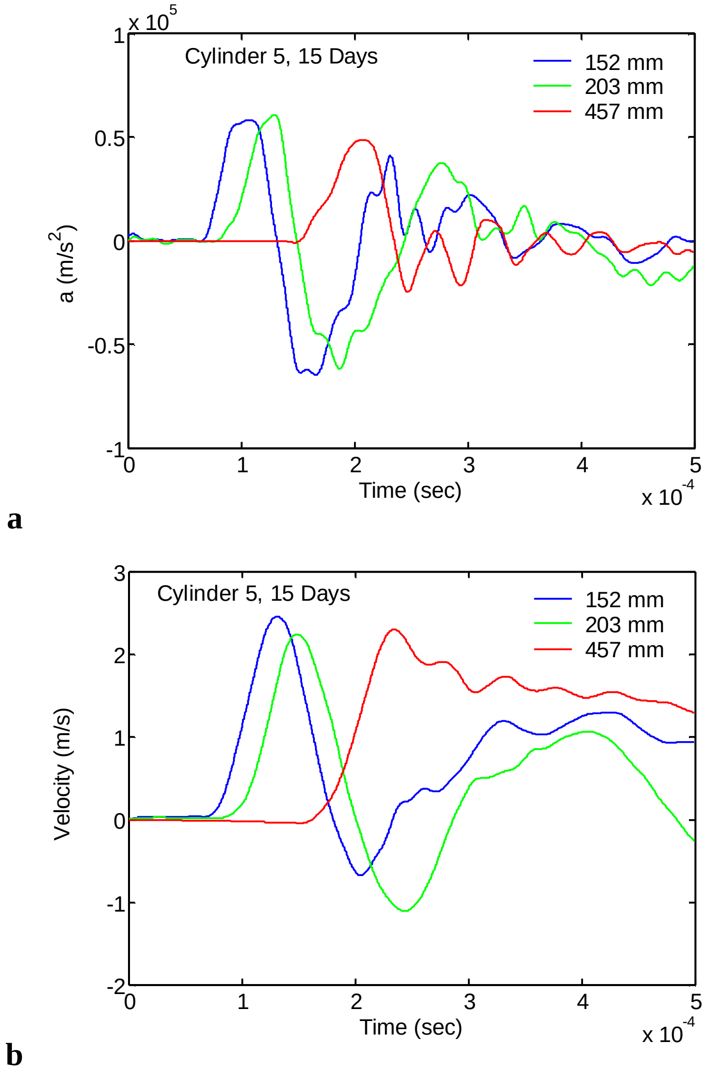

Figure 60. Cylinder 5 - (a) Accelerations and (b) velocities for all accelerometers that functioned. Only the first 500 microseconds of data are shown.

Cylinder 3, Test 9, 28 Day

A good data set was obtained for Cylinder 3 tested at 28 days (Figure 61). Of interest here is the reduction in acceleration between 152 and 203 mm, as expected from geometric spreading, and the subsequent increase as the free surface amplifies the acceleration at 457 mm.

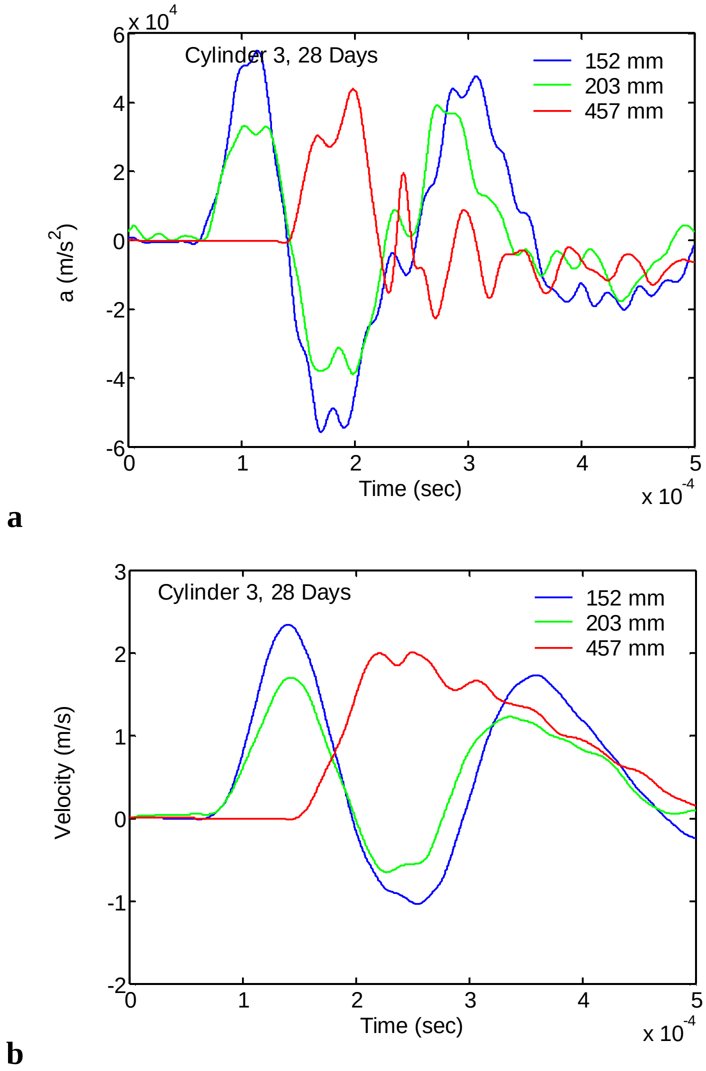

Figure 61. Cylinder 3 - (a) Accelerations and (b) velocities for all accelerometers that functioned. Only the first 500 microseconds of data are shown.

Cylinder 4, Test 10, 28 Day
Results for cylinder 10 tested at 28 days are similar to the other 28 day specimen (Figure 61). The arrival times at 152 mm is very close to the arrival time at 203 mm; the apparent wave speed would be 8.47 km/s which is unlikely to be true. The problem is again the difficulty of installing the accelerometes to accurately known depths in the holes drilled post-casting. In future work, holes will be cast in, making accurate depth control more feasible.

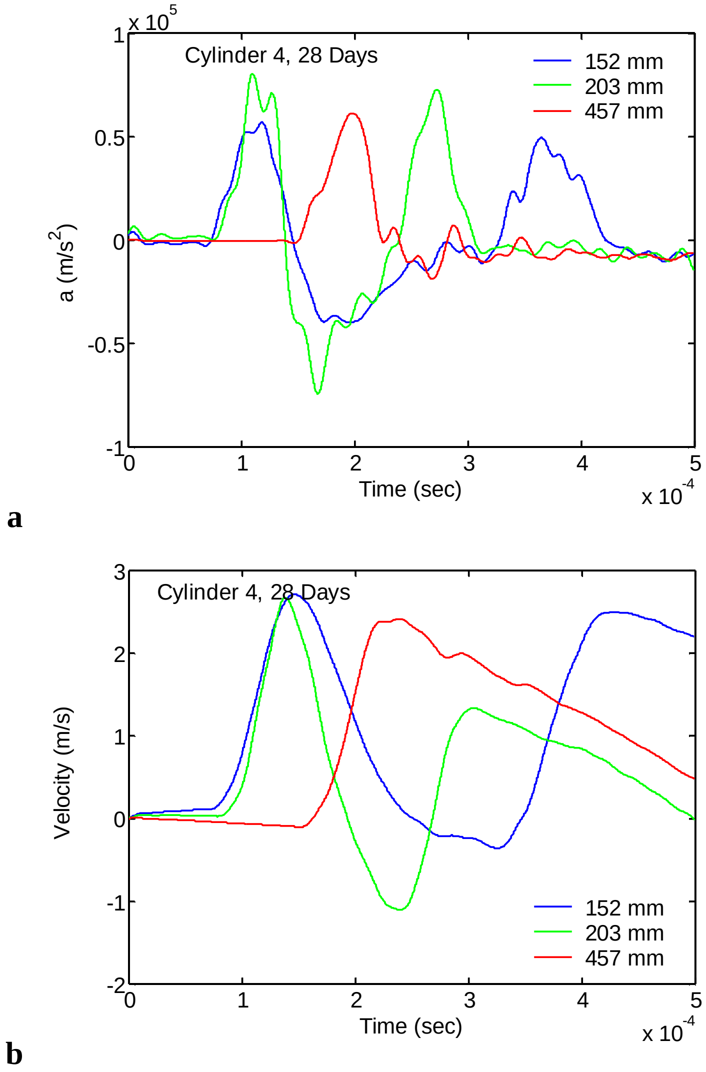

Figure 62. Cylinder 4 - (a) Accelerations and (b) velocities for all accelerometers that functioned. Only the first 500 microseconds of data are shown.

Results obtained from the accelerometers are summarized in
Table 11 and Figure 63, Figure 64 and Figure 65. One column of
Table 11 requires explanation; column 6, with the heading (V_P km/s) tabulates the apparent velocity of the stress wave generated by the explosives as it propagates between accelerometers. The velocity is simply the nominal distance between the accelerometers divided by the difference in arrival times of the stress wave at the corresponding

accelerometers. If the wave is propagating as an elastic wave, then this velocity should be similar to V_P measured on the as-poured samples (Figure 34) which was around 3.5 km/s. A value different from this indicates either problems with data or propagation through damaged material. Most of the deviations are the result of data errors, or are associated with suspect accelerometers. However one example may indicate propagation in damaged material; Cylinder 7 had two accelerometers on the borehole wall and two on the exterior. The arrival times for the accelerometers on the borehole at 50.8 mm were almost identical—57 and 58 microseconds, giving credence to the values even though the accelerometers were overranged. At the exterior, the arrival times translate into low values for V_P—3.2 and 2.88 km/s. As will be discussed later, Cylinder 7 apparently was damaged all the way to the exterior. This damage may be reflected in the low apparent velocities of the stress wave.

Table 11. Data on accelerations and velocities observed during explosively-driven cylinder tests.

Cyl #	Age days	Range g=9.8m/s^2	r mm	$T_{Arrival}$ x10^{-6}s	V_P km/s	a $_{Peak}$ (m/s^2)	V $_{Peak}$ (m/s)	Comments	Expl.
1	9	200kg	50.8	18		1,200,000		200k, first cycle to 1,200,000 looks valid	COMP-4
1	9	1kg	457.2	126	3.76			clipped at 17000	COMP-4
1	9	100g	457.2	165	2.76			clipped at 8000	COMP-4
2	10	200kg	50.8	15		2,000,000		overranged but plausible	COMP-4
2	10	200kg	152.4					no data	COMP-4
2	10	2kg	457.2	216	2.02	35000	3.2		COMP-4
3	28	200kg	152.4	64		53000	2.14		PETN
3	28	200kg	203.2	67	16.93	33000	1.87		PETN
3	28	20kg	457.2	140	3.48	43000	1.96		PETN
4	28	200kg	152.4	69		57000	2.8		PETN
4	28	200kg	203.2	75	8.47	80000	2.63		PETN
4	28	20kg	457.2	146	3.58	60000	2.5		PETN
4	28	2kg	457.2						PETN
5	15	200kg	152.4	68		62000	2.37		PETN
5	15	200kg	203.2	83	3.39	64000	2.27		PETN
5	15	20kg	457.2	155	3.53	50000	2.37		PETN

Cyl #	Age days	Range g=9.8m/s^2	r mm	$T_{Arrival}$ x10^{-6}s	V_P km/s	a $_{Peak}$ (m/s^2)	V $_{Peak}$ (m/s)	Comments	Expl.
6	14	200kg	152.4	93		42000	1.5		PETN
6	14	200kg	203.2	80	-3.91	16000	0.5		PETN
6	14	20kg	457.2	151	3.58	38000	2.09	output clipped by oscilloscope	PETN
6	14	2kg	457.2	168	2.89	30000	1.31		PETN
7	7	200kg1	50.8	57		400,000	28		PETN
7	7	200kg2	50.8	58					PETN
7	7	2kg1	457.2	185	3.20			went flat and started ringing	PETN
7	7	2kg2	457.2	199	2.88	37000	4.4		PETN
8	7	200kg1	50.8					200k1 no useful data	PETN
8	7	200kg2	50.8	76				200k2 pick is a little shaky	PETN
8	7	2kg	457.2	185	3.73	7500	0.85	2k, ringing after first cycle	PETN
8	7	100g	457.2	175	4.11			100, overranged	PETN
9	3	200kg	50.8	92				no data	PETN
9	3	20kg	457.2	189	4.19	23000	2.1		PETN
10	3	200kg	50.8	96				poor quality signal	
10	3	*20kg*	457.2	160	6.35	31000	1.96		PETN

Peak values for accelerations (a $_{Peak}$) and particle velocities (V_{Peak}) are included in Table 11 and can be used as a measure of energy transport and absorption. Accelerations were surprisingly consistent for accelerometers embedded in the concrete; Figure 63a plots all the valid accelerations measured as a function of distance from the explosives and separated by Cylinder #. For tests in which multiple accelerometers functioned, a line is drawn between the related acceleration values to show the change with distance from the explosives. At 152 mm, with 100 mm of concrete between the explosion and the accelerometers, the values cluster around 50,000 m/s^2 or 5kg's. Accelerations at the next largest radial distance, 203 mm, are more scattered. On the exterior surface the accelerations ranged from 25,000 to 50,000 m/s^2, averaging a little lower than at the innermost accelerometers.

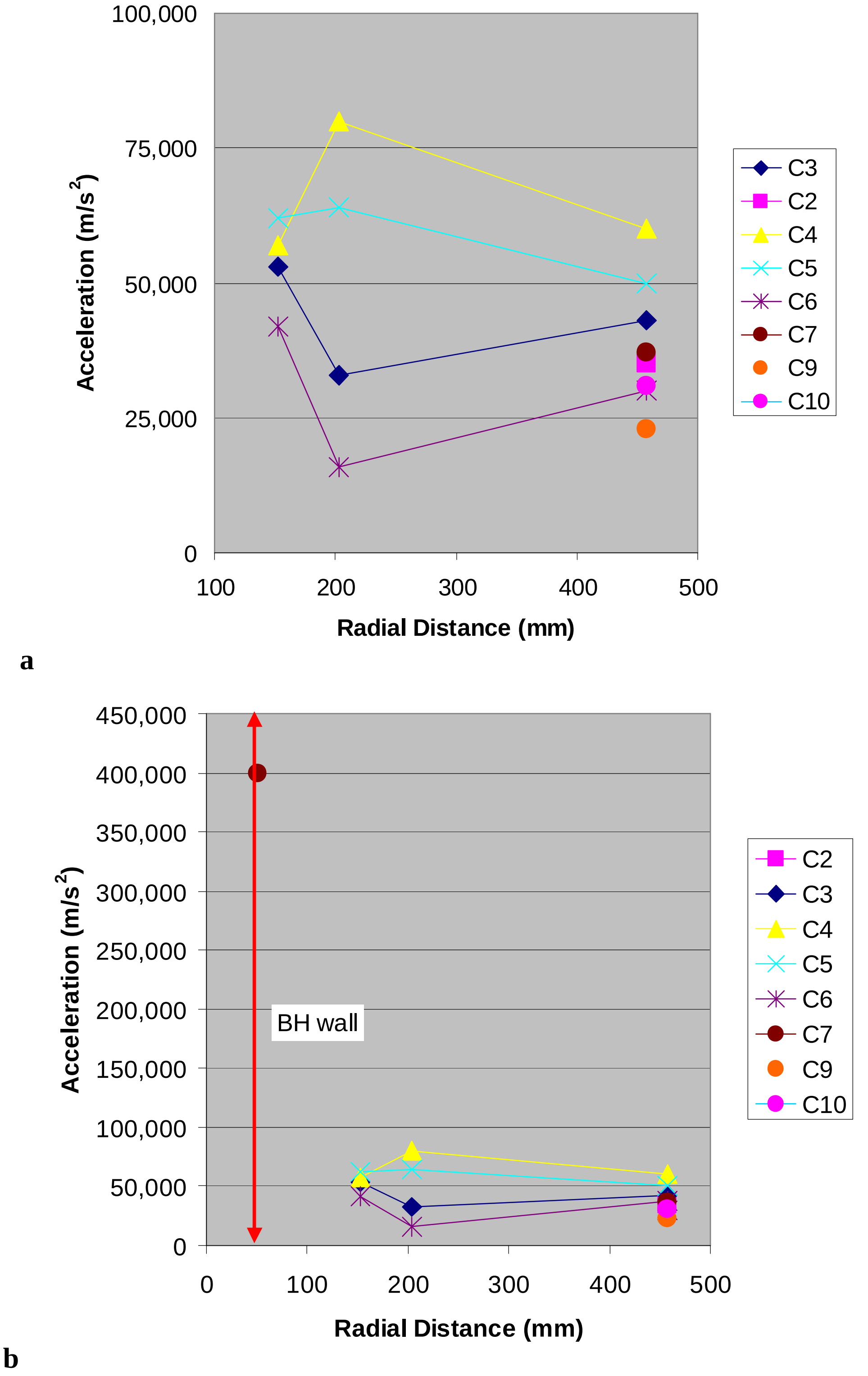

Figure 63. (a) an expanded view of the low acceleration regime observed beyond 100 mm and (b) accelerations as function of distance from the explosive source, including the very high accelerations at the borehole wall.

Lines connecting data points from the same test make it clear that the acceleration at the exterior was roughly equal to the acceleration at the innermost accelerometer. This was discussed earlier for Cylinder 6, Test 7 (Figure 59) as being the result of geometric spreading being cancelled out by the amplification of the free surface. If the accelerations were greatly different that would be evidence for non-linear, damaging, processes occurring along the path. Unfortunately, only exterior accelerations were obtained for Cylinder 7, the one test where we seemed to see evidence of such damaging processes.

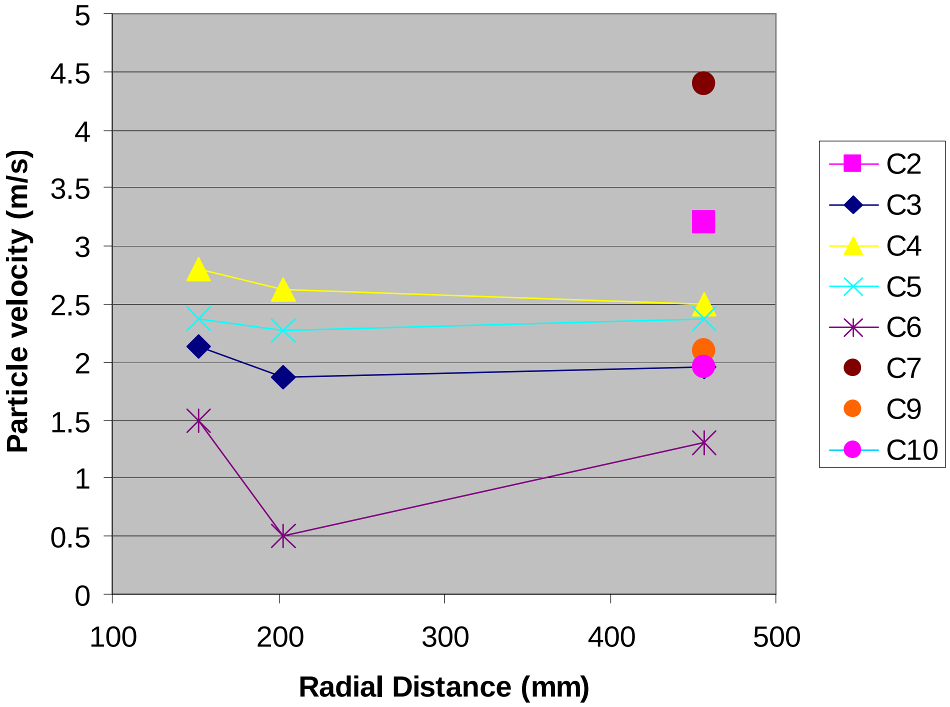

Figure 64. Velocities for all useable accelerometer records. Lines connect those points where all three accelerometers functioned, allowing the gradient of velocity to be observed.

Initially we were inclined to discard all data from the accelerometers installed flush with the borehole wall at a distance of 50.8 mm from the explosion and exposed directly to the explosion. Measured accelerations were very high and in most cases exceeded the range of the 200kg accelerometer, damaging or destroying it. However, closer examination of the data resulted in the conclusion that some of the data appears to be valid. The first test on Cylinder 1 used 4 times as much explosive as the later tests, rubbleizing the specimen and destroying the accelerometer. However, as Figure 13 shows, the first few microseconds after the stress wave arrived at the accelerometer produced a short, well-defined peak in acceleration reaching 120kg or 1,200,000

m/s^2 before the signal went off-scale. This is well within the 200kg range of the accelerometer and there is no obvious reason to ignore the data. A second example is somewhat less plausible, at least as far as the peak; Cylinder 2 (Figure 14a) also shows a clear signal with an abrupt emergence from the baseline, and a peak value of 300 kg, which is somewhat beyond the range of the accelerometer and thus should not be trusted to high precision. Subsequent behavior does not seem to indicate a destroyed device. Finally, the innermost accelerometer on Cylinder 7 (Figure 15a) detected a stress wave arriving at the appropriate time with a subsequent peak at 40kg or 400,000 m/s^2. Immediately after that peak the accelerometer was driven off scale, but there is no obvious reason to doubt the peak value achieved prior to the overranging.

These values are at least an order of magnitude higher than the accelerations reliably observed a few mm away which were consistently in the 5kg (50,000 m/s^2) range (Figure 63a). The most conservative of these data, that from Cylinder 7, is plotted on an expanded scale in Figure 63b with a line added to indicate the position of the borehole wall. The explosives were at 0 mm. Assuming that the data from the accelerometers closest to the explosion can be trusted, then some mechanism is absorbing a tremendous amount of energy from the stress wave over the 100 mm distance to the next set of accelerometers at 152 mm. For greater radial distance, the wave propagated elastically, or nearly so. Scoping calculations done with Auto-Dyne, a commercial finite element code, indicated the possibility of such high accelerations.

Integration of the acceleration-time records gives the particle velocity at the accelerometer location and provides a sanity check on the validity of the acceleration. Unphysical accelerations will produce velocities that are not reasonable by comparison with others determined on the same sample or similar samples. All useable velocity data are shown in Figure 64, with lines connecting those data points which were determined on the same sample. As with the accelerations, velocities within one sample were almost constant, although there was significant variation between samples. Not shown is the velocity calculated at the innermost accelerometer from Cylinder 7, the accelerometer that seems to show 40kg accelerations. The integrated acceleration indicates a particle velocity of 28 m/s.

Accelerations at the exterior surface reflect the energy absorbed by the intervening concrete. One of the premises of this work was that differences in cure time, and thus strength, would be reflected in the energy absorption in a way that correlated with penetrability. The first step towards that goal is shown in Figure 65, where all accelerations measured on the exterior surface are plotted as a function of cure time. The black line is a least squares fit to the data and it shows a strong increase in transmitted energy as the age, and strength, of the concrete increased. If the energy is not being absorbed then the material is not being damaged, crushed, or otherwise deformed in the irreversible, energy-absorbing manner required to allow a penetrator to penetrate.

Results of velocity measurements

An extensive set of measurements was made to determine the elastic wave velocities in the as-poured concrete, hydrostatically loaded concrete and the explosively loaded concrete, using specimens cast at the same time as the main pour for the first two and cores retrieved from the cylinders post-test for the third set of data. Results are shown in Figure 33, Figure 34, and Figure 35, and Table 6Table 7Table 8. In addition to characterizing the concrete and the differences between pours, the velocity measurements can be used to assess the damage done by the explosion, its magnitude and spatial extent. Damage is frequently defined as the ratio of a degraded elastic modulus to the same modulus for undamaged material. Thus velocity squared (eg. V_P^2) directly measures an elastic modulus, with a correction for density. Thus comparison of the velocities after damaging processes can be used to measure damage and can precisely delineate the zones of high and low or no damage.

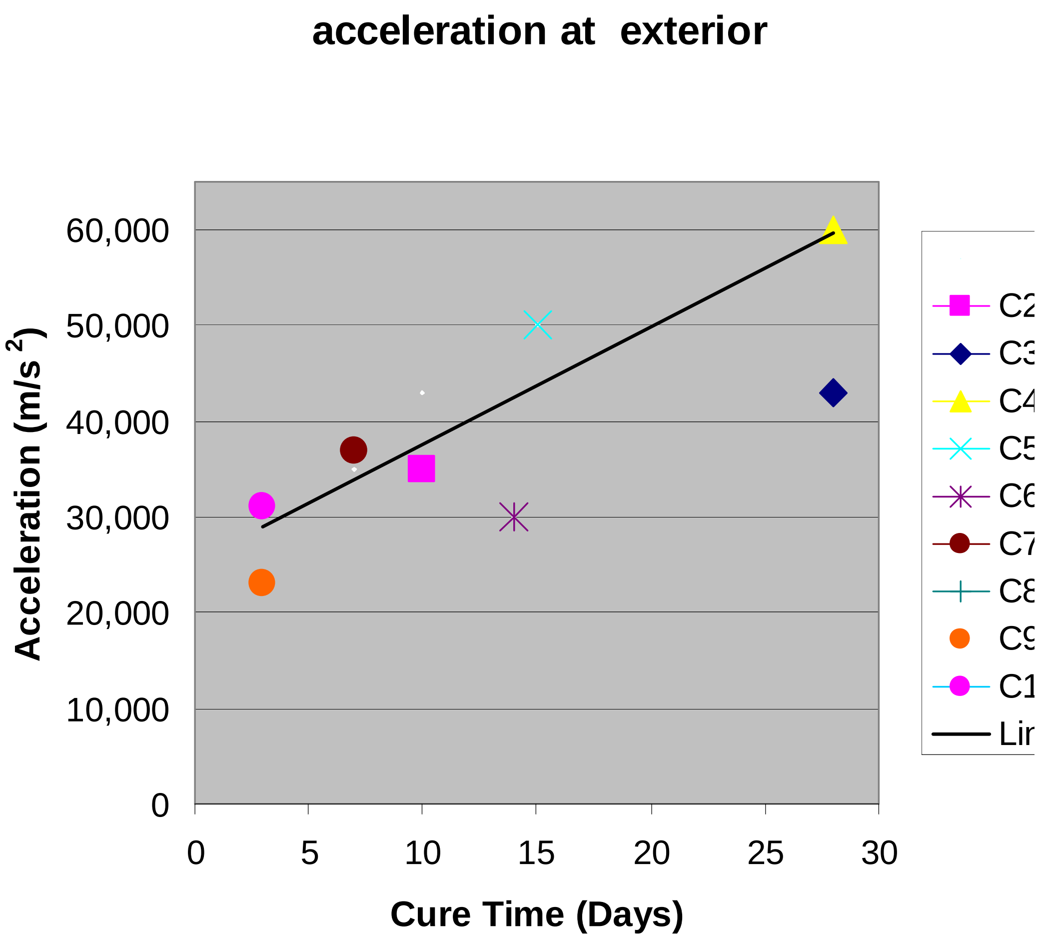

Figure 65. Radial accelerations measured on the exterior of the specimens as a function of cure age showing an increase for older, stronger specimens.

In Figure 66, V_P measured on cores retrieved from the explosively-loaded cylinders (see Elastic Wave Velocities, p.61 for details) is plotted with two different normalizations. Figure 66a normalizes the velocities using V_P measured on the hydrostatically loaded specimens from the corresponding pour. In Figure 66b, the normalization is to the as-poured specimens.

Normalizing with respect to the velocities measured on hydrostatic loaded specimens allows an estimate of the stresses that the explosively-loaded material had been exposed to during the test. Normalized values near 1 would be associated with stresses similar to the pressures applied in the hydrostatic tests. A complication arises from the moisture content; as discussed in Triaxial and Hydrostatic Loading, p. 76, at a certain pressure the dry porosity had been removed and the saturated sample became much stiffer. No further damage was occurring past the lockup point, as evidenced by the linear loading and unloading with little hysteresis. Thus the velocity change is determined by the lockup stress during hydrostatic loading. Because of the range of lockup stresses, caused by a range of moisture contents, this stress measure gives a crude answer. Most of the lockup stresses were about 50 MPa. Normalized measurements on C10 and C7, tested at 3 and 7 days cure respectively, are shown in Figure 66a as the two lower lines. Near the borehole, the normalized values approach 1, implying that stresses reached at least 50 MPa, a value not too different from the 80 MPa borehole pressure predicted by Auto-Dyne. The other normalized measurements from cylinders C6 and C4, tested at 14 and 28 days, were much higher. As the explosive loading was the same for all these tests, the difference in damage must reflect the greater strength of the cylinders cured longer. All tests show a zone extending about 50 mm radially outward from the borehole within which the normalized velocities are increasing before becoming relatively constant. Note that these plots have zero at the borehole wall, not at the center of the cylinder.

When normalized to the as-poured specimens (Figure 66b), the values are a measure of damage. A value of 1 means that the velocity in the explosively-loaded material is the same as the velocity in the as-poured material, which by definition is undamaged. As damage increases, elastic wave velocities decrease and the ratio decreases. As mentioned above, damage is really measured by the square of the velocity, corrected by the density, but the picture is the same. Again, a narrow zone of highly damaged material was observed that extended from the borehole wall at 0 mm to a depth of about 50mm. Over this region, the normalized velocity increased to approximately 1 for the 14 and 28 day tests, and about 0.9 for the 3 and 7 day tests. Stronger concrete confined almost all of the damage to the 50 mm zone. The weaker 3 and 7 day concrete was damaged over most of the thickness, although most severely in the 50 mm zone. There is some indication of an increase in damage for C7, the 7 day concrete, at the outer surface. This would be consistent with tensile stresses resulting from the stress wave reflecting off the free surface. Indeed we had expected that there might be circumferential cracking caused by this effect, but little evidence beyond this one point, was found for it. No macroscopic tensile cracks were observed, implying that the impedance match provided by the wet sand buffer may have been better than anticipated.

Implications of Experimental Results

The clearest implication comes from the narrow damage zone that was delineated by the velocity measurements and possibly by the acceleration measurements. Beyond about 50 mm, the energy of the explosion had been dissipated to such an extent that the stress wave propagated elastically.

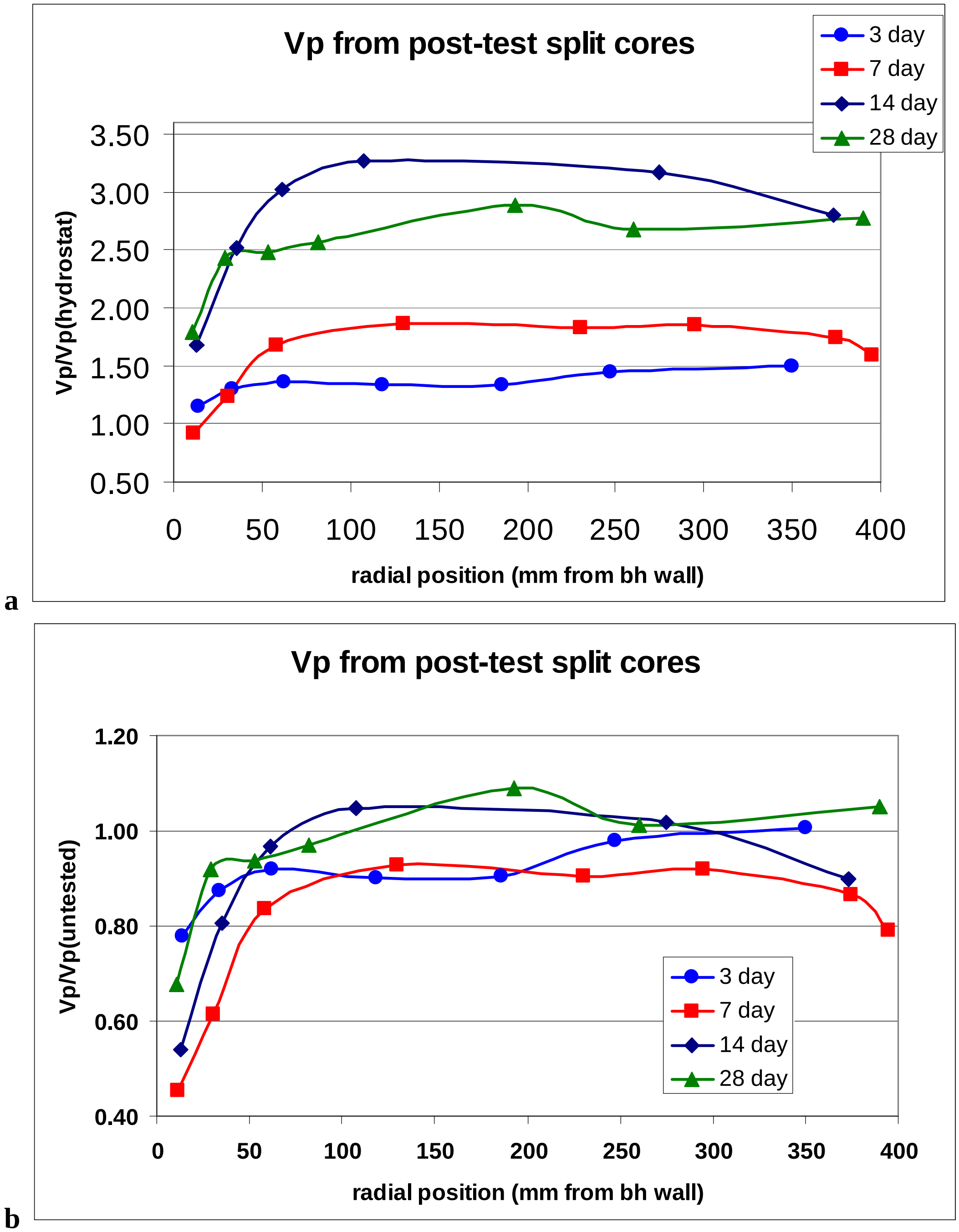

Figure 66. Vp as a function of distance from the borehole wall, measured on specimens cored post-test from cylinders C10, C7, C6 and C4 which were tested at 3, 7, 14, and 28 days after pouring. (a) normalized to Vp measured on specimens loaded hydrostatically and (b) normalized to Vp measured on as-poured specimens.

Elastic propagation is implied by the low strains measured and the amplitudes of the acceleration as the wave propagated outward. The boundary between damaged and undamaged materal was sharp. This observation fits with anecdotal accounts of the damage in the target material around a penetrator. It is typically described as a well defined zone of highly damaged or comminuted rock or concrete. If the damage zone is small then the conclusion is that only a small volume of material immediately adjacent to the penetrator entry axis controls the penetration process. Target diameter, for test shots, should not matter very much until the target diameter approaches a small multiple of the penetrator diameter. A recent paper by Frew et al. (2004) reports measurements designed to determine the effect of target diameter. Their results agree with the conclusion drawn here from the observation of a narrow zone of high damage. An obvious question then is how would fractures effect penetration. One possibility is that, absent a direct strike on a fracture or joint, the effect should be small as long as the fracture or joint spacing is significantly larger than the penetrator diameter. This neglects the effect of a lower compliance associated with the fracture. In future work, we plan to embed model fractures in an experimental arrangement similar to that used in this work to test the effect.

The possible observation of high accelerations near the borehole wall, together with much lower accelerations 150 mm away implies that the majority of the explosive energy was dissipated in the intervening zone, which the velocity measurements show to be even narrower. It is worth recalling that the explosive energy was equivalent to the kinetic energy of a penetrator massing a few kilograms moving at 100 m/s. The energy lost in this zone is what stops a penetrator, so understanding where and how the energy is dissipated will shed light on what makes a material like rock and concrete more or less penetrable. The more energy that is lost per volume of damaged material, the faster the penetrator will stop. The promise of this approach is that energy absorption is easily measured and may be easier to correlate to rock type and properties than other more complex or non-scalar quantities.

Mention has been made of the observation that relatively constant decelerations were observed when high quality measurements were made for penetration into a concrete similar to the one used (Forrestal, et al. (2003)) Because the velocity is changing rapidly as deceleration continues, the material being penetrated is subjected to rapidly-varying strain rates. It is well known that geomaterials exhibit a strain-rate dependence of strength above a critical rate that is often in the 10 to 100/s range. If strain rate was important, then it is hard to see how the deceleration could remain even approximately constant while the properties of the material being penetrated were varying as a function of velocity. A similar hypothesis may be formed from the observation of uniform damage zones along the path of a penetrator. If the damage processes were rate dependent, then the damage zone should be velocity dependent. It seems simplest to assume that rate dependence is not a strong effect, at least in materials where the deceleration is close to a constant. A further implication is that the driving velocity in experiments such as those described in this work is relatively unimportant. Obviously this has a limit; a minimum velocity is required to initiate damage. One of the difficulties of the present experimental approach is that it is difficult to induce velocities that are equivalent to penetrator velocities. Depending on nose shape and position relative to the tip, the velocities imposed by a penetrator vary from 0 to 100+ m/s. 20 m/s was the highest particle velocity observed in the present work, based on the less-than-perfectly-reliable data from accelerometers on the borehole wall.

Conclusions and Recommendations

After a rather steep learning curve, we succeeded in carrying out experiments designed to mimic a portion of the deformation imposed by a penetrator going into concrete. We were able to measure the associated material accelerations, strains and the damage zone created by the cylindrical explosion driving the experiment. Features of the damage and energy absorption appear to reproduce aspects of the penetration process, but in an environment that is more easily controlled and that is more amenable to detailed experimental investigation.

Any future work needs to better account for moisture content. Moisture in pores is an important determinant of the mechanical properties of porous materials such as rock and concrete and it is ubiquitous. All rock or concrete in the earth has some moisture content, often approaching saturation. In the present work, uncertainty was introduced because there seemed to be larger variations in moisture content for samples from the same pour, even though they were stored under apparently similar conditions. This raises the question of the state of saturation of the big cylinders. In future, we would determine the moisture content directly on the test cylinders by removing and testing small cores on test day for the main cylinder.

The discovery that the damage zone was 50 mm thick was not made until the test sequence was completed. It was unfortunate that when we decided to move the accelerometers into the concrete, away from the borehole, we moved 100 mm, which was well outside the damage zone. In future work, measurements would be made within the damage zone if possible, as it is crucial to understand the energy deposition process.

The current work could be extended to cover a higher range of velocities now that the experimental limitations and requirements are well established. As all rock is fractured at some scale, it is important to understand the effect of fractures. Concrete lends itself to casting with fractures included and the techniques used in the present work should shed light on the importance of fractures to penetration.

References

Blum, P., Moisture and density (by mass and volume). “Ocean Drilling Program publication Physical Properties Handbook”, College Station, TX, 1997.

Christensen, N.I., Measurements of dynamic properties of rock at elevated temperatures and pressures. Pincus, H.J., and E.R. Hoskins (Eds.), Measurement of Rock

Properties at Elevated Pressures and Temperatures, ASTM STP 869, American Society for Testing and Materials, Philadelphia, 93-107, 1985.

Forrestal, M.J., D.J. Frew, J.P. Hickerson and T.A. Rohwer, "Penetration of concrete targets with deceleration-time measurements", Int. J. Impact. Eng., 2003, 28, pp. 479-497.

Forrestal, M.J. and D.Y. Tzou, "A spherical cavity-expansion penetration model for concrete targets", Int. J. Solids Structures, 1997, 34, pp. 4127-4146

Fossum, A.F. and R.M. Brannon, "The Sandia GeoModel: Theory and User's Guide," SAND2004-3226, Sandia National Laboratories, Albuquerque, New Mexico, September 2004

Fossum, A.F., "Rock Penetration: Finite Element Sensitivity and Probabilistic Modeling Analyses," SAND2004-3926, Sandia National Laboratories, Albuquerque, New Mexico, September 2004

Frew, D.J. , M.J. Forrestal, and J.D. Cargile, "The effect of concrete target diameter on projectile deceleration and penetration depth", Submitted Int. J. Impact Engineering, 2004.

Gran, J.K. and D.J. Frew, "In-target radial stress measurements from penetration experiments into concrete by ogive-nose steel projectiles", Int. J. Impact Engng., 1997, 19, pp. 715-726

Hill, R., "A Theory of earth movement near a deep underground explosion", Armament Research Establishment Memo No. 21/48, 1948

Kerr, S.A., R.A. Benham, S.M. Harris, S.A. Silling, T.F. Hendrickson, R.G. Lundgren, W. J. Kluesner and M. Groethe, "Calibration and explosively formed projectile test report", Sandia National Laboratories Report SAND98-1811, 1998

Sandia National Laboratories SOP, 15322OP-REMOTE_A&F, *Remote A&F Support on the Installation and Firing of Conventional Explosives (NTS and Other Remote Locations)*

Warren, T.L., A.F. Fossum and D.J. Frew, "Penetration into low strength (23 MPa) concrete: target characterization and simulations", Int. J. Impact. Eng. 2004, 30, pp. 477-503

ACKNOWLEDGEMENTS

The authors wish to thank the 9930 personnel, Anthony T. Evans, and Ed Vieth for their assistance on this test series. Financial support for this work came from Sandia National Laboratories under the Laboratory Directed Research and Development project on the geomechanics of penetration. Support from Campaign 6 was leveraged to provide the concrete test cylinders and staff support.

Distribution

1	MS0751	Larry Costin, 6117
20	MS0751	David Holcomb, 6117
1	MS0751	Arlo Fossum, 6117
1	MS0372	Joe Jung, 9127
1	MS0482	Joel Wirth, 2131
1	MS0482	Tom Togami, 2131
1	MS0482	Ed Hoover, 2131
1	MS0800	J.S. Kendall, 8417
1	MS0800	P.R. Walker, 8417
5	MS0314	L.G. Grant, 9811
	MS0574	D.R. Jones, 5941
8	MS0827	J.R. Dallas, 1502 Attn: R. Collier
1	MS0832	A.T. Walker, 6503
1	MS0841	E.R. Farmer, 3340 Attn: D.G. Anderson, 3341
1	MS0731	Bldg. 823 Library
1	MS0161	Patent and Licensing Office, 11500
3	MS9018	Central Technical Files, 8945-1
2	MS0899	Technical Library, 9616